Sylwester Kaliski Institute of Plasma Physics and Laser Microfusion

Doctoral dissertation

Impurity behavior study in Wendelstein 7-X plasmas by the use of the C/O monitor system

mgr inż. Tomasz Fornal

Supervisor: dr hab. Monika Kubkowska

Supporting supervisor: dr Ireneusz Książek

Warsaw, 2022

Niniejszą pracę dedykuję moim Rodzicom

Streszczenie

C/O monitor jest dedykowanym systemem diagnostycznym przeznaczonym do monitorowania zanieczyszczeń w plazmie stellaratora Wendelstein 7-X (W7-X). Zaprojektowany został do pomiaru natężeń linii Lyman-α wodoropodobnych jonów czterech lekkich zanieczyszczeń – boru (B^{4+} - 4.9 nm), węgla (C^{5+} - 3.4 nm), azotu (N^{6+} - 2.5 nm) oraz tlenu (O^{7+} - 1.9 nm). Jest to optyczny system spektroskopowy oparty o geometrię Johanna z cylindrycznie zakrzywionymi elementami dyspersyjnymi. Jego konstrukcja składa się z dwóch niezależnych komór próżniowych, z których każda przeznaczona jest do pomiaru intensywności dwóch linii spektralnych: pierwsza dedykowana jest pomiarowi linii C oraz O, zaś druga B i N. W trakcie nadchodzącej fazy operacyjnej (OP2.1) pierwsza część spektrometru odpowiedzialna za pomiar linii C oraz O zostanie po raz pierwszy uruchomiona i przetestowana w warunkach eksperymentalnych.

Nadrzędnym celem systemu jest dostarczanie bieżącej informacji na temat intensywności promieniowania wspomnianych jonów, jednak kształt ich linii spektralnych nie będzie przedmiotem rozważań. W związku z tym jest niezwykle istotnym, aby dokładnie zrozumieć zależności pomiędzy zmierzonym sygnałem a parametrami kinetycznymi plazmy tj. temperatury (T_e) i gęstości (n_e) elektronowej, poziomem zanieczyszczeń czy wpływem ich transportu (zachowania się w plazmie) na strumień fotonów docierających do powierzchni detektorów. Zależności te jednak okazują się być nietrywialne ze względu na dużą objętość oraz skomplikowany kształt obserwowanej plazmy, w tym warstwy przybrzegowej, z której znaczna część promieniowania jest emitowana.

Aby odpowiedzieć na te pytania rozwinięto kod numeryczny w języku Python dedykowany do wyznaczania emisyjności oraz całkowitej intensywności promieniowania docierającego do powierzchni detektorów. Niniejsze obliczenia prowadzone są w oparciu o precyzyjne, numeryczne odwzorowanie geometrii systemu diagnostycznego C/O monitor w odniesieniu do układu W7-X i związanych z nim parametrów kinetycznych plazmy.

W celu jakościowego zbadania reakcji systemu na zmieniające się warunki eksperymentalne, jak i również wpływu transportu zanieczyszczeń, przeprowadzono

szereg symulacji przy założeniu różnych profili T_e oraz n_e w plazmie W7-X (z uwzględnieniem modelu równowagi koronowej). Uzyskane wyniki pozwoliły dokładniej zrozumieć wpływ warunków eksperymentalnych na strumienie emisji fotonów w odniesieniu do poziomu zanieczyszczeń. W efekcie zademonstrowano stopień złożoności sygnałów końcowych oraz wykazano wysoką korelację pomiędzy zwiększającą się wartością temperatury (szczególnie w strefie brzegowej) na zmniejszającą się intensywność strumienia emitowanych fotonów. Ponadto, nie bez znaczenia pozostaje kwestia transportu zanieczyszczeń. Przykładowym skutkiem wystąpienia akumulacji zanieczyszczeń w centralnym obszarze plazmy może być spadek (a w przypadku linii tlenu, w pewnym zakresie temperatur, również wzrost) emitowanego strumienia fotonów, mimo, że całkowita zawartość domieszki w plazmie nie uległa zmianie.

W następnej kolejności przeprowadzono studium przypadku dla pomiarów eksperymentalnych zmierzonych podczas ostatniej fazy operacyjnej OP1.2b, gdzie zaobserwowany został przypadek akumulacji domieszek węgla w centralnej części plazmy. Pomiaru radialnych rozkładów zanieczyszczeń linii C^{6+} dokonano za pośrednictwem urządzenia diagnostycznego Charge Exchange Recombination Spectroscopy (CXRS), zaś całkowitą ilość domieszki wraz z radialnym rozkładem wszystkich jej składowych (jonów) wyznaczono przy użyciu kodu pySTRAHLdo modelowania transportu zanieczyszczeń. Następnie, przy użyciu rozwiniętego kodu numerycznego wyznaczono przebieg czasowy potencjalnych sygnałów możliwych do zaobserwowania w sytuacji, gdyby urządzenie diagnostyczne C/O monitor funkcjonowało w trakcie trwania poprzednich sesji eksperymentalnych. Wyniki porównano z przypadkiem równomiernego rozkładu zanieczyszczeń przy założeniu tych samych parametrów kinetycznych plazmy oraz niezmiennej średniej ilości rozpatrywanej domieszki. Wspomniane założenia zastosowano również dla przypadku linii tlenu. Otrzymane wyniki są zgodne z rezultatami uzyskanymi w pierwszej analizie.

Ostatecznie stwierdzono, że system będzie dość wiernie wskazywał zmiany poziomu domieszek w plazmie co potwierdza, że diagnostyka ta będzie kluczowa z punktu widzenia zapewnienia bezpiecznej eksploatacji stellaratora W7-X.

Abstract

The C/O monitor is a dedicated diagnostic system designed to monitor impurity content in the Wendelstein 7-X (W7-X) plasma. It was designed to measure the intensity of Lyman-α lines of hydrogen-like ions of four low-Z impurities - boron (B^{4+} - 4.9 nm), carbon (C^{5+} - 3.4 nm), nitrogen (N^{6+} - 2.5 nm) and oxygen (O^{7+} - 1.9 nm). It is an optical spectroscopic system whose construction is based on Johann geometry with cylindrically curved dispersive elements. It is constructed as two independent vacuum chambers, each designed to measure the intensity of two spectral lines: the first one is dedicated to measuring the C and O lines, and the second one to B and N. During the next operational phase (OP2.1), the first sub-spectrometer dedicated to the measurement of C and O lines will be commissioned.

The main goal of the system is to provide information on the intensities of radiation. However, the shape of their spectral lines will not be investigated. Therefore, it is extremely important to understand thoroughly the origin of the measured output signals with respect to its dependence on the main plasma kinetic parameters, i.e., temperature (T_e) and electron density (n_e), or the impact of impurity transport on the radial impurity distribution, hence radiated photon intensities. These dependencies, however, turn out to be non-trivial due to the large observed plasma volume and its complicated shape, including the edge plasma layers, from which most of the radiation is emitted.

To answer these questions, a numerical code in Python dedicated to determine the emissivity and the total intensity of radiation reaching the detectors' surfaces was developed. Its purpose is to precisely reproduce the system's geometry with respect to the W7-X and to determine the output signals originating from the investigated lines. Consequently, mainly qualitative information on the emitted photon flux intensities is obtained, but in the future, after an absolute calibration of the system, it will also be possible to obtain quantitative results.

To examine the response of the system to the experimental conditions qualitatively, a series of simulations was performed, assuming various T_e and n_e profiles in the W7-X plasma (with the use of corona equilibrium model). The aim of this analysis was to estimate the expected radiation fluxes and to determine the sensitivity of the system

to the changes in impurity levels, as well as plasma kinetic parameters. The results of analysis demonstrated complexity of the output signals including a high correlation between e.g., increasing temperature (especially in the edge region) and decreasing intensity of the emitted photon fluxes. The problem of impurity transport is also important. For example, their accumulation in the central plasma region can lead to a decrease (and in the case of oxygen lines, over a certain temperature range, also increase) in the emitted photon flux, even though the total impurity content in the plasma remained unchanged.

A case study was then performed for the experimental results registered during the previous operational phase OP1.2b, where carbon accumulation was observed in the central plasma region. The radial distribution of impurities from the C^{6+} line was measured using the Charge Exchange Recombination Spectroscopy (CXRS). Based on these measurements, the distribution of all C ions along minor plasma radius was calculated using the pySTRAHL code. Then, using the developed code, the time evolution of the potential signals was determined. These calculations illustrated photon flux which would be observed if the C/O monitor system was in operation during the previous experimental phase. The results were subsequently compared with the 'flat' impurity profile, assuming exact kinetic parameters and a constant average impurity content in the plasma. A similar procedure was also used for the oxygen line. The obtained results match previous findings.

Finally, it was concluded that the system will fairly accurately reflect the changes of impurity level in the plasma, which confirms that the diagnostic will be crucial from the safety point of W7-X operation.

Contents

10

Motivation and scope of the work

An ideal fusion plasma contains only the intended reactants – hydrogen isotopes and the fusion reaction product – helium. However, in real fusion devices with magnetic confinement (MCF – magnetic confinement fusion), plasma is always contaminated by other elements, so-called impurities, which are essential from the operational point of view of a future fusion reactors. Their origin is usually associated with the interior of the plasma vessel, mainly the first wall materials and elements adsorbed at its surface. In some experiments, impurities are also introduced intentionally, e.g., in order to mitigate plasma instabilities, change erosion of the wall or to study the influence of impurities and their transport. The most undesirable impurity species are mid- and high-Z elements, which lead to essential energy losses of a plasma by emission of radiation in the form of spectral lines. This can be particularly dangerous when the impurity accumulation occurs in the central plasma region, leading to a 'fuel' dilution and eventually to a radiational plasma collapse. To reduce these effects, internal components of a plasma vessel are made of carbon or can be covered with thin layers of low-Z elements such as e.g., boron or beryllium. In modern fusion experiments, the first wall or some components are usually metallic (e.g., tungsten) reducing carbon level significantly, but its spectral lines can still be observed. Another light element constantly present in MCF plasmas is oxygen, which is absorbed on the surfaces of the inner walls of the vessel as water molecules during the machine's venting. It is afterwards consistently released during the operation of the device. Nitrogen, together with oxygen, may be an indicator of a leakage in the vacuum system. Nevertheless, it can be also introduced intentionally during some experiments.

The Wendelstein 7-X (W7-X) [1] is the largest and the most advanced stellarator which was constructed to demonstrate high power and high performance quasi-continuous operation. There are several diagnostic systems dedicated to observation of Wendelstein 7-X plasmas' contamination, e.g., HEXOS (high efficiency extreme ultraviolet overview spectrometer) [2], PHA (pulse height analysis) [3], [4], XICS (the x-ray imaging crystal spectrometer) [5], [6] or HR-XIS (the high-resolution x-ray imaging spectrometer) [6]. One of them, the C/O monitor, is a new dedicated XUV spectrometer designed for monitoring of four, main low-Z impurities: B, C, N and O.

These measurements will be performed by observation Lyman-α transitions of their hydrogen-like ions. It is a crystal spectrometer whose construction is based on Johann geometry with cylindricaly curved dispersive elements. The ultimate puporse of the system is to provide continuous information about the line intensities of the respective hydrogen-like ions without study of the line shapes. It is a high time resolution (1 ms) and a high throughput system with large acceptance angle. Its commissioning is planned for the next Operational Phase 2.1 (OP2.1)

Since the system will measure volume integrated radiated photon intensity originating from a large plasma volume, the analysis and proper interpretation of obtained experimental data may become very difficult, especially under rapidly changing plasma conditions. Beside the potential change of impurity density in the plasma, there are other factors such as changes of the kinetic parameters and radial impurity distribution that may affect the measured signals significantly. For example, the impurity accumulation in the W7-X plasmas can occur resulting in a shift of their significant fraction towards the plasma center. Since stellarators are characterized with their complex, helical-like plasma shapes, the impurity profiles may also affect obtained signals significantly. Especially difficult case for analysis may arise when several factors occur simultaneously, e.g., change in the total impurity content, its radial profile shape as well as fluctuations of electron temperature (T_e) and electron/plasma density (n_e).

Therefore, it is essential to check how each of these factors affect the output signal i.e. intensity of a specific spectral line. It was presumed that some of those factors may compensate each other (e.g., decrease of electron temperature and a reduced impurity content), thus making it difficult to draw decisive conclusions. For that reason, it was essential to implement techniques to simulate possible reactions of the system under various plasma conditions.

The work presented in this thesis aims to develop the C/O monitor spectroscopic system and apply a modelling approach to predict future signals based on the aforementioned factors. Hence, the main tasks related to this topic were to:

1. Desig the key components of the C/O monitor system for W7-X;

2. Develop a comprehensive code for the detailed representation of the system's geometry enabling simulations of a potential signals with respect to a geometry of observed plasma volume, kinetic plasma parameters (T_e, n_e), as well as spatial impurity distribution. The code assumes a corona model and was integrated with external package pySTRAHL [7] used for modelling of impurity transport in a plasma.

3. Perform qualitative investigation of the influence of the electron temperature, electron density and impurity profile shapes (assuming their constant level in the plasma) on the radiated photon intensities at the detectors' positions.

4. Perform case study for the sample of plasma discharge, where accumulation of C in the plasma center was observed. The obtained outcomes were to be compared with uniform ('flat') impurity profile case. The same approach was applied for the O line investigation.

Some research results that are closely related to the topic of this dissertation have already been described in the following scientific papers:

1. **T. Fornal,** M. Kubkowska, I. Książek, D. Stańczak, S. Jabłoński, R. Burhenn, **"Modelling of expected B, C, N and O Lyman-α line intensities emitted from W7-X plasmas and measured by means of the W7-X light impurity monitor system",** The European Physical Journal Plus (2021), volume 136, Article number: 659 ;

2. **T. Fornal,** I. Książek, M. Kubkowska, R. Burhenn, **"Estimation of Photon Flux of the Oxygen Lyman-α Line Emitted from the W7-X Plasmas",** Acta Physica Polonica A (2020), No. 4 Vol. 138;

3. **T. Fornal,** I. Książek, M. Kubkowska, J. Kaczmarczyk, R. Burhenn, **"Choice of the detectors for light impurities plasma studies at W7-X using "CO Monitor" system",** Fusion Engineering and Design (2019) 146, 1-4;

4. **T. Fornal,** I. Książek, J. Kaczmarczyk, W. Figacz, M. Kubkowska, R. Burhenn, F. Kunkel, R. Laube, S. Renard, **"XUV diagnostic to monitor H-like emission from B, C, N, and O for the W7-X stellarator",** Review of Scientific Instruments (2019) 90, 1-8.

1   Introduction

Ensuring access to the reliable energy source for the society living in the 21st century is currently one of the largest issues to tackle and it will become even more serious in the next decades. A stable source of energy is essential for a proper functioning of all branches of everyday life such as health care, water supply, sewage system, transportation and the global telecommunication network being the foundation of the current, technical civilization. Basically, each aspect of our daily existence is strongly dependent on energy supply. The energy demand per person is constantly increasing and the trend continues in developed countries of Europe, North America and Asia what is correlated with the living standard. Other developing countries (e.g., India or China with population above 1 billion) are in pursuit of better living standards, hence their energy consumption is constantly increasing while worsening the global climate related situation. The climate crisis we are facing requires continuous carbon footprint reduction thus providing clean, reliable energy system is nowadays a crucial factor.

The current world's energy system is based mostly on fossil fuels like coal, natural gas, and oil. Their combustion lead to abrupt release of significant amounts of carbon dioxide as well as other pollutants into the atmosphere, increasing the greenhouse effect. There also exist renewable energy sources such as e.g., solar panels, wind turbines and hydropower, but they still play a minor role in the global energy market. They are considered a 'clean' energy source with almost zero emission of 'greenhouse' gases using 'free' resources at the same time. Their common adoption, however, is far more difficult than those based on fossil fuels due to certain conditions that must be met (e.g., sunny or windy terrains). This leads to a situation where the renewable energy cannot sustain the energy needs of today's society with its current shape (due to the lack of the stability in energy supply as well as the energy 'quality').

An alternative solution providing stable and free of 'greenhouse' gases emission energy source might be nuclear fission which in the current days plays recognizable role for the electricity production. The nuclear energy is clean and reliable, therefore the energy system of many developed countries is based on the energy from nuclear fission. Moreover, spent fuel is no longer a serious issue since good solutions related to

its storage exist on a market for many years [8]. After five – six years of operation in nuclear reactor (which is the typical length of the reactor fuel cycle), more than 90% of its potential energy remains in the fuel [9], which can be reused in the IVth generation of reactors, e.g., very high temperature nuclear reactors (VHTR) [10]. However, on a global scale this would not be practicable due to low acceptance level from the society, driven by the fear resulted from several major failures of nuclear fission power plants that occurred in the past.

An alternative might be energy from nuclear fusion - the process similar to this powering the Sun based on energy released when two nuclei of e.g., deuterium and tritium combine. Since 'fuels' required to perform the desired reactions are easily accessible in the world (deuterium can be derived from water while tritium can be produced by reactions of neutron with lithium from common Earth rocks), there would be virtually no limitations to the energy production and fuel supply.

Nuclear fusion emits no greenhouse gasses and provides access to the unlimited source of clean energy. Moreover, in contrast to nuclear fission, there is no chain reaction, hence its safety is indisputably higher. The fusion technology is not yet fully developed as above-described fission technology, but is under intense research phase, and might become a solid candidate for the energy resource of the future. This may happen around 2050 when the first commercial fusion power plant is planned to be brought into operation.

To achieve this goal, the research on high temperature plasma (occurring in the thermonuclear reactors as tokamaks or stellarators), which could bring the thermonuclear reactors to the operation, is highly prioritized. It is also essential to emphasize the fact that the measurement of the plasma parameters (electron temperature, density, magnetohydrodynamics (MHD), confinement etc.) are the key elements for the long pulse operation. Since the plasma is not free from impurities, their measurement is also of crucial importance because they strongly affect the plasma stability and play key role in the energy balance.

For those reasons, the constant work related to the plasma research is one of the priorities of the modern science. It is especially important for the development of technology ensuring the application of the fusion to deliver clean energy, which

nowadays becomes one of the largest priorities. This will help to reduce the greenhouse emission while providing the inexhaustible energy for mankind of XXIst century and the next millennia.

1.1   General plasma description

Plasma after solids, liquid and gas – is considered as a fourth state of matter. It resembles gas but due to the fact that its properties differ significantly, it deserved to be named as fourth state of matter [11]. The plasma is an ionized gas containing electrons and ions coexisting together, created by providing energy freeing the electrons from atoms, in which a significant part of particles is electrically charged.

Plasma is typically an electrically quasi-neutral, which means that on the large scale the number of positive and negative charges is the same. By saying 'large scale' it means distances larger then Debye length r_D, which determines the rate of particle's electric field intensity decrease depending on the distance from it. This is described by equation (1) [12]:

$$r_D = \sqrt{\frac{\varepsilon_0 k_B T}{e^2 (n_e + \sum_{z,a} z^2 n_a^z)}} \qquad (1)$$

where n_e - electron density, n_a^z – density of a particles with the ionization state z, T – plasma temperature, e - electron mass and ε_0 an k_B are the well-known constants. Charged particles generate electric currents, therefore any movement of the plasma is affected by the field generated by the other charged particles. This influences their collective behavior.

Plasma is mostly associated with stars and can be also found in the interstellar space between galaxies. It is very dense and hot in the core of the stars, while in the stellar atmospheres as well as interstellar space it is rare and characterizes with lower temperatures. Considering the stars, the further from the core, the lower density and temperature of the plasma, what is associated with its different properties. The solar corona is a dilute magnetized plasma with the temperature of several million degrees. Plasma is then emitted into outer space and planetary system in a form of solar wind. When solar wind reaches the Earth, its interaction with the upper part of the

atmosphere partially ionizes its upper layers, which is called ionosphere. Plasma is also very common in our everyday life. We can observe it during gas discharges (e.g., lightnings) as well as its use in the modern technologies (e.g., plasma welding, plasma tv, fluorescent lamps, etc.).

The term 'plasma' in general describes the state of matter with very different properties. Depending on its type, the differences between their densities and temperatures may be in the range of several orders of magnitude. Figure 1.1. [13] presents the variety of plasma types depending on their temperature and electron density.
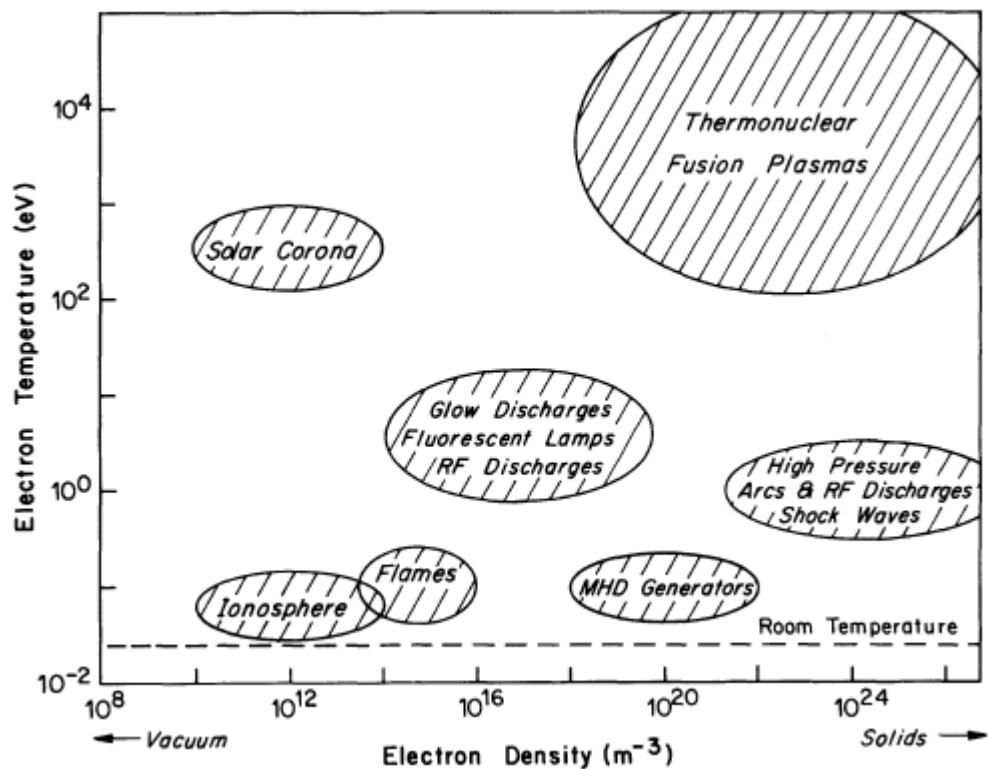
Figure 1.1. Variety of plasmas characterized by electron density and temperatures.

There is a popular division into low and high-temperature plasmas. The low temperature plasma is the plasma with nuclei temperature (both - heavy ions and electrons) from the room temperature up to several thousand Kelvins [11]. This range corresponds to the average kinetic energy of the particles from fractions of an electronvolt (eV) to a few electronvolts. Such plasma can be e.g., aurora, ionosphere, fluorescent lamps, or flame. The high temperature plasma, however, is usually

reserved for thermonuclear plasma, with temperatures order of millions of K (with corresponding energy of several keV). An example can be e.g., core of the Sun or magnetic fusion.

1.1.1 Nuclear Fusion – physical reactions

Fusion is the process that powers the stars so also the Sun. It takes place when two light atoms combine (or 'fuse') together into heavier one. As a result, the products in the form of neutrons, protons, photons and alpha particles are created while emitting a large amount of energy.

Synthesis reactions are characteristic mainly for light nuclei (such as e.g., hydrogen and helium), but they also occur for heavier particles. However, in the case of light nuclei, these reactions are exothermic and above a certain limit of atomic mass (iron), they become endothermic requiring an input of energy to proceed and are signified by a positive change in enthalpy. This dependence is explained in Figure 1.2 presenting the binding energy per nucleon (MeV), which is energy required to decompose the nucleus of a given atom per nuclides (protons and neutrons).
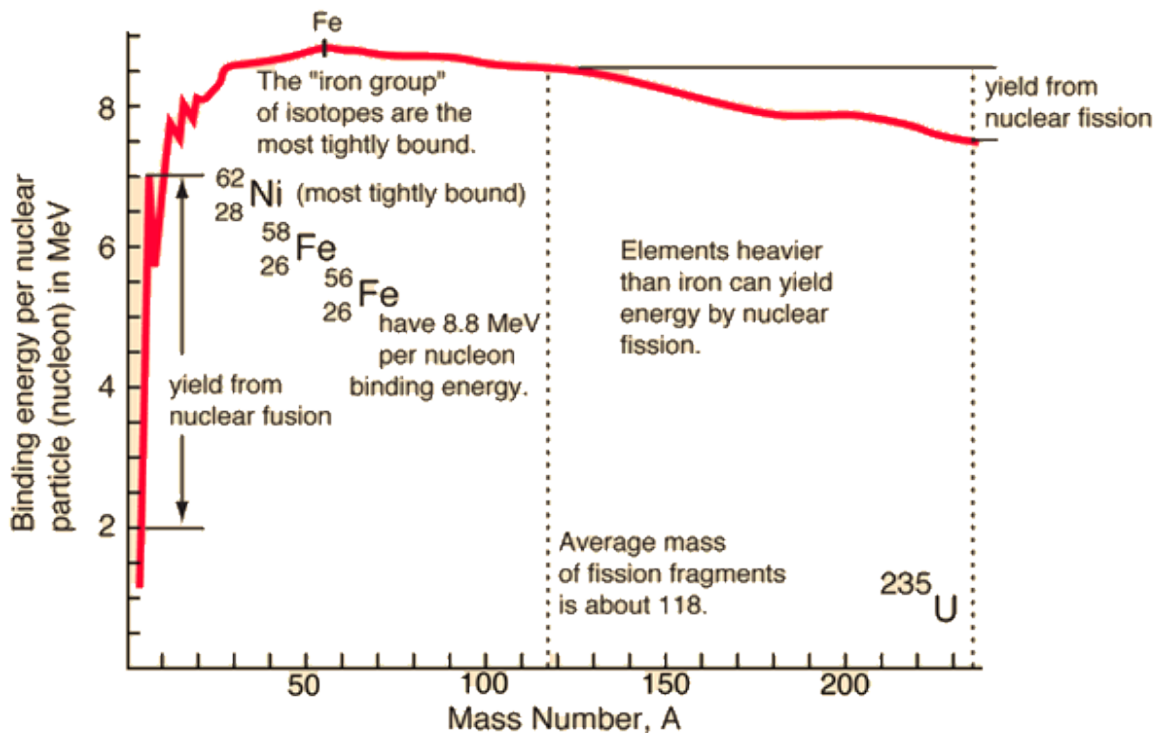
Figure 1.2. Binding energy per nucleon versus atomic mass number [14]*.*

On the other hand, the binding energy is equal to the amount of energy released in the process of thermonuclear fusion. Thus, the difference in masses of substrates and products multiplied by the square of the speed of light result in an energy release E_B [15]:

$$E_B = \left(Nm_n + Zm_p - m_A\right)c^2 \qquad (2)$$

where N − number of neutrons, Z − atomic number, m_p − rest mass of proton, m_n − rest mass of neutron, m_A - nuclear mass and c − speed of light.

According to the Figure 1.2, hydrogen nucleus has the lowest binding energy level. By the process of synthesis of two hydrogen isotopes nuclei (as e.g., D + D or D + T), a helium nucleus will be formed, and the difference in their masses will be the amount of emitted energy. On the other hand, iron has the highest binding energy, and is also the most stable element. For nuclei with higher atomic masses, from the energetic point of view, the nuclear fission reaction will be much more profitable (breaking into lighter nuclei with simultaneous emission of excess energy).

The above-described reactions are the basis for the existence of all stars which, by synthesizing hydrogen atoms into heavier nuclei, emit significant amount of energy. Each star, depending on its mass and temperature, 'burns' its fuel in a slow process that takes billions of years (in the case of the Sun it is several billion years). The formation of helium from hydrogen nuclei can be accomplished by various nuclear reactions. Depending on the mass of the star, these reactions can occur through two main cycles. The cycle, which powers smaller stars (such as the Sun) with their temperatures reaching up to several million Kelvins is the proton-proton chain (p-p chain) resulting in release a net energy of E = 26.7 MeV [16]. For more massive stars, the fusion reactions take place via the carbon-nitrogen-oxygen (CNO) cycle.

1.1.2 Fusion on earth

To perform the nuclear fusion of two nuclei, it is necessary to provide an amount of energy sufficient to overcome the Coulomb barrier. This means that thermonuclear synthesis requires an ignition temperature usually exceeding 10 keV, in which the matter is in the form of plasma. In terrestrial conditions such temperatures do not

exist naturally and are very difficult to obtain. There are several reaction channels that may be crucial for the future fusion reactors. They are presented below together with energies releases in those reactions [17]:

$$D^2 + D^2 \rightarrow T^3 + H^1 + (4.03 \; MeV) \tag{3}$$

$$D^2 + D^2 \rightarrow He^3 + n^1 + (3.27 \; MeV) \tag{4}$$

$$D^2 + T^3 \rightarrow He^4 + n^1 + (17.60 \; MeV) \tag{5}$$

$$D^2 + He^3 \rightarrow He^4 + H^1 + (18.30 \; MeV) \tag{6}$$
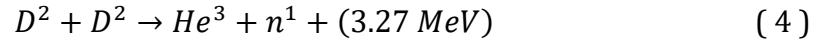
The energy efficiency of the above-mentioned reactions can also be assessed on the basis of the probability of their occurance (i.e. reaction cross-section) – see Figure 1.3.
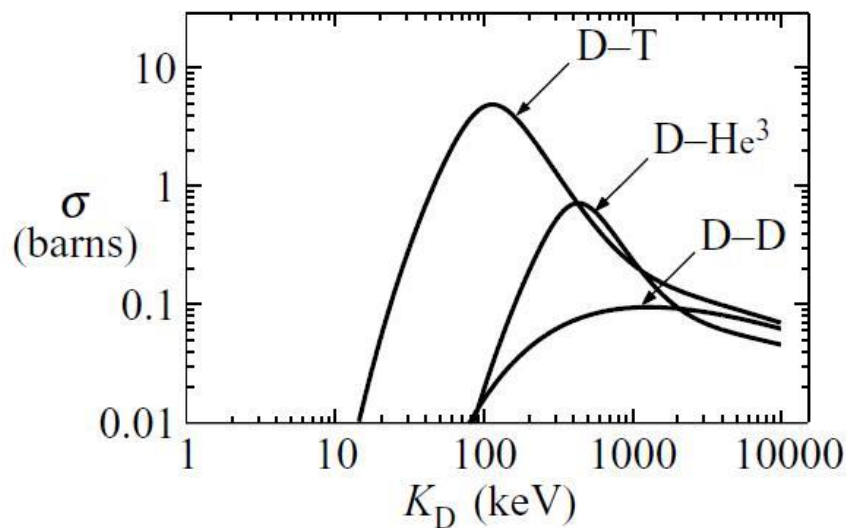
Figure 1.3. Fusion reaction rate coefficients for the D-T, D-D and D-He³ as a function of electron temperature [15].

Due to the aforementioned nuclei binding energies and the cross-sections of those reactions, the most promising channel is the D-T reaction (4), which not only has the highest cross-section of the reaction but also requires relatively low initial energy while releasing 17.6 MeV. Taking this into account together with almost ten times lower requirements for the initial temperature level than those for the D-D reaction, it is the main candidate for fusions in terrestrial conditions. Nevertheless, given the high

temperatures required for fusion reactions, the energy of tenth kilo electron volts needs to be provided.

In order to ensure the self-sustained synthesis reaction, three conditions must be met at the same time: temperature, sufficiently high plasma density and confinement time. The above means, that the deuterium/tritium plasma must be sustained long enough for the synthesis reaction to take place. This is so-called Lawson criterion (defined as a triple product), fulfilment of which will release the reaction energy high enough to exceed the energy losses, thanks to which the positive energy balance can be achieved. In the case of deuterium and tritium synthesis, the Lawson criterion [18] takes the form described by the inequality (7):

$$n \cdot T \cdot t_E > 5 \cdot 10^{21} \ [keV \cdot s \cdot m^{-3}] \qquad\qquad (7)$$

where n = plasma density, T – temperature and t_E – confinement time.

In order to ensure the highest reaction efficiency, it is ultimately necessary to provide the proper fuel density. Due to the 'burning' of the fuel as well as contamination by other atoms and the accumulation of helium ions the power obtained during synthesis is reduced. Therefore fuel (deuterium and tritium) must be refilled and helium (fusion 'ash') needs to be removed. The confinement time increases significantly as the plasma volume increases. Therefore, it is strongly desirable to create ever larger fusion facilities to provide favourable conditions for the implementation of thermonuclear synthesis.

1.1.3 Fusion confinement

Due to extreme temperatures required to initiate the thermonuclear reaction, carrying out a synthesis under terrestrial condition is quite a challenge. Direct contact of a plasma with inner vessel's components could lead to its immediate cooling and also degradation of the plasma facing components. Therefore, it is necessary to use appropriate method of isolating the plasma as well as ensuring a technique of its maintenance that guarantees the safety of adjacent materials and, consequently, creates appropriate conditions for the reaction.

There are three known ways of plasma confinement: gravitational, inertial and magnetic. In stars, the confinement is achieved by their strong gravitational field that creates sufficient pressure. Those conditions are, however, not applicable on Earth. Another approach is the inertial confinement, the idea of which is the significant compression of the pellet with thermonuclear fuel by strong, well-focused, symmetrical laser pulses or ion-beams. There are two major methods developed to perform inertial fusion reactions. The simplest one, also called direct drive method, is the concept where the fuel is arranged as a sphere and a laser pulses are being focused directly on a capsule (see Figure 1.4). The surface of the pellet evaporates to a form of plasma-crown, and the expanding plasma creates a shock wave towards the pellet, leading to its implosion. As a result, a short-term fusion reaction takes place.
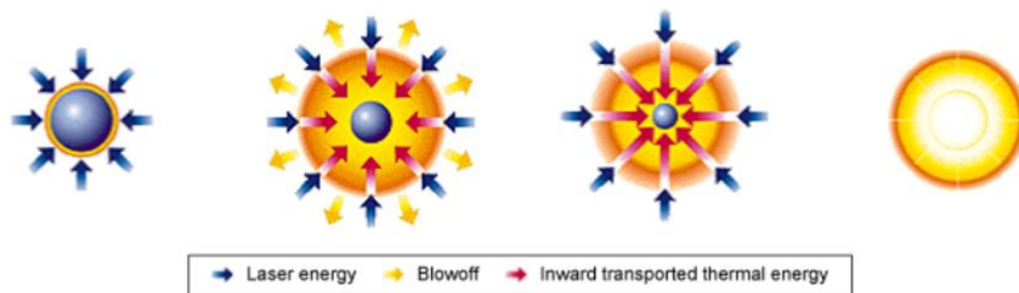
Figure 1.4. The direct-drive laser-based approach of Inertial confinement fusion [19]*.*

Another approach is the indirect drive method where the laser or ion-beams are not aimed directly at the capsule containing fuel, but into a special target containing fuel, usually small cylinder made of gold which is also called as 'hohlraum' (see Figure 1.5). The idea is not to use beams to target fuel capsules but the interior of a cylinder leading to its heating until it starts emitting X-ray radiation. These X-rays heat the fuel capsule and begin the fusion reaction [20].

22
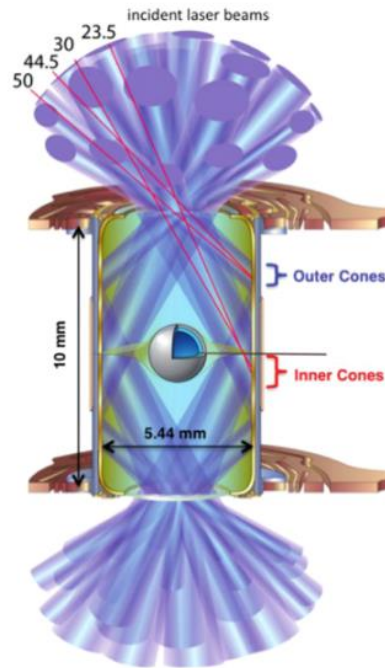
Figure 1.5. The hohlraum target used in the indirect-drive method of inertial confinement fusion [21]*.*

The most promising way of a plasma confinement in terms of its application as energy source of the future is magnetic confinement. Taking into account the fact that the plasma as a collection of charged particles can be controlled by magnetic and electric fields, it is possible to use magnetic traps to keep the specific plasma volume away from the wall of the vessel. Charged particles placed in the magnetic field begin to move helically along the magnetic field lines.

Some initial research on fusion was carried out using the linear configuration of the magnetic field, characteristic for mirror reactors (also known as magnetic bottle). In a cylindrical plasma chamber, a magnetic field parallel to its axis keeps particles along the field lines (presented in Figure 1.6). Configuration of electromagnets in magnetic mirror creates the area of increased density of magnetic field lines at either end of the confinement area. Particles approaching the ends experience an increasing opposing force, causing them to reverse direction and reflect the certain number of particles back into the cylinder interior. This effect, however, occurs only for the particles with limited approaching velocities and angles.
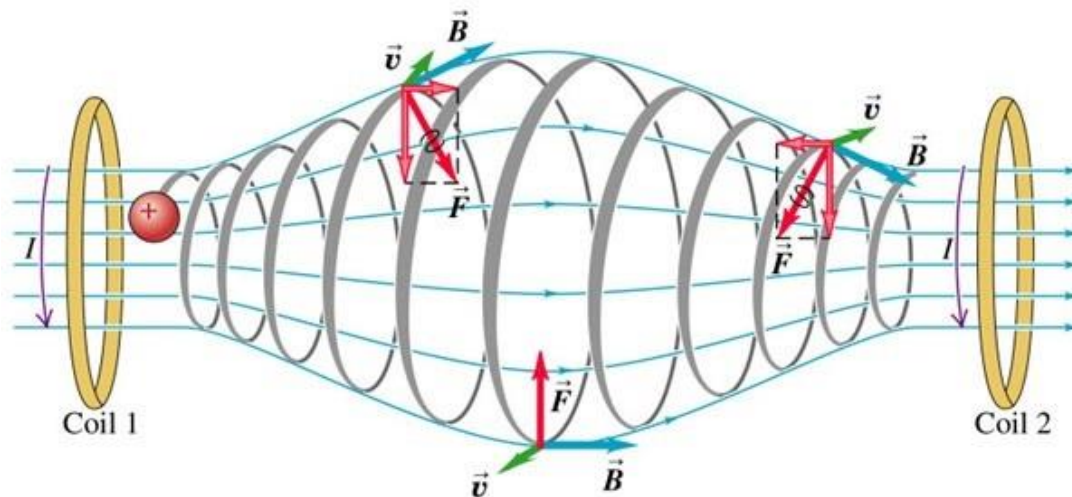
Figure 1.6. Concept of the magnetic mirror including motion of charged particle [22]*.*

Since the particle losses in magnetic mirror trap may be substantial, they can be eliminated by curving the cylinder into the form of closed ring (torus) – see Figure 1.7. Then we deal with the toroidal magnetic field. However, the early experiments showed that plasma lost its initial symmetric form and developed "kinks". This result implied that the plasma was unstable. As a consequence, in almost all subsequent experiments these instabilities limited achievable plasma conditions [23]. Another disadvantage of this solution is the heterogeneity of the magnetic field, which pushes the plasma outwards, bringing it into contact with the wall of the vessel.
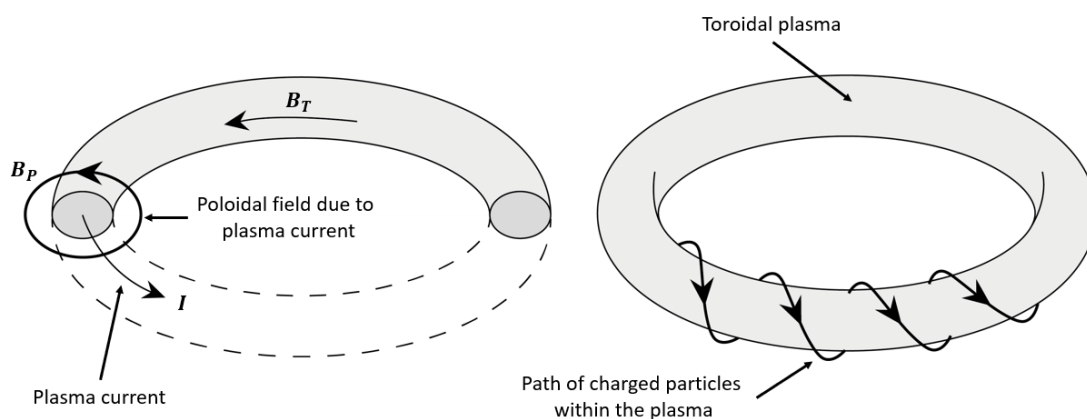
Figure 1.7. The magnetic field distribution of the torus. Left figure presents the direction of a plasma current, poloidal and toroidal fields. Right side presents the path of charged particles within the toroidal plasma [24]*.*

To reduce the impact of this effect, poloidal (perpendicular to the toroidal) magnetic fields are applied. The resulting magnetic field not only have to enclose the lines into rings, but also follow helical paths while creating closed magnetic flux surface. These assumptions were implemented by two conceptual methods – tokamaks and stellarators. Both concepts, together with their main features, similarities and differences are presented in the next section.

1.2 Nuclear fusion in magnetic confinement plasma devices (MCF)

1.2.1 Tokamaks and stellarators – similarities and differences

The concept of magnetically confined fusion is nowadays realized by the two most promising technologies: tokamaks and stellarators (Figure 1.8). Their constructions provide helical (poloidal and toroidal) magnetic fields, producing toroidally nested and closed magnetic surfaces. As a result, the similar stability and plasma confinement is achieved for both configurations. However, constructions of these technologies differ significantly, which results in their different properties. Therefore, their characteristics will be elaborated in more detail.

Figure 1.8. Schematic representation of a tokamak (left) and stellarator (right) [25]*.*

First of them, tokamak (from Russian '*Toroidalnaja Kamiera s Magnitnymi Katuszkami'* – toroidal chamber with magnetic coils), is constructed as a vacuum chamber in the shape of a torus containing the plasma. The toroidal magnetic field is created by the applied set of outer coils surrounding its vacuum chamber. This acts as a primary mechanism of plasma confinement. The poloidal magnetic field, however, is generated by an electric current induced in the plasma by the use of a transformer. Its primary circuit is a set of poloidal coils in its core, and the secondary circuit is the plasma.

Consequently - the combination of both toroidal and poloidal magnetic fields, results in field lines taking a helical path around the torus [23].

The second concept is a stellarator, which forms the plasma shape as a twisted Mobius strip. This is achieved by the application of a specially designed magnetic coils mounted outside the toroidal vacuum chamber. Moreover, stellarators to achieve plasma stability do not require current induced in the plasma. There are, however, plenty of other differences occurring during their operation, which together with aforementioned features results in a different pros and cons of both technologies.

The main difference between tokamaks and stellarators is the plasma confinement mechanism. In tokamaks the toroidal set of coils produces the stabilizing toroidal field component and large toroidal current which is induced in the plasma producing most of the confining poloidal field. Nevertheless, since the axisymmetric shape of the tokamak plasma results in its appropriate confinement, such induced current leads to plasma instabilities, obstructing its continuous operation. In stellarators, however, current flowing in external non-axisymmetric coils solely creates both of the magnetic field components, therefore the continuous work may be achieved. Nevertheless, due to the higher complexity of the stellarator's geometry, there are more unconfined particle orbits, leading to a high transport of ionized particles.

Both machines can be described using two coordinate systems – cylindrical and magnetic flux. The cylindrical coordinate system is defined by radial (R), vertical (Z) and toroidal (φ) components. The major radius (R) is a distance measured from the center of a torus and vertical coordinate (Z) is perpendicular to R - see Figure 1.9. Unlike cylindrical, the magnetic flux coordinate system depends on the flux surfaces and is described by radial (r_{eff}), toroidal (φ) and poloidal (θ) components. The r_{eff} (also called effective minor radius) is calculated from the minor radius (r) which is a distance from axis of a plasma (poloidal cross section of a torus) to the last closed flux surface (LCFS) [26]. Its principle is based on assumption that any given point is the average radius of a specific flux surface passing through that point, which results in r_{eff} value representing this flux surface. Such transformation is useful for simplification since the shape of magnetic field lines is non-symmetrical and for stellarators changes with a

toroidal angle (non-axisymmetric) thereby hindering comparison of measurements from different diagnostics and experimental machines.

Since tokamaks and stellarators can be described using above-described coordinate systems they differ in the ratio of their major (R) and minor (r_{eff}) radii. In tokamaks this aspect ratio is usually between 2.5 (in JET) and 4 (in ASDEX) resulting in the larger effective plasma volume [27]. In stellarators this ratio varies in the range between 5 (in CHS) and 12 (in W7-AS) [27]. Therefore, the device is constructed to have small rotational transformation per geometrical period.
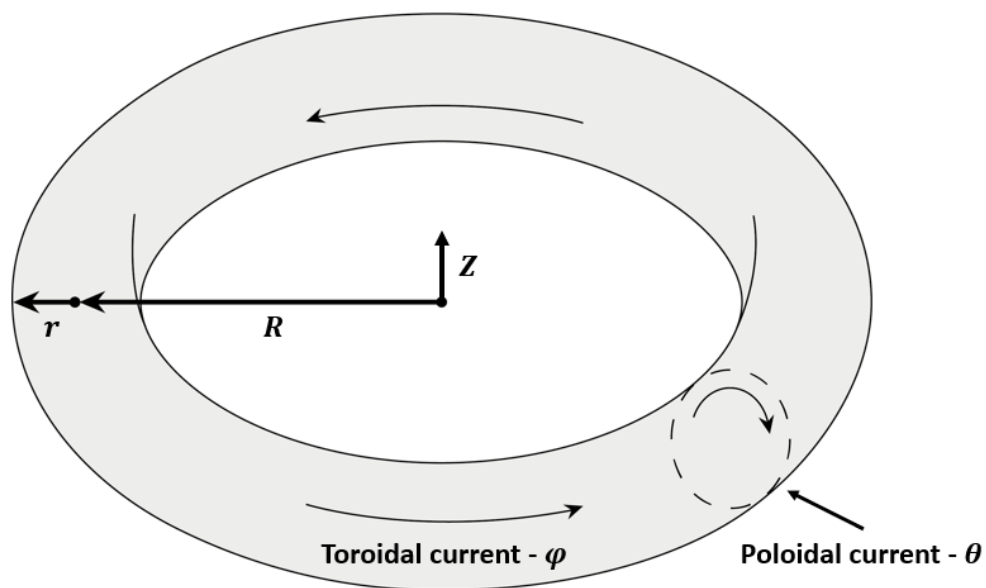
Figure 1.9. The relation between major (R) and minor radius (r) of a spherical fusion reactor [23]*.*

Another important aspect is the magnetohydrodynamic (MHD) instabilities. In fusion plasmas, they play crucial role in determination of achieving stable plasma parameters, advanced scenarios, and operational limits. The source of the MHD instabilities arises from pressure and current gradients as well as unfavorable curvatures of magnetic field lines. In the case of tokamaks, the current induced in the plasma becomes a main source of MHD instabilities. Moreover, they also cause serious issues related to high mechanical and heat loads of machine's components. Therefore, since disruptions (which are basically the most dangerous instabilities occurring during plasma operation) became a serious issue for tokamak's operation, this topic is under continuous intense study [23]. In contrast to tokamaks, almost no MHD instabilities are observed during operation of stellarators due to absence of the net current in the plasma. In the

stellarator plasmas, however, the two small plasma currents exist: Pfirsch-Schluter current and bootstrap current [28], nonetheless those are substantially smaller and cannot create MHD modes. Marginal role of MHD instabilities in stellarators is a great advantage, in consequence reducing the limitations of the reactor.

In the fusion experiments, the increase of plasma densities leads predominantly to a significant increase of impurity content what consequently results in enhanced radiated power losses. The highest emission originates from higher-Z elements what finally can cause the plasma collapse. In tokamaks the rapid cooling of the outer plasma boundary with accompanied MHD instabilities leads to the plasma disruptions. This might occur when the Greenwald limit (n_G) [15] is exceeded. This limit is especially important for the magnetically confined fusion reactors with net plasma current induced, such as tokamaks, since many studies present, that rapid delivery of fuel to the plasma can lead to disruptions. In stellarators the Greenwald limit does not exist because no toroidal current is induced. As a result, stellarators usually operate at higher density regimes than tokamaks. However, the density limit is dictated by the absorbed power and enhanced impurity radiation leading to the temperature collapse. Another type of edge phenomenon occurring in tokamaks is multifaceted asymmetric radiation from edge (MARFE), which is characterized by a high radiation intensity from the zone of the inner side of the torus, resulting in the plasma cooling. Unlike in tokamaks, the transport in stellarators is significantly stronger, hence causing the drift of impurities towards the plasma and, in consequence, its cooling down.

Both devices have their pros and cons. In principle, they are based on helical magnetic fields, which can result in a similar plasma confinement. Unlike tokamaks, the stellarator plasma is non-axisymmetric, hence the shapes of poloidal cross sections change when rotating around the torus and magnetic axis. For that reason, the construction of tokamak is characterized by its simplicity (and lower costs) and is less affected by a neoclassical transport. On the other hand, stellarators are almost free from MHD instabilities resulting in a longer, more stable plasma discharge. The absence of a net plasma current leads to a steady-state operation and its high efficiency, but its more complicated shape increase the construction costs of the

machine. Nevertheless, the stellarator may turn out to be a much better choice for the future application as fusion power plants.

1.2.2 Wendelstein 7-X project

The W7-X stellarator is located in the Max Planck Institute for Plasma Physics in Greifswald (Germany). It is currently the largest and the most advanced fusion device of a helical type in the world. The second one is the Large Helical Device (LHD) in National Institute for Fusion Science in Japan. The purpose of W7-X is to demonstrate the high performance and continuous, long pulse operation, ensuring that the plasma will be sustained for about 30 minutes. Moreover, it is essential to manifest the benefits of optimized magnetic field geometry resulting in neoclassical transport reduction, good magneto-hydrodynamic stability, and fast particle confinement.

The W7-X is constructed as a five-fold Möbius strip. The whole stellarator is composed of five identical sections, each divided into two symmetrical segments (see Figure 1.10 – a)). Its major radius is R ≈ 5.5 m, minor radius is r ≈ 0.5 m, and the total plasma volume equals approx. 30 m^3. The magnetic field is generated by the set of 70 superconducting magnetic coils with about 3.5 m height. Each segment contains 2 planar and 5 non-planar coils (see Figure 1.10 – b)). All superconducting coils are cooled down to the temperature approx. 3.4 K. This setup is able to generate the magnetic field reaching its maximum level B_0 ≈ 2.5 T at the plasma magnetic axis.

a)   b)
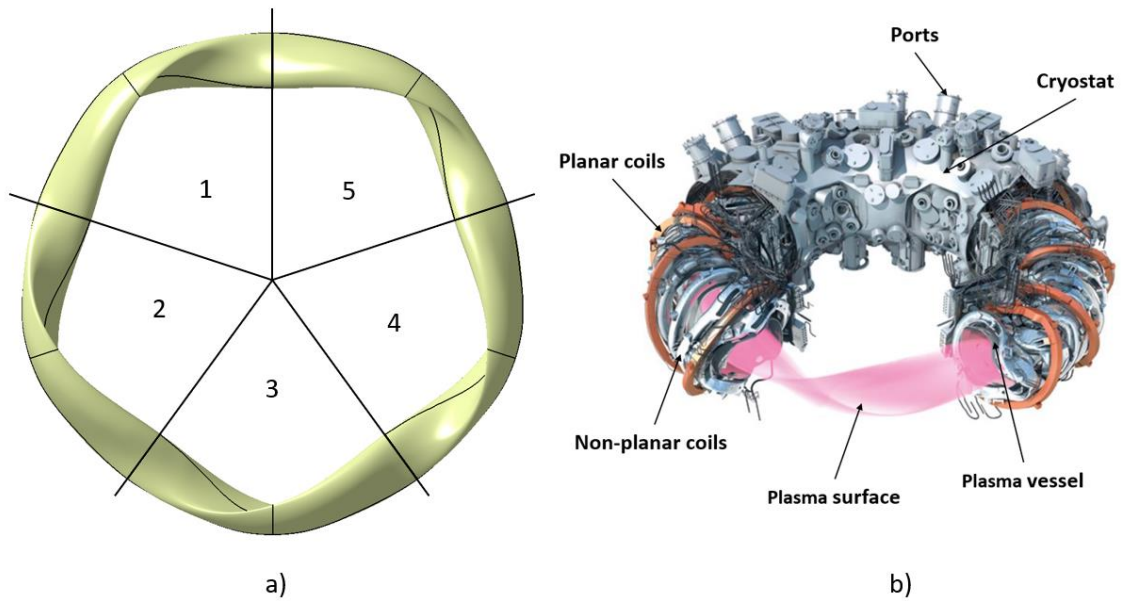
Figure 1.10. Left: schematic representation of the Wendelstein 7-X plasma as a five-fold mobius strip. Right: outline ot he W7-X stellarator. Pink color represents the plasma located in a vacuum vessel. 50 superconducting non-planar (grey) and 20 planar (orange) coils are showed. The cryostat covers the external superconducting coils [29]*.*

The outer part of the plasma vessel contains 253 ports, which are dedicated to different diagnostics and heating systems. Poloidal cross section of the W7-X is characterized by its different shape when rotating around the magnetic axis (see Figure 1.11) which changes from a 'bean shape' (φ = 0°) to a 'triangular shape' (φ = 36°).
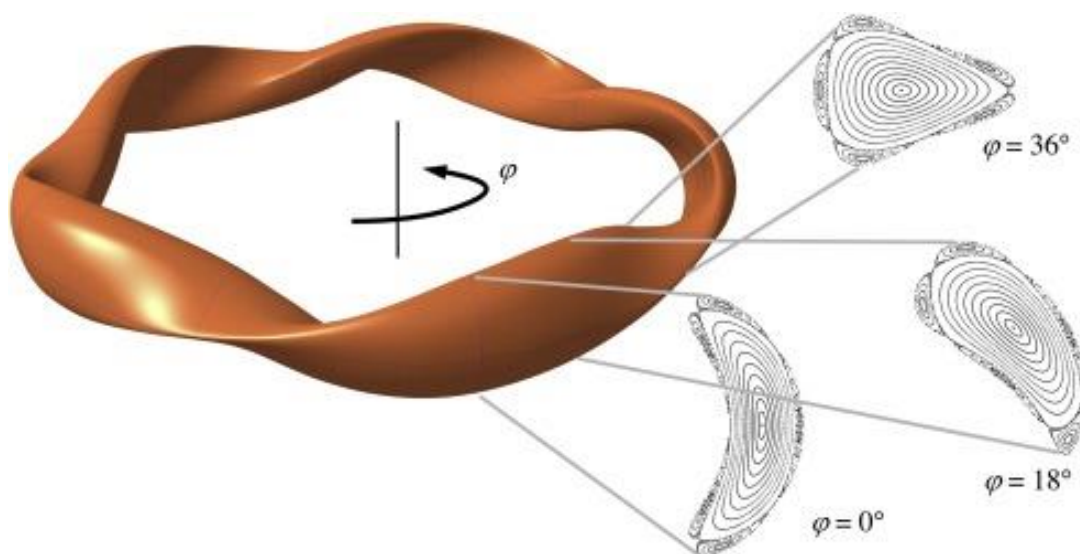
Figure 1.11. Last closed flux surface shape of the W7-X plasma. The bean-shaped (φ=0º), the φ=18º and the triangular (φ=36º) cross sections are indicated [29]*.*

Exploitation of the W7-X was divided into several operational phases depending on whether a limiter or divertor will be used. In fusion experiments, these are components placed inside the plasma vessel allowing exhaust of energy and plasma particles during the operation. In limiter configuration, the magnetic field lines of a plasma collide directly with the limiters' walls [30]. Divertors, on the other hand, are the specially equipped plates positioned at the plasma edge where plasma split and the energy and particles that moves to the restricted area of the vessel wall are 'captured' by the divertor plates [31]. Since divertors proved to be more efficient for good plasma confinement, they have become the most important exhaust system in fusion experiments.

Operation of the Wendelstein 7-X is planned to be held in four phases [32]:

1.   Setup for initial operation with limiter – OP1.1;

2.   Substantial extension of heating systems and the in-vessel components with passively cooled divertor – OP1.2a and OP1.2b;

3.   Subsequent operation of the machine with actively cooled divertor – OP2.0;

4.   Full performance of the device.

During the commissioning phase of the W7-X, the energy to the plasma was provided only by the electron cyclotron resonance heating (ECRH) system which played the main role for this task [33]. ECRH consist of 10 gyrotrons (each of frequency 140 GHz) serving as a microwave source – each providing power of 0.8 MW [32]. In the latter phases (OP1.2a and OP1.2b), the set of two neutral beam injectors (NBI) was installed [34]. Moreover, an ion cyclotron resonance heating (ICRH) [35] system is planned to be used during the next operational phase OP2.0 foreseen at the end of 2022– see Table 1.1.

Table 1.1. Major parameters of the Wendelstein 7-X stellarator [32].

Quantity	Unit	Stage 1	Stage 2	Stage 3	Stage 4
Plasma volume	m^2			30	
Major radius	m			5.5	
Minor radius	m			0.5	
Magnetic induction on axis	T			2.5	
Rotional transform	2π			$5/6\ldots5/4$	
ECR heating power	MW	4.3	8.5	10	10–15
ICR heating power	MW			1.5	3.5
NBI heating power H/D	MW		3.5	7/10	14/20
Heating energy	MJ	4	200	1000	18 000
Pulse length typ.	s	1–2	10–100	100–200	100–1800

Initially the stellarator was operated in the limiter configuration (OP1.1) based on 5 different graphite limiters positioned inside the plasma vessel. This setup guaranteed that the 99% of convective heat loads were deposited on the limiter's surfaces. The rest of W7-X inner surface was made of stainless steel and CuCrZr alloy.

In the next phases (OP1.2a and 1.2b) the divertor configuration with uncooled graphite shields and graphite divertor was applied. The divertors were mounted in the positions formerly occupied by limiters. According to the roadmap of bringing the W7-X operation to the higher level, the active cooling of the divertors are applied for the coming operational phase OP2.0.

During the OP1.2, the high-performance discharges were feasible only for a limited time (10 − 30 s). Longer pulses (~100 s) were performed for the lower plasma temperatures, hence its lower performance. The maximum plasma density planned to be obtained is $3 \cdot 10^{20}\ m^{-3}$.

1.3   Impurities in stellarator plasmas

Continuous monitoring of impurity level is critical to the proper operation of fusion reactors. It delivers information about e.g., plasma composition, energy radiated from the plasma or unwanted plasma-wall interaction.

The high-Z impurities, which are not fully ionized even in the plasma core, significantly affect the power balance, causing strong radiation losses from line emissions. The low-Z impurities, however, play a crucial role during plasma start-up, when the temperature is still quite low, and their radiation may disturb the plasma formation. Moreover, since high concentration of the low-Z elements can lead to unfavorable dilution of the plasma 'fuel', this may lead to a consequent degradation of a fusion power as they can reduce the likelihood of a fusion reaction. For these reasons, monitoring of impurities is a significant part of the proper operation of every fusion device.

Impurities can be described using two parameters:

a)   **Impurity density** (n_Z) being represented as a number of particles of a specific atom per unit plasma volume [m^{-3}].

b)   **Impurity concentration** defined as ratio of the impurity density to the electron's density in a unit plasma volume, $\frac{n_Z}{n_e}$.

Those notations will be consequently used in the latter sections of this dissertation where the numerical results are presented.

Impurities in the plasma, in most cases originates from the internal components of the plasma vessel. Such impurities are observed in the plasma consistently and hence are called intrinsic impurities. Even though plasma is very well confined due to the properly optimized magnetic field configurations, there is still a noticeable volume of a plasma outside the LCFS in the SOL region [36]. This plasma interacts with the plasma facing components what leads to the simultaneous occurrence of several effects: chemical and physical sputtering, evaporation, desorption, erosion, evaporation, melting/sublimation or backscattering. These effects were described in details in [37]. On the other hand impurities might also be injected on a special purpose (for impurity transport studies), hence they are called extrinsic (usually Ar, Ne, N or Fe).

Examples of light impurities present in the W7-X are e.g., carbon, oxygen, boron and nitrogen. Since they are of C/O monitor system interest the role of their monitoring is presented below.

Carbon is a dominant intrinsic impurity in the W7-X plasmas since the divertor as well as tiles installed on the inner plasma vessel are made of graphite. Sudden increase of its content in the plasma could be an indication of a plasma-wall interaction. Moreover, its monitoring would be a good indicator of the local overload of the plasma divertor plates.

Oxygen can be observed during every discharge, since its presence is associated with the machine venting, when the humidity from the air is adsorbed on the surface of the inner wall of the plasma vessel. During operation, oxygen is slowly released in time, penetrating into the plasma, and hence its content decreases over the experimental campaign. Therefore, its monitoring is an indication of the condition of the machine's inner wall.

In order to minimize impact of impurities on the plasma parameters, the inner wall and plasma facing components are covered by low-Z elements, e.g., by glow discharges. In the case of W7-X such element will be boron. Its content in the plasma is an indication of the quality of its layer on the vessel's wall. Significant increase of a signal can be a sign of a possible plasma-surface interaction. Its low level, however, may be a sign of a proper W7-X operation. On the other hand the quality of the layer decreases over time, and is associated with continuous decrease of its signal. Therefore the B layer needs to be renewed periodically and it is essential to monitor its quality over time.

An increased level of nitrogen might be an indication of a possible malfunction or a leakage in the vacuum system. Monitoring of its content may be also beneficial during dedicated experiments, when the nitrogen is injected into the plasma vessel e.g., in order to cool down the plasma edge.

1.4 Elementary processes in the plasma

1.4.1 Ionization and recombination

Ionisation may be the result of collision of an atom (ion) X^z with electron e. This process may be described as follows:

$$X^z + e \longrightarrow X^{Z+1} + 2e \qquad (8)$$

Another way of ionising atom may occur in a two-step mechanism by capturing of electrons. In this process an atom is excited above the limit potential, after which the autoionization occurs in order to reach an equilibrium state. This process can be described as follows:

$$X^z + e \longrightarrow X^{z*} + e \longrightarrow X^{Z+1} + 2e \qquad (9)$$
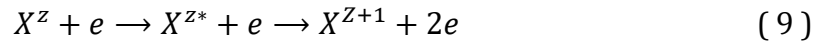
The reverse to the ionization is the recombination process. The reverse process to this is the three-body recombination, which involves ion and two electrons. In the case of recombination, the continuum radiation is emitted, however for the low-density plasmas (as in stellarators or tokamaks) this effect is negligible.

Radiative recombination is the process, when a positively charged ion captures free electron and radiates the excess energy as photon. Then the charged ion Z-*1* in the excited state j is formed emitting photon with energy $hv = \varepsilon + E(X_j^{Z+1})$.

$$X_g^z + e \longrightarrow X_j^{Z-1} + hv \qquad (10)$$

Where X_g^z is an ion with charge Z in the ground state g capturing free electron with energy ε. Radiative recombination with photon emission dominates for the relatively low plasma temperatures.

One on the possible channels for the dielectronic recombination process is capturing of free electron provides energy which is subsequently carried away by the promotion of a bound electron to another bound state, emitting the characteristic photon, related to the double excited state (**).

$$X_g^z + e \longrightarrow X_k^{(z-1)**} \longrightarrow X_j^{Z-1} + hv \qquad (11)$$
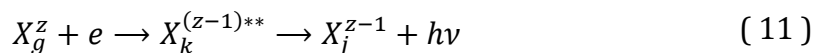
The dielectric recombination is the process reverse to the autoionization, which dominates at the higher temperatures above the specific ionization level. As a result of dielectric recombination, several photons might be emitted.

The 'charge exchange' recombination is a result of capturing the free electron from neutral atom by charged ion to the highly excited state according to the formula:

$$X_g^z + H_0 \longrightarrow X_j^{z-1} + H^+ \qquad (12)$$

In magnetic confined plasma devices, it occurs during plasma heat-up by Neutral Beam Injection (NBI) from which the electrons are captured by the ions of plasma impurities. This process is especially relevant for the low-Z impurities such as C, B or O. In MCF devices the total recombination coefficient of an ion with charge $Z(a_R^z)$ might be expressed as a sum of all above-described recombination coefficients according to the formula:

$$a_R^z = a_r^z + a_d^z + a_{CX}^z \frac{n_0}{n_e} \qquad (13)$$

where n_0 is the neutral beam density of hydrogen and n_e is the electron density.

1.5 Radiative processes in the plasma

To calculate the radiation spectrum emitted by the plasma, it is necessary to know the concentration of all ions and atoms together with electron temperature. There are three main emission types occurring in the plasma: free-free continuum radiation, free-bound continuum radiation and bound-bound (line) radiation.

- *Free-free* or *Bremsstrahlung* (from *bremsen* 'to brake' and *Strahlung* 'radiation') continuum radiation is a result of an electron interaction with an ion via the electric field. This interaction is associated with deceleration of a charged particle when deflected by another charged particle (electron or atomic nucleus). The loss of kinetic energy of a moving particle is subsequently converted into radiation (i.e., photons). The name 'free-free' refers to the fact, that the radiation is generated by free electrons (before) which remain free (unbound) after the photon emission, and initial as well as final state are not discrete states. Emitted spectrum is continuous since the photon

energy may be any part of the initial kinetic energy on electron. The described process is the main component of the continuous radiation since the ion-ion or electron-electron interactions impacts are negligible. The continuum radiation is emitted in very wide spectral range from infrared region to X-ray. The radiation loss power P_{brems} due to electron collision with ion per unit volume [36] is given by equation:

$$P_{brems} = 1.5 \times 10^{-38} n_e^2 Z_{eff} \left(T_e / e \right)^{1/2} \left[\frac{W}{m^3} \right] \qquad (14)$$

where the effective charge is defined as Z_{eff}:

$$Z_{eff} = \frac{\sum n_i Z_i^2}{n_e} \qquad (15)$$

Energy losses caused by free-free radiation is proportional to Z^2, and hence the Z_{eff} increases with impurity content in a plasma.

- *Free-bound* transition (recombination) occurs when a free electron is captured by an ion. The capture can be to the ground state and in this case a photon with an energy higher than the ionization potential of the atom or ion is emitted, as a consequence producing a band of continuous emission. The recombination can lead to an excited energy level with a photon emission, after which the electron cascades down to the ground state through the excited states. This produces emission lines which are characteristic to that atom or ion [38].

- *Bound-bound* (line) radiation is a result of an electron transition from higher-energy state of an ion or atom to the lower energy state. In consequence, a photon with energy equal to the energy difference between these levels is emitted. Because of the discrete character of atom energy levels, the radiated spectrum is linear. There are many possible transitions of each electron. Each of them represents a specific line that becomes visible in the emitted spectrum.

1.6   Ionization equlibrium models

In order to understand the emitted radiation, it is essential to know the excited states population. To provide comprehensive description about the radiation emission, it is necessary to solve the time dependent kinetic equations. There are three main

approximations used for the description of these phenomena: thermodynamic equilibrium model, corona equilibrium model and collisional radiative model. Dense plasma can be described using thermodynamic equilibrium model, while for the low-pressure plasma (i.e., MCF plasma) the collisional-radiative or corona model can be applied. A short description of those models is presented.

1.6.1 Thermodynamic equilibrium

In a complete thermodynamic equilibrium state of plasma, at any moment of time each process is accompanied by the opposite process. The density of excited states is proportional to the Boltzmann coefficient $\exp\left(-E_i/kT_e\right)$ therefore simultaneously the equilibrium distribution in the case of multiple ionization states is described by the Saha ionization equation (which is also associated with Boltzmann equilibrium) [39]:

$$n_e \frac{n_Z^{z+1}}{n_Z^z} = 2 \frac{g^{z+1}}{g^z} \frac{(2\pi m_e k T_e)^{3/2}}{h^3} \exp^{(-E_i/kT_e)} \qquad (16)$$

where g^z – the partition function of an ion with charge z, E_i – ionization energy of an ion with charge Z, T_e – electron temperature. The Saha's law is correct, when the plasma is considered a gas and in which the simultaneous recombination and ionization processes take place in the same way. Complete thermodynamic equilibrium is never reached in laboratory plasmas but can exist in the interior of stars [40]. Radiation would easily escape thus leading to unbalanced photon emissions and absorptions. In consequence, the Planck's law is almost never fulfilled for laboratory plasma. Therefore, for these plasmas the Local Thermodynamic Equilibrium (LTE) or partial Thermodynamic Equilibrium (pLTE) models are used.

1.6.2 Corona equilibrium

A simple approach is so-called corona model, which name refers to the solar corona. This is applied for the low-density plasma ($10^{18} - 10^{21}$ m^{-3}), e.g., in MCF plasmas. In this approach it is assumed that the balance between the recombination and ionization processes determines the stationary state of ionization, and the rate of recombination and ionization, as a result of collisions of electrons with ions is higher compared to ionic collisions. In this model, recombination with radiation emission (radiative and di-

electron recombination) is the predominant recombination process. It is also assumed that the stationary ionization state is not comparable with the thermodynamic equilibrium state. What is also important, the plasma, assuming corona equilibrium, is optically thin, i.e., transparent to radiation. The charge distribution is given by formula [11]:

$$\frac{dn_z}{dt} = n_e S_{z-1} n_{z-1} - n_e S_z n_z + n_e \left(\alpha_{z+1}^{rr} + \alpha_{z+1}^{dr}\right) n_{z+1} - n_e (\alpha_{z+1}^{rr} + \alpha_{z+1}^{dr}) n_z \qquad (17)$$

Subsequent components of the given equation describe the increasing number of particles in the Z state by ionization of particles from the lower ionization states, the decrease of their population by their ionization into higher ionization state, again increase of the population by the recombination from the excited state and decrease by the recombination to the lower energy state. Therefore, such equations need to be solved for each ionization state [11].

1.6.3 Collisional-radiative model and photon emissivity coefficients (PEC)

In order to describe less dense plasmas, the collisional radiative model (CR) is used. In contrast to corona model, the population of an excited state does not only depend on electron temperature but requires also taking into account the processes of electron collisions with atoms and higher charge states ions, including three-body recombination and excitation/ionization from highly excited bound-states. For electron densities $n_e \geq 1 \cdot 10^{23} m^{-3}$ the processes involving electron collisions happen more frequently than radiative processes [41]. The MCF plasma discharges exhibit electron densities in the domain in the range up to few $1 \cdot 10^{20} m^{-3}$. In the electron density range of $1 \cdot 10^{18} m^{-3} \leq n_e \leq 1 \cdot 10^{23} m^{-3}$ it is required to take into account all the populating processes. They can be described in a system of differential equations containing all (excitation as well as ionization) states of a given element, which influence the population of the considered state. The collisional-radiative model approach can be therefore represented by a photon emissivity coefficient (PEC) which include all the above-mentioned components (18):

$$PEC(n_e, T_e) = \frac{\epsilon}{n_e n_z} \qquad (18)$$

where ε – emissivity and n_z – density of the considered charge state.

The total emission $\epsilon_{i \to j}$ $(ph \cdot cm^{-3} \cdot s^{-1})$ [42] of a spectrum line consists of three contributions – excitation, recombination and charge-exchange. This is given by equation (19):

$$\epsilon_{i \to j} = \sum_{\sigma} PEC^{(exc)}_{\sigma, i \to j} N_e N_\sigma^{z+} + \sum_{\rho} PEC^{(rec)}_{\rho, i \to j} N_e N_\sigma^{(z+1)+} + \sum_{\rho} PEC^{(CX)}_{\rho, i \to j} N_H N_\sigma^{(z+1)+} \qquad (19)$$

where $PEC^{(exc)}_{\sigma, i \to j}$ corresponds to excitation, $PEC^{(rec)}_{\rho, i \to j}$ – recombination and $PEC^{(CX)}_{\rho, i \to j}$ charge exchange. Although PECs include also charge exchange component, it is not considered in this work, because under these experimental conditions the contribution of CX processes is negligible. Since the PEC based approach provide high precision dataset characterized with ease of its application, it became a powerful tool for the emissivity analysis. The PEC data for transitions important for this work are available at Atomic Data and Analysis Structure (ADAS) database [42].

1.7   Basis of impurity transport modelling

In the confined regions the Coulomb collisions are the elemental interactions between the plasma particles. The radial displacement of colliding particles results in convective (V) and diffusive (D) transport coefficients [43]. The characteristic step size which results from the collisions is the width of particle gyro orbits [44]. Along magnetic field lines the diffusion is orders of magnitude higher than in the radial direction perpendicular to the magnetic field lines ($D_\parallel \gg D_\perp$). As a consequence, the density and the temperature of a given particle population in the plasma is equalized on the respective flux surfaces and occurs on a significantly shorter time scale than the other components of particle transport. Such description of the colliding plasma particles is called classical transport.

Due to the toroidal geometry of the MCF devices, the characteristic particles' step size increases as a result of additionally formed drift forces [44]. This makes their bounce orbit to reach further across the magnetic fluxes. Such a behavior is also known as neoclassical transport. Its characteristic feature is the dominating radial (perpendicular)

transport, significantly increasing the $D_\perp$ above the level characteristic for classical approach. In the toroidal plasmas the neoclassical transport is always present.

To describe how strong the particle transport in a plasma is, the perpendicular to the magnetic field radial diffusion coefficient was selected. The change of diffusive behavior with the collisionality $\nu^* = \nu R/\iota V$, where v is the mono-energetic pitch-angle-scattering frequency, R is the major radius and V is the speed of the particles is presented in Figure 1.12 [45].

At a low collisional rate, when the size of the device is larger than the mean free path of a particle, some population fraction is trapped and move on a given flux surface. Since the ratio of a perpendicular and parallel kinetic energy is low, the particles tend to move around the closed magnetic flux surfaces. Such a particle's behavior is also called the Banana regime, since their orbit shape resembles the shape of a banana. As the particles' trajectories strongly depends on a magnetic structure of a device, therefore in this transport regime a clear difference in a level of neoclassical diffusion between tokamaks and stellarators is observed.

Due to asymmetric magnetic field configuration in stellarators, the particles can switch between magnetic fluxes, even when no collision occurred. As a consequence, a significantly stronger neoclassical transport (up to 2 orders of magnitude) is observed in stellarators compared to tokamaks.
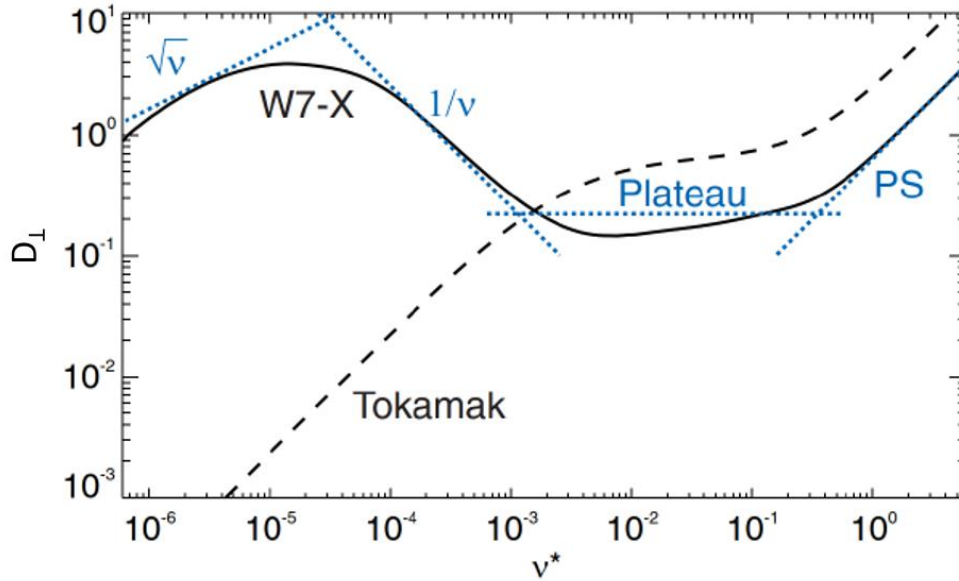
Figure 1.12. A diffusion coefficient perpendicular to the magnetic field lines (D⊥) versus collisionality (v)*
for W7-X stellarator (solid curve) and tokamaks (dashed curve) [45]*.*

At a high collisionality, the transit time of a trapped particle becomes longer compared to the characteristic collision time. Therefore, the kinetic energies of particles in a perpendicular direction may be high enough to escape its orbit becoming passing particles. Above $v^* \approx \epsilon^{-\frac{3}{2}}$ the mean free paths as well as the collision times are too short to allow particle transit its orbit undisturbed. This leads to its increased radial transport and is also called as Pfirsch-Schlütter regime. Since the particle orbits are no longer fulfilled, the impact of magnetic field configuration on a diffusion is strongly reduced. This results in the similar particle's transport both for tokamaks and stellarators at this regime. The transition between low and high collisionality regimes is called the Plateau [45], [46].

Experiments performed at W7-X showed, that in many cases the energy losses are up to an order of magnitude higher than its predictions derived from the neoclassical models [47]. This suggests that besides neoclassical transport there are additional effects that play a significant role. They are collectively named as anomalous transport to which the turbulent flows give a large contribution. Compared to the neoclassical model, the perpendicular component corresponding to the turbulent transport is generally much higher, hence often dominating the radial impurity transport.

Nevertheless, its basic mechanism is not yet fully understood and is still under investigation.

As the impurities have the significant impact on power balance in the plasma, their behavior needs to be precisely examined. As it is presented in the Equation (20), the simulation of the radial transport and emission of impurities is done by solving the radial continuity equation which is based on the law of particle conservation. For a given ionization stage, the transport equations are coupled with the ionization, recombination as well as charge exchange rates from and into neighboring stages. As a consequence, when all the impurity sources, sinks and their transport are well balanced, it means that the plasma is in steady-state form. Therefore, the transport times (due to the impurity transport coefficients (D, V)) parallel to the magnetic field are orders of magnitude higher than these perpendicular to the magnetic field. This makes it possible to assume the density of considered impurity constant on a given magnetic flux surface. As a consequence the radial impurity transport is a dominating factor when investigating the transport in the plasma. The reason for that are the variation of temperature and density gradients which are strongly correlated with the distance between the magnetic field surfaces. As a consequence, calculations of the radial impurity distribution based on the parallel transport with respect to the poloidal assymetries of magnetic flux surfaces can be performed.

The possibility of a highly charged impurities concentration with their strong central peaking inside the plasma core was observed a long time ago, at the early stage of the research on plasmas with magnetic confinement. These were predicted both for classical and neoclassical transports. Such a central peaking (called also impurity accumulation) refers to the situation when the amount of impurity ions in the specific radial position of a plasma (usually in the plasma centre) exceeds the number of ions in the rest of the plasma regions [44]. This may occur when the impurity source rate in a steady state plasma operation is high enough eventually leading to a performance problem. Other scenario, when the impurity accumulation can be observed, is when steady-state plasma conditions are not obtained (e.g., by continuous increase of impurity density), hence the source-sink balance cannot be reached within the given plasma conditions. This topic is especially important since the potential impurity

accumulation leads to a plasma dilution and enhanced power loss resulting in a fusion performance deterioration. Number of studies proved, that the impurity transport depends strongly on a plasma parameters. Therefore, to better understand these phenomena and hence to investigate impact of radial impurity distribution on the fusion plasma performance – the special methods needed to be included.

In this work, the pySTRAHL code [7] was used to investigate the impact of impurity transport in the plasma on the signals obtained in the C/O monitor system. The pySTRAHL code is a Python implementation of a well-known STRAHL code [48] devoted to the calculation of radial transport of a selected plasma impurity. It includes calculations of the collisional transport (referred to as neoclassical transport) as well as anomalous transport, in which additional effects (e.g., turbulence) are taken into account.

The code solves the radial impurity transport equation as a function of charge stage and effective minor radius of a given ion in 1 dimension (1D) based on the law of particle conservation.

$$\frac{\partial n_{imp}^{Z+}}{\partial t} = -\frac{1}{r}\frac{\partial}{\partial r}\left(r\Gamma_{imp}^{Z+}\right) + Q_{sources,imp}^{Z+} + Q_{sinks,imp}^{Z+} \qquad (\,20\,)$$

The radial covariant of the of component Γ_{imp} (impurity ion flux) is given by equation (21), where the impurity transport is defined by two coefficients – diffusion (D) and convection velocity (V).

$$\Gamma_Z^z = -D\frac{\partial}{\partial r}n_Z + Vn_Z \qquad (\,21\,)$$

The source/sink of a given impurity stage couples the transport equation of each ionization stage with the neighboring stages. This dependence is described by the equation (22). The S_{imp}^{Z+} represents the rate coefficient for a given impurity in ionization state Z, α_{imp}^{Z+} represents the recombination coefficient for di-electronic and radiative recombination and β_{imp}^{Z+} corresponds to recombination coefficient from charge exchange.

$$Q_{imp,Z} = Q_{sources,imp}^{Z+} + Q_{sinks,imp}^{Z+} = -(n_e S_{imp}^{Z+} + n_e \alpha_{imp}^{Z+} + n_H \beta_{imp}^{Z+})n_{imp}^{Z+} \quad (\,22\,)$$

$$+n_e S_{imp}^{(Z-1)+} n_{imp}^{(Z-1)+} + (n_e \alpha_{imp}^{(Z+1)+} + n_H \beta_{imp}^{(Z+1)+})n_{imp}^{(Z+1)+}$$

To run the calculations, pySTRAHL requires kinetic profiles (as a spline functions of experimental or theoretically established profiles), atomic data (e.g., from ADAS database [42]), the device geometry, radial profiles of the transport coefficients - diffusion (D) and convection (V) together with edge conditions (e.g., impurity source rate from inner plasma vessel).

This approach enabled to determine the impact of various radial impurity distributions on the emitted photon fluxes from the plasma. For that reason, the code was used to investigate the impact of two radial impurity distributions on the photon intensities observed by the C/O monitor system. The first one considered impurity accumulation (as observed in experiment *20181009.016*). In the further chapters this impurity distribution is called the 'peaked' profile. The second assumed uniform radial distribution of impurities which in the following chapters is referred to as the 'flat' profile. In both cases the total amount of the impurity was fixed at the same level. The experimentaly measured impurity profiles were provided by the Charge Exchange Recombination Spectroscopy (CXRS) system, a brief description of which is presented in section 3.2.4.

2 XUV spectrometer dedicated to low-Z elements study in the Wendelstein 7-X plasmas

In order to provide high quality data about the impurity content in experimental plasmas, an ideal diagnostic system should be characterized by:

- high energy resolution – to distinguish between ionization states of considered impurity species;
- high temporal resolution – to provide information about the impurity content in the very short time scale;
- high spatial resolution – to study radial impurity profiles in the plasma.

Information about the impurities in the W7-X plasmas are delivered by a set of diagnostic systems covering broad wavelength ranges, from visible to soft X-ray. The core impurity content is measured by the High-Efficiency eXtreme ultraviolet Overview Spectrometer system also called HEXOS [2], [49]. It covers wavelength range 2.5 – 160 nm delivering information with high-time (1 ms) and high-spectral resolution. Shorter wavelengths (4 – 0.06 nm) are measured by the Pulse-Height Analysis system (PHA) [4], [50] providing information about the impurity concentration, average electron temperature and Z_{eff}. There are also two X-Ray imaging crystal spectrometers called HR-XIS (High Resolution X-ray Imaging Spectrometer) and X-ray Imaging Crystal Spectrometer (XICS) [5], [6]. HR-XIS is intended for monitoring of spectral lines of injected tracer impurities (e.g., Si^{12+}, Ar^{16+}, Ti^{20+}, Fe^{24+}, Ni^{26+}). The XICS, however, is dedicated to measure Ar^{16+}/Ar^{17+} as well as Fe^{24+}/Mo^{32+} lines. It provides information about ion and electron temperatures profiles with high energy resolution of 20 eV together with a high precision information about poloidal plasma rotation measurements (+/- 5 km/s). Both crystal spectrometers deliver information with about 5 ms time resolution and a spatial resolution of 2 cm. Additional two diagnostic systems such as soft X-ray Multi-camera Tomography System (XMCTS) [51] and two bolometer cameras [52] observe plasma in a wide angle covering a total plasma poloidal cross section. Since they do not have energy resolution, their main purpose is to measure radiation asymmetries. In Figure 2.1 the energy ranges of the above-described impurity diagnostics at the W7-X are presented.
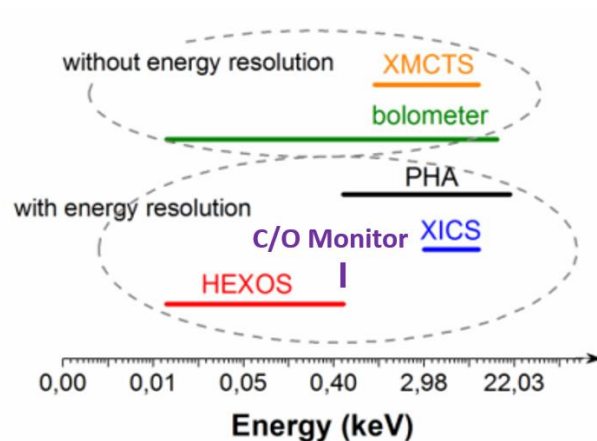
Figure 2.1. Energy ranges registered by the selected diagnostic systems at W7-X [53]*.*

To provide precise information about the light impurity content in the plasma, the XUV spectrometer called C/O monitor was designed.

2.1   General characteristics of the C/O monitor system

C/O monitor is a historical name, since the similar devices measuring the C and O lines were already used in the past e.g., at ASDEX-U [54]. However, in the case of the dedicated XUV spectrometer for W7-X also the B and N line intensities will be measured.

The system is characterized by its simple construction and is a dedicated tool for monitoring ions of selected light elements. It will be a high throughput system ensuring simultaneous measurement of all indicated elements with time resolution approx. 1 ms. Its purpose is to deliver information about the line intensities only, thus every change of the signal corresponding to the specific impurity measurement will suggest, that the total amount of hydrogen-like ion has evolved.

The system was constructed as a crystal spectrometer, based on the Johann geometry with cylindrically curved dispersive elements. Since its purpose is to deliver information about the line intensities and the continuum radiation, the application of polychromator is more appropriate than monochromator. This solution ensures the simultaneous measurement not only the line intensity of the specific element but also

its far wings (continuum). Such dispersive elements diffract selected wavelengths according to the Bragg's law [55]:

$$\lambda n = 2d sin\vartheta \qquad (23)$$

where λ - reflected wavelength, n – order of diffraction, d – spacing of the crystal's layers, ϑ – *angle of reflection.*

The Bragg's law describe the dependency of the crystal's structure with the wavelength of the incoming radiation and the angle of its incidence. When radiation interacts with crystal, the diffraction occurs at its every atom (see Figure 2.2). Knowing the wavelength of the incoming radiation and the spacing between the interplanar distance of the crystal's structure, the Bragg law defines the impact angle of the incoming radiation (θ) at which the constructive interference occurs.
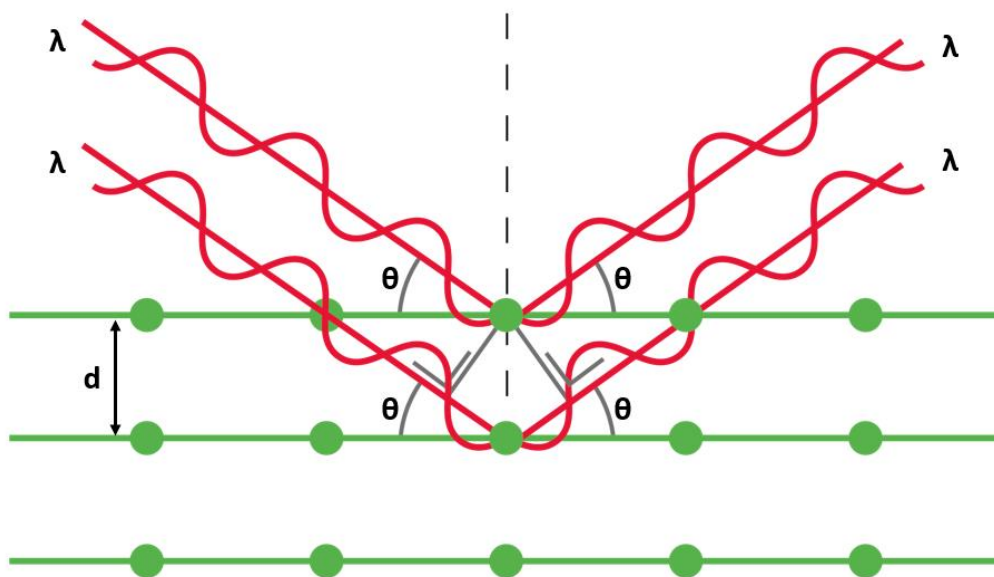
Figure 2.2. Schematic illustration of Bragg's law. λ represents the photon wavelength, Θ is angle of reflection and d represents spacing of the crystal's layers.

The rays which on the entrance side of the Rowland circle have common intersection point, when reflected from the dispersive element are subsequently focused on the detector's side of the Rowland circle at angles according to their wavelengths. The main principle of the Johann geometry is presented in the schematic Figure 2.3.
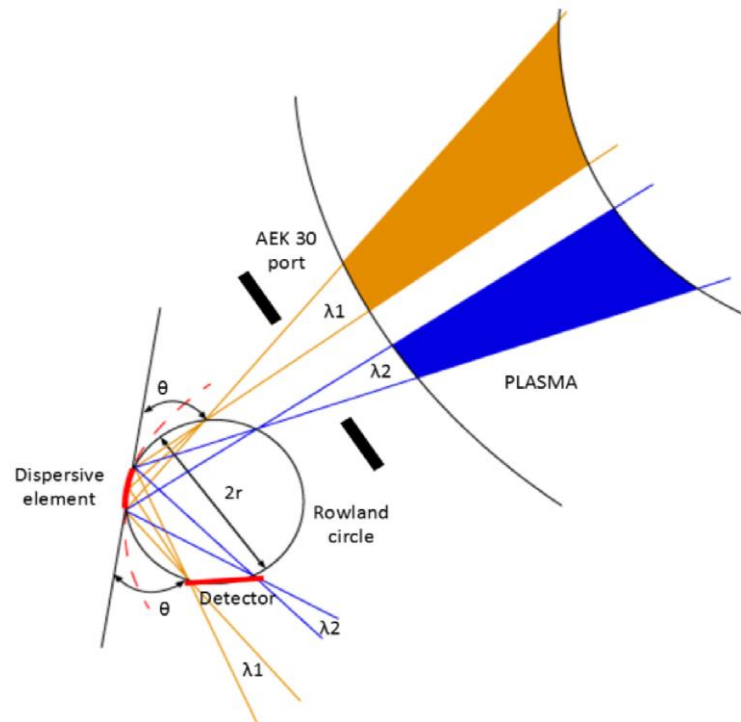
Figure 2.3. Johann geometry with Rowland circles radii [56]*.*

The construction with polychromators (in contradiction to monochromators) is characterized by broad acceptance angle, and hence providing energy resolved spectrum ensuring the measurement of the full spectral range including central line as well as its background. However, the price of such a solution is low spatial resolution. Adapting Johann geometry determines the detector's position as tangential to the Rowland circle. In the case of the C/O monitor, the detectors' positions are perpendicular to the reflected beam, though. This is non-standard solution resulting in de-focusing, which infers some degradation of the spectral resolution of the system. An important advantage of this approach is the freedom of choice of detectors (the design of some of them requires rather small input angle). Nevertheless, since the lines corresponding to the measured elements are clearly separated in their spectral ranges and including the fact that the discussed diagnostics is not going to investigate the line shapes, the assumed spectral resolution is sufficient for this purpose.

The system consists of two sub-spectrometer chambers, which are positioned one over another at nearly horizontal position at a distance approx. 3.2 m from the W7-X magnetic axis. Each chamber contains two independent energy channels dedicated to measurement of two ions: upper chamber will measure H-like carbon and oxygen line

intensities, while bottom one will measure boron and nitrogen. The lines of sight (LOS) of both sub-spectrometers crosses at the W7-X magnetic axis. The specific wavelength ranges of photons emitted from the plasma are reflected from the dispersive elements (depending on their incidence angle) towards the surface of the detectors active area. In order to avoid saturation and attenuate the intensity of the incoming light, the aperture system with vertically adjusted shutters is applied. The description of given requirements for this diagnostic and its detailed description is presented in the next sections.

2.2   The W7-X requirements for the C/O monitor system

Several requirements were defined at the start of the design process. First of all, a high magnetic field level reaching up to 2.5 T at W7-X magnetic axis needed to be taken into account. Its level decreases approximately exponentially with the distance from the magnetic axis, and above 3 m from the plasma center is reduced to approx. 75 mT. For that reason, the magnetic permeability of the material that the diagnostic is made of should be as low as possible in order not to perturb the stellarator magnetic field. The candidates for such materials were two types of steel: 316L and 316LN. Moreover, all the electronic components as well as the piezoelectrical drives used for shutters and crystals adjustment need to be able to withstand such conditions.

Since the absorption of the radiation is very high in the XUV range, the whole spectrometer needs to be operated in high vacuum (10^{-7} mbar) and be connected directly to the W7-X plasma vessel with no intermediate window that could absorb some of the incoming radiation. This, however, requires very efficient pumping system that meets substantial challenges. The turbomolecular pumps need to be grease free system, in order to avoid a possible hazard of sucking the grease into the vacuum chamber in case of the pumps failure. The solution is to use the vacuum pumping system with magnetic bearing. However, the high magnetic field level in the area of the spectrometer chambers may result in serious issues with its proper operation and even its potential damage. In order to avoid such hazard, the pumping system is shifted several meters from the spectrometers area, where the magnetic field is acceptable for this equipment (< 5 mT) – see Figure 2.4.
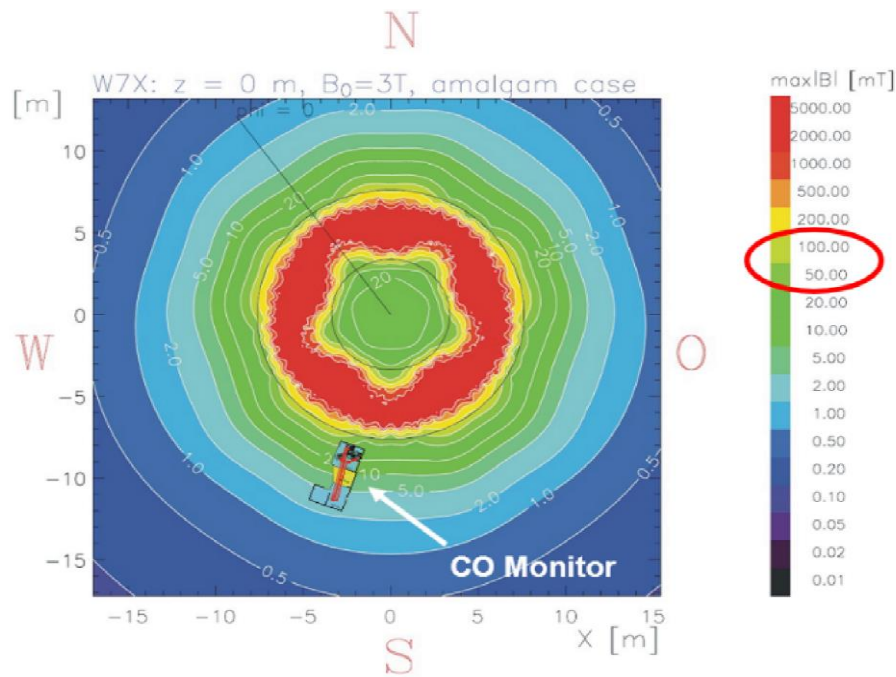
Figure 2.4. W7-X magnetic field distribution scheme with indicated position of the C/O monitor system [57].

Currently, there are several heating systems operating at W7-X e.g., Electron Cyclotron Resonance Heating (ECRH) [33], Ion Cyclotron Resonance Heating with frequency … and power (ICRH) [35] as well as Neutral Beam Injection (NBI) [34]. The ECRH heating system is the basic heating sysetem. It uses high-intensity microwave beams (with up to 10 MW power) of frequency of 140 GHz. The generated radiation, however, is not fully absorbed by the plasma, thus can be easily reflected by the inner walls of the plasma vessel, and hence may penetrate the diagnostic systems. This might be the reason of an uncontrolled heating of internal components and, consequently, leads to their damage. To protect the spectroscopic equipment from this kind of hazard, the dedicated shielding against ECRH stray radiation needed to be applied.

The detection system should be characterized by several features. Most important - it should be sensitive in the energy range of interest (energy range from approx. 250 up to 500 eV). Moreover, they should characterize with the ability for fast photon measurement with time resolution on the order of 1 ms. Finally, its detection area should be large enough to include the measure the spectral line with its far wings/associated continuum. As the requirements for the detection system are crucial, they will be discussed in more details in the further section (2.4.1).

2.3   Detailed description of the C/O monitor and its subcomponents

The system will be attached horizontally to the AEK30 port of the W7-X stellarator. Both of its vacuum chambers are positioned one over another in a nearly horizontal position (± 4.5°), what implies their relative angular position to be 9°, leading to crossing of their LOS at the W7-X magnetic axis. The whole system is supported by dedicated support structure with adjustment system (see Figure 2.5) ensuring precise angular positioning of both chambers independently as well as their relative linear position with respect to the W7-X port.
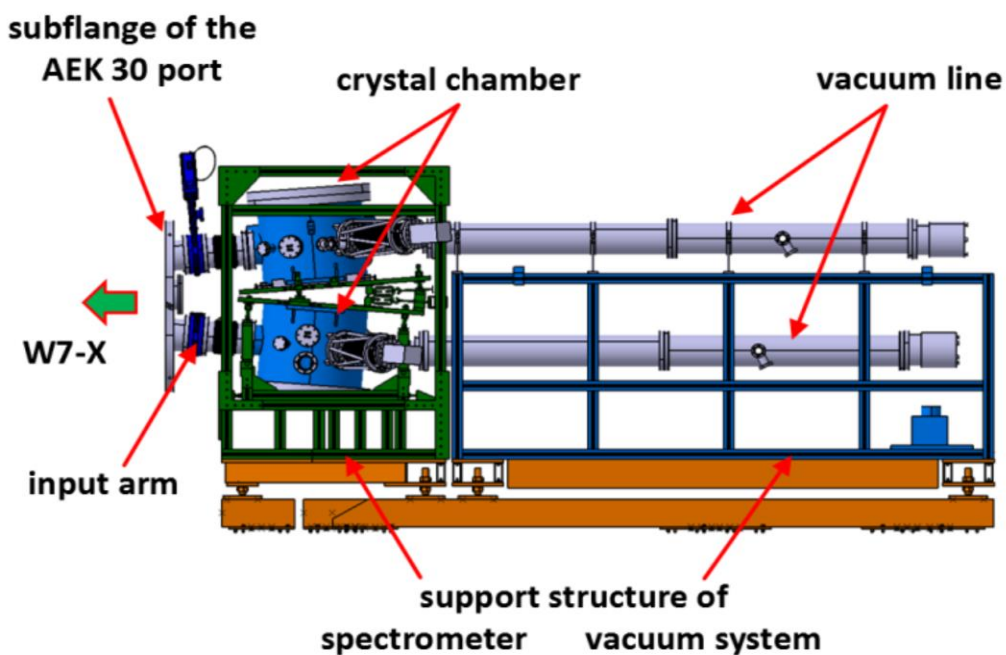
Figure 2.5. Assembly model of the C/O monitor system together with vacuum line, support structure and AEK 30 port flange [56]*.*

The outer diameter of each chamber is 510 mm and height is 440 mm. Total weight of the single vacuum chamber is expected to be approx. 200 kg. Each of them contains set of two dispersive elements with rotational piezoelectrical drives dedicated to the independent measurement of selected spectral line, collimator and two sets of adjustment units with variable apertures containing linear piezoelectrical drives (see Figure 2.6).
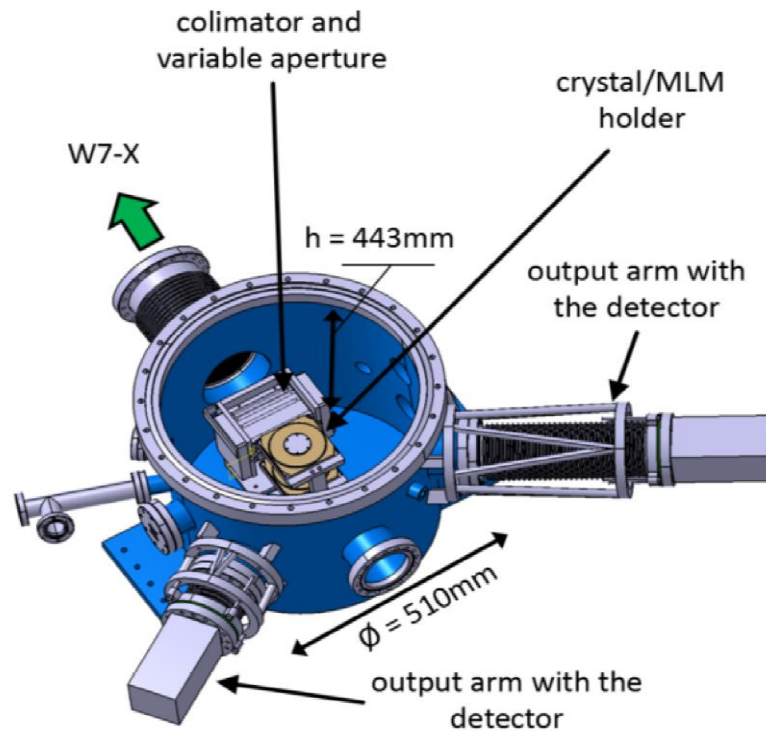
Figure 2.6. Sub-spectrometer with its internal components [56]*.*

Connection of both vacuum chambers with W7-X entrance port is provided by the use of gate valves and bellows, separating the spectroscopic units from the stellarator's plasma vessel. Applied bellows ensures the lateral movement in the range of ± 7.5 mm. Inside them, the two sets of microwave shields against ECRH stray radiation have positioned. This solution prevents the unwanted radiation from penetrating into the spectrometers sections, thus avoiding from damaging of internal components but at the cost of attenuating of incoming light by about 75%.

To obtain the strongest signal corresponding to the measured lines, appropriate type of dispersive elements needed to be applied. Since their reflectivity strongly depends on the reflected wavelength (according to the Bragg's law), the choice had to be performed for each energy channel separately. For the energy ranges corresponding to B, C and N Lyman-α lines, the multilayer mirrors (MLMs) has been chosen. However, since the O Lyman-α line is characterised by the shortest wavelength (1.9 nm), the contemporary MLMs production technology cannot provide high quality solution like in case of longer wavelengths. For that reason, it was decided to use TlAP crystal for O channel, which ensures sufficient reflectivity factor (see Table 2.1). All indicated

dispersive elements are cylindrically curved, in order to provide information not only about the respective line core, but also continuum radiation.

Table 2.1. Detailed optical parameters of the individual dispersive elements.

Channel	OVIII	N VII	C VI	B V
Line wavelength [nm]	1.89	2.48	3.37	4.86
Wavelength range [nm]	1.86 – 2.00	2.25 – 2.66	3.08 – 3.50	4.65 – 5.19
Radius of curvature [mm]	680	880	1720	1419
Bragg angle [degree]	48.05	29.71	24.94	29.07
Linewave-length[nm]	TlAP	MLM	MLM	MLM
Reflectivity [%]	≈ 5.7	≈ 6.3	≈ 25.7	≈ 25.5

Each dispersive element is 8 cm length and 2 cm height. They are positioned one over another by means of dedicated crystal holder as presented in Figure 2.7. The rotation axes of both crystals are collinear with axis of spectrometer chamber. Since the reflectivity strongly depends on the angle of incidents (AOI) of incoming radiation, it is essential to precisely set their positions (with precision of 0.2^{o}). For that reason, the rotational piezoelectrical drives are used.
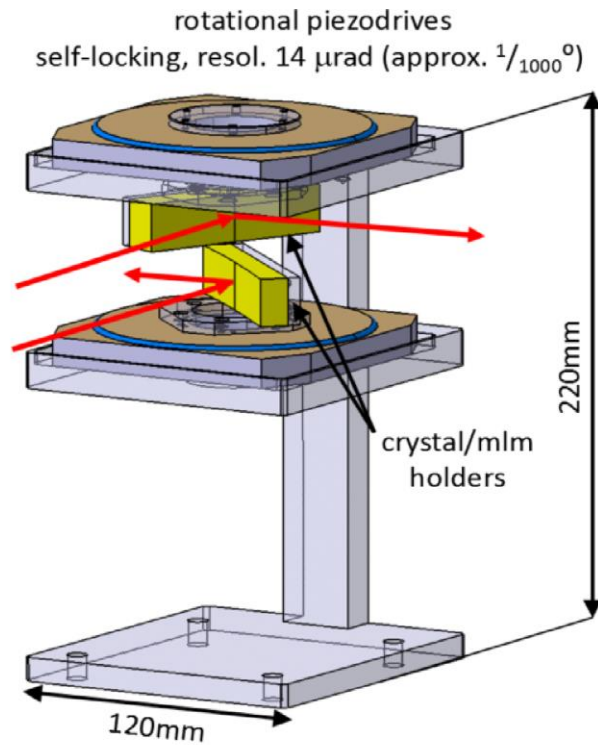
Figure 2.7. The design of the crystal holder with dispersive elements and rotational piezoelectrical drives. Red arrows indicate the direction of the incoming light [56]*.*

Their purpose is the fine-tuning of the MLMs/crystal angular position with high resolution (14 µrad), which is sufficient in the C/O monitor case. Once their correct angular position is found, they remain fixed until the end of experimental campaign.

Depending on the energy channel, the observed plasma region in a horizontal/toroidal direction (parallel to the W7-X magnetic axis) is slightly different and varies from 0.3 up to 0.5 m in the plasma center. The reason for the limitations referring to the different energy channels is the curvature of respective dispersive elements, dimensions of detectors active areas as well as the AEK30 port size. This is valid especially for the case of O^{7+} line observation due to the smallest curvature radius of dedicated crystal. However, in the vertical direction, the observed plasma volume is defined by multigrid collimator, designed as a set of horizontal slits with 1 mm spacing (see Figure 2.8) [56]. Applied solution allows for reduction of incoming radiation in a vertical direction down to acceptance angle which equals 1.43⁰. As a result, the height of observed plasma volume on the W7-X magnetic axis equals approx. 10 cm. Each set

of two collimators is dedicated to two energy channels and is positioned in front of the crystal holder.
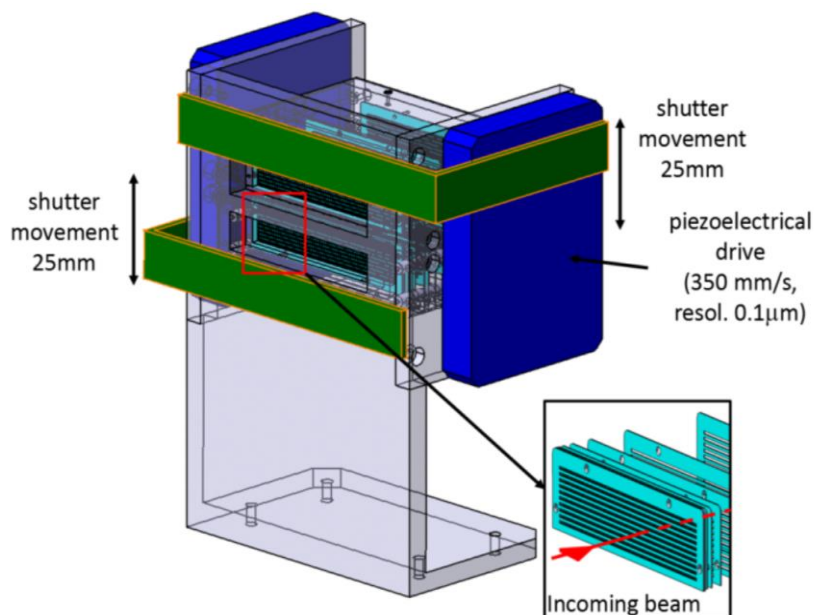
Figure 2.8. The design of the dedicated grid collimator [56]*.*

Application of such solution will reduce impact of a stray light to the negligible level, while providing the strong intensity of the measured line. Moreover, to attenuate the intensity of the incoming radiation and in consequence extend the dynamic range, independent vertical shutters for each energy channel are used. The applied solution uses the set of two linear piezoelectrical drives for shutter control, ensuring partial coverage of the slits and, in some cases, even cut-off the entire radiation.

The detectors are positioned at the output arms corresponding to the specific energy channels via bellows. Length of each output arm (and hence bellows) depends on the curvature of the respective dispersive element. Each detector is supported by dedicated supporting arms carrying the loads generated by their own weights and vacuum forces (see Figure 2.9). Moreover, this design allows for precise positioning of the detectors' photosensitive areas on the focal planes in the range of ± 2.5 cm. The advantage is the freedom of choice of the type of detector.
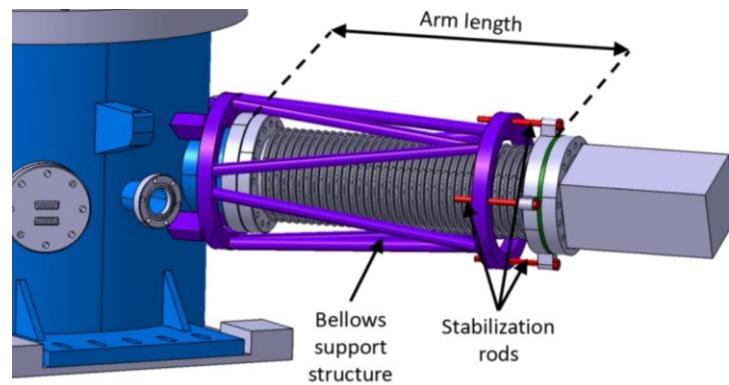
Figure 2.9. The design of detector's output arm [56]*.*

For the first C/O monitor operation several types of detection systems were under consideration. In the next section the detailed description of each solution is presented.

2.4 Choice of the detectors for observation of H-like ions of B, C, N and O

In order to obtain high quality data, the proper detection system needs to be applied. For that reason, several detector types were taken under consideration. Since each detection system needs to fulfil specific requirements given by the wavelength ranges of interest, as well as withstand the harsh environmental conditions of the W7-X, the whole procedure deserved special attention and is presented in the following sub-section.

2.4.1 General requirements for the detector

A proper detection system for the C/O monitor needs to meet several conditions. First of all, since the investigated lines are in the range of VUV/XUV (1.9 – 4.9 nm), the detection system should be characterized by relatively high sensitivity in that wavelength range. On the other hand, such detectors should be insensitive to other energy ranges (especially in the visible region).

Due to the internal parameters of the specific detection system and external distortions (originating e.g., from ECRH system), it might turn out, that electronic noise will be relatively high, reducing the signal to noise ratio (SNR) significantly. In order to

counteract this phenomenon, and to ensure relatively high SNR level (not less than 10), the quantum efficiency should be as high as possible.

The purpose of the diagnostics is a fast measurement of the plasma content, therefore the detectors should have a high time resolution (about 1 ms). Since a high quantum flux that reach the detectors' photosensitive areas is expected - the dynamic range should also be as high as possible. To avoid the necessity of performing frequent calibration – its sensitivity should not change over time. Otherwise, to provide qualitative information about the plasma content such system would require periodic cross calibration with other absolutely calibrated systems.

Size of photosensitive area is rather crucial when applying polychromator as a dispersive element. Therefore, to cover the line of interest together with its background (far wings), its length should not be shorter than 20 mm (recommended – 40 mm). Moreover, it would be beneficial if its height would cover the height of respective dispersive element (20 mm), but this is not crucial requirement. Since the line shapes are not of interest, the spectral and spatial resolution does not need to be high.

Since the C/O monitor will be positioned close to the W7-X vessel, where the magnetic field level reaches up to 100 mT, it is essential for the detectors to withstand such conditions. Usually this is not an issue, however, a strong magnetic field might distort the work of the cooling fans. Therefore, if external cooling system is required, a water-cooling system or other, more sophisticated cooling method need to be applied.

Finally – from the point of view of its future operation during experimental campaigns with deuterium as a working gas, significant neutron yield may occur. The detector should be able to withstand the neutron flux without affecting the measured signal when interacting of neutrons with photosensitive area, what in more serious case may even result in its damaging.

Taking all the aforementioned factors, it was essential to find the most suitable detection system. These considerations included Micro Channel Plates (MCPs), gas detectors (MSGC, GEM) and CCD cameras. All of them are characterised by specific properties, which are presented in the next sub-sections.

2.4.2 Considered detection systems

The first option under consideration were Micro Channel Plates (MCP) [58] – commonly used on other machines (e.g., HEXOS at W7-X [49] and KT4 at JET [59]). The micro channel plates are connected to a phosphor screen image intensifier. The general principle of its operation is multiplication of photoelectrons produced by the incoming radiation.

Once a photon reaches MCP channel, it produces the photoelectrons which are subsequently multiplied in the microchannels. An amplification of emitted photoelectrons depends on the voltage applied to MCPs, which might increase even by a factor of 10^4. An output electrons are subsequently accelerated and focused on the phosphor plate (luminofor) by additional voltage. Applied voltage is also responsible for the increase of energy conversion on the phosphor plate (see Figure 2.10). Its time resolution strongly depends on other subcomponents such as fluorescence lifetime of the luminofor or readout electronic.
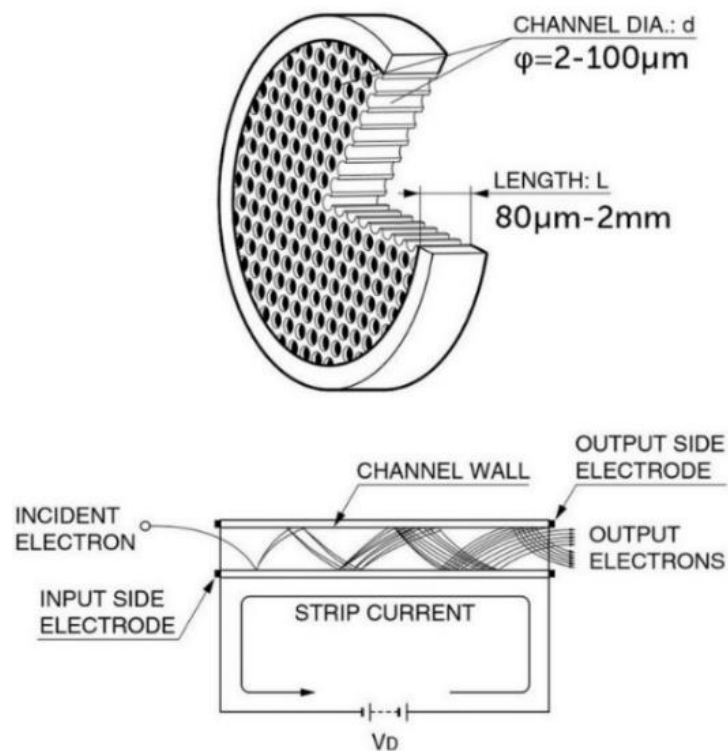
Figure 2.10. Design of the multi-channel plate detecto [60].

The detection system based on the MCPs might be a good choice since they provide high photoelectron multiplication factor, guaranteeing high level of a signal to noise ratio. Another advantage would be its high sensitivity in the energy ranges of the diagnostics interest.

MCPs, however, have several drawbacks that need to be considered. First, the MCPs sensitivity is high at their commissioning phase, however, decreases over time. Therefore, to provide reliable quantitative information about the impurity content, it is required to periodically calibrate them. Moreover, when operating the MCP detectors, the system needs to be constantly under low pressure (10^{-6} mbar). The sudden loss of vacuum may lead to detector damage. For that reason, it is required to apply an additional safety system, ensuring high-voltage cut-off when the sudden pressure increase will be detected, and/or the use of dedicated efficient pumping system, ensuring proper pressure level for the detectors [49], [61]. Moreover, the neutron yield associated with deuterium plasmas may have an impact on the signals and even destroy the detectors. Therefore, an additional neutron shielding (made of e.g., polystyrene) need to be applied.

An alternative for the forementioned solution based on MCPs could be a gas detector in a type of proportional counters – Multi Strip Gaseous Chambers (MSGC). Such solution is successfully applied at e.g., ASDEX tokamak (Axially Symmetric Divertor Experiment) [62], [63] as well as similar diagnostic system KS6 at JET (Joint European Torus). The principle of its operation is based on the ionization of a gas in the chamber (usually Argon with small admixtures of quenching gas) by incident photons. Due to their small structures, they can provide a high rate capability as well as very good spatial resolution.

The primary electrons are accelerated in high voltage electric field and then generate the electrical signal which is proportional to the deposited photon energy. On the one hand, the low energy photons does not transfer enough energy to ionize the gas. On the other, the high energy photons can pass through the gas due to the lower cross-section for any collision in unlike to XUV photons. This allows to construct the detectors ensuring high sensitivity level in the selected energy range. Moreover, in

contrast to MCPs, the sensitivity of gas detectors does not decrease over time and they are also insensitive to neutron yield.

Detector's efficiency depends strongly on the transmission of its entrance window (e.g., 0.9 μm thickness Mylar foil with 100 nm of aluminum coating) separating the vacuum area inside the spectrometer from the detector's gas filled chamber. However, due to the significant pressure gradient (~ 1 atm.) between the vacuum area and gas chamber – there is a meaningful risk of possible leakage of a gas or even rapture of a window. This might lead to an uncontrolled pressure increase inside the spectrometer's chambers and leakage of a gas into the plasma vessel. Therefore, to avoid such hazard, an additional safety system with feedback between the vacuum gauges and the main gate valve should be used. Moreover, the MSGC are characterized by relatively low amplification factor (approx. 100), as well as dynamic range, thus would require frequent radiation influx adjustment using variable aperture.

The partial solution of the aforementioned drawbacks would be application of the gas electron multiplier (GEM) [64], [65] detectors as they offer much higher amplification factor as well as dynamic range. Alike MSGCs – GEM detectors do not suffer from neutron impact what is an advantage of their application. However, similar to typical proportional counters, the problem with working gas in GEM detectors, and hence its possible leakage into the vacuum chamber remains unsolved. Taking all those into account, the GEM detectors are considered for the latter phase of the W7-X operation when deuterium plasmas are going to be investigated.

Another considered detector types were the commercially available CCD cameras, successfully applied in other plasma diagnostic systems (e.g., VUV spectrometer at LHD [66]. One of the considered CCD camera models was provided by the Greateyes company (model ALEX-s 1k256 [67]), ensuring linear response (better than 99%) as well as sensitivity in the energy range of interest increasing from 60 up to 90% (see Figure 2.11).
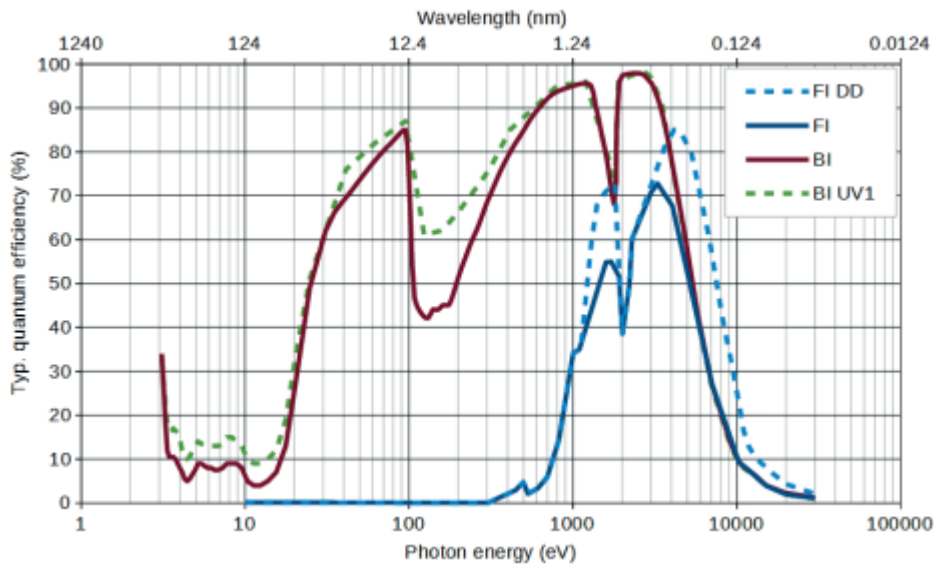
Figure 2.11. Quantum efficiency of the Greateyes CCD cameras different models as a function of photon energy [67]*.*

The described model has maximum full spectrum readout above 1 kHz, corresponding to the time resolution ~1 ms. Another important aspect is its detection area with a size of 26.6 mm x 6.7 mm (resulting in its active area of 178.22 mm^2), which is sufficient to cover the line of interest together with its background.

However, the considered CCD camera has relatively high sensitivity in the range of visible light. In extreme cases this may result in detector's saturation (or even blinding the system) if some heat load would occur on the inner wall of the plasma vessel leading to the increase of a background level. Moreover, alike MCPs, the CCD cameras are vulnerable to neutron flux which may appear in the latter phase of operation when investigating the deuterium plasmas. Since it is difficult to predict their resistivity and lifetime when working under such conditions, the implementation of neutron shielding housing for each detector might be a solution.

Taking into account the features of described detector types it was decided that the CCD cameras will be applied for the initial phase of the C/O monitor, due to their high sensitivity in the energy ranges of interest and commercial availibility. Nonetheless, for the future experimental campaigns with deuterium plasmas as a working gas, other detector types will also be considered.

3 Numerical code for modelling of the C/O monitor signals

C/O monitor is a high throughput system with large acceptance angle in poloidal/horizontal direction (even above 11° for the observation of O Lyman-α line - according to the Johann optical set-up) and approximately 1° in radial (vertical) plane for all channels. The W7-X is constructed as complex five-fold symmetric device (see Figure 1.10) with poloidal cross sections changing from shape similar to bean to close to triangle (see Figure 1.11). For that reason, the observation of different poloidal regions contributes to a different wavelength of the obtained signals. This implies a wide range of the observed plasma including the W7-X magnetic axis, as well as broad range of edge plasma regions, but at a cost of a poor spatial resolution. A top view along with an isometric view of the observed plasma volume (for C and O channels) is shown in Figure 3.1.
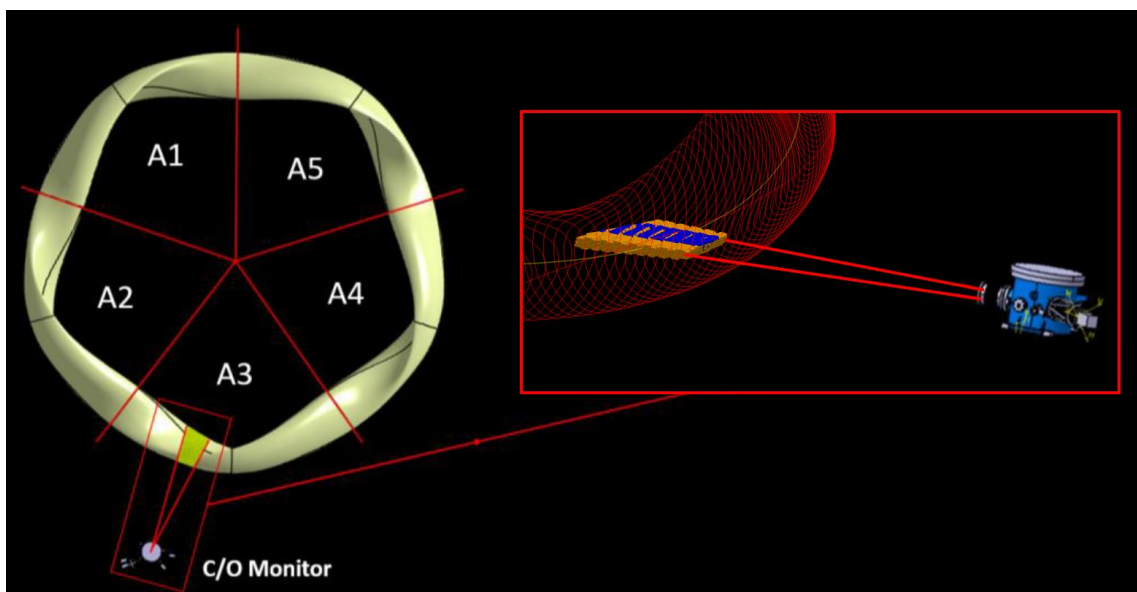
Figure 3.1. Top-down view on the last closed-flux-surface of the W7-X with the C/O monitor included. The zoomed part presents isometric projection of the upper sub-spectrometer chamber, as well as its acceptance angle and the observed plasma volume.

The implication of the above fact is the origin of the radiation emitted by significantly different plasma regions with various range of temperatures and densities. Moreover,

the observed plasma volume for each channel is slightly different what may result in differences of the total radiated photon intensities between them.

Since the emissivity of low-Z elements strongly depends on the plasma kinetic parameters, especially at low T_e ranges (closer to the edge plasma), where maximum emissions of these lines are observed - it is essential to compare experimental results with simulations. Moreover, it is also important to understand impact of systems geometry on the obtained signals (e.g., shutters, collimators or dispersive elements angular positions). Therefore, to better understand the experimental results, the dedicated simulation code in Python was developed. For the emissivity calculations, the code implicitly assumes corona equilibrium without impurity transport. However, it is possible to include impurity transport by using the pySTRAHL code, with which it is integrated. The results provided by the code can be regarded rather as qualitative. In order to obtain precise quantitative information, the system needs to be calibrated (e.g., cross calibrated with other systems as CXRS or HEXOS). What was already mentioned, the system is going to measure not only the intensity of the particular Lyman-α lines, but also their background. Nevertheless, due to the qualitative character of performed investigations, the code is focused on calculations of the line intensities only.

3.1 Description of the code

The main purpose of the code is to compare experimental results with theoretical assumptions, and deliver results based on the given experimental conditions. The calculated results will be cross checked with other diagnostic systems (e.g., CXRS, HEXOS), to provide high-quality information about the impurity content in the plasma. In order to efficiently handle this task, the code should characterize by a relatively fast computing time and the highest possible precision of the performed calculations. Those requirements are not easy to be fully guaranteed when operating on a relatively limited computing power, therefore the compromise between its speed and precision needed to be found. Moreover, from the development point of view - the code should be easy to maintain in order to quickly implement significant improvements/changes and should be easy to operate by a regular user. In the next part of this section its detailed description is presented.

The code is divided into three main modules:

- **Geometry and ray tracing** – represents the basic geometry of the system and performs the ray tracing calculations;

- **r_{eff} readout** – calculates effective radius (using VMEC code) of each discreet point representing considered plasma volume;

- **Emissivity** – calculates the emissivity of each discreet plasma point represented by r_{eff} values and integrates the signal over the observed volume by each energy channel separately;

Each of these points is dedicated to solve different task, therefore in order to perform thorough numerical investigation, they should be used in the presented sequence. However, it is possible to perform specified operations independently if appropriate input data is provided.

3.1.1 Geometry calculation

In order to precisely investigate the obtained experimental results, it is essential to provide numerical spectrometer's representation and perform comparable calculations also taking into account the geometry of the system and enabling ray tracing operation. It is especially important since the construction of the C/O monitor system is based on Johann geometry with large observed plasma volume. For that reason, the geometrical module which thoroughly reflects the design of the device was created. Its development and precise input parameters describing the internal diagnostics sub-components ensures the way to calculate very subtle differences in the observed plasma volumes by all energy channels separately.

In general – the main task of this module is to perform the ray tracing of the radiation emitted by the given plasma volume and examine, whether each of investigated radiation beams is reflected by the specific dispersive element, hence reflecting the beam towards the detectors active area.

To represent particular component of the diagnostics it needed to be defined in the cartesian coordinate system using the CAD (Computer Aided Design) model. The base point of the considered coordinate system defines its origin [0, 0, 0] and refers to the x, y and z dimensions. It is positioned in the central point of the W7-X torus. The z

coordinate represents vertical direction, perpendicular to the toroidal plane of the W7-X while x represents the horizontal East-West direction and y represents horizontal direction perpendicular to x.

Each component as well as observed plasma volume has its numerical representation and is used in the latter phase for ray-tracing calculations. Therefore, several main numerical sections representing diagnostic's subcomponents, essential from the point of view of the observed plasma regions are included. The indicated components are: AEK30 port, ECRH protection shields, collimators with shutters, dispersive elements and detectors. Numerical model of each part required different approach and is described together with the step by step calculation procedure.

3.1.2 Plasma volume determination

The first step is to determine the plasma volume investigated in the subsequent parts, defined by the input solid angle. For this purpose, the general volume of the plasma will be described by equally spaced points. The distance between points can be varied/modified, but by default it is assumed to be 1 cm, hence each point of this mesh represents the 1 cm^3 volume. At the initial calculation phase a cuboid volume much larger than observed plasma is considered. In the next step the investigated volume is trimmed to reduce the number of points by cutting-off the regions that are definitely not in the area of observation. As a result, the considered bulk is significantly decreased, reducing the number of input points required for the further calculations. This step (reduction of the cuboid's volume) is not strictly required from the numerical point of view but is essential to significantly speed up the computing process.

3.1.3 Numerical representation of system's subcomponents

3.1.3.1 W7-X port and ECRH shield

Representation of the AEK30 port is described as a set of cartesian coordinates and even though the LOS of the system is not 'cutting' the edge of the port, it is included for the initial reduction of the calculated volume. This step accelerates sequent calculations by reduction of the point cloud investigated when performing final ray tracing procedure.

As an ECRH protection shield against stray radiation, two grids are mounted inside the entrance arm/bellow which connects diagnostics to the W7-X vacuum vessel. Since the ECRH shields will reduce the incoming signal by approx. 75%, implementation of their numerical representation is important. Such reduction factor could be assumed as fixed value, however, due to the large acceptance angle of O and N dispersive elements, there is a risk, that part of the incoming radiation goes beyond the area of ECRH grids, thus might be blocked, leading to the attenuation of incoming radiation. For that reason, it was essential to include information about the shields' dimensions in the model.

3.1.3.2 Collimators with shutters

The vertical (not a dispersion) angle is defined by a grid collimator with 10 grid planes and 1 mm grid spacing (presented in chapter 2.3). Its appropriate modelling was essential not only from the operational point of view (by defining the observed plasma region as well as provide information about the light flux reduction when using the particular shutter position), but also is necessary for the estimation of intensity signal collected by the detectors. Shutter's closing position provides information about the percentage of incoming radiation reduction, and hence currently observed plasma volume, thus increasing the precision of calculations.

The procedure of transmission checkout is similar to the ECRH protection shield case – each of 10 cuboids (yellow parts – Figure 3.2) represents the vacuum volume where the radiation transmission is possible (not limited by collimator's grids). The ray crossing front plane of a single cuboid representing the aforementioned vacuum volume must leave it at its backside plane. Each of 10 cuboids are considered separately. This approach allowed to simulate the transmission of radiation through the collimator and reduce the number of points representing the volume of the observed plasma.
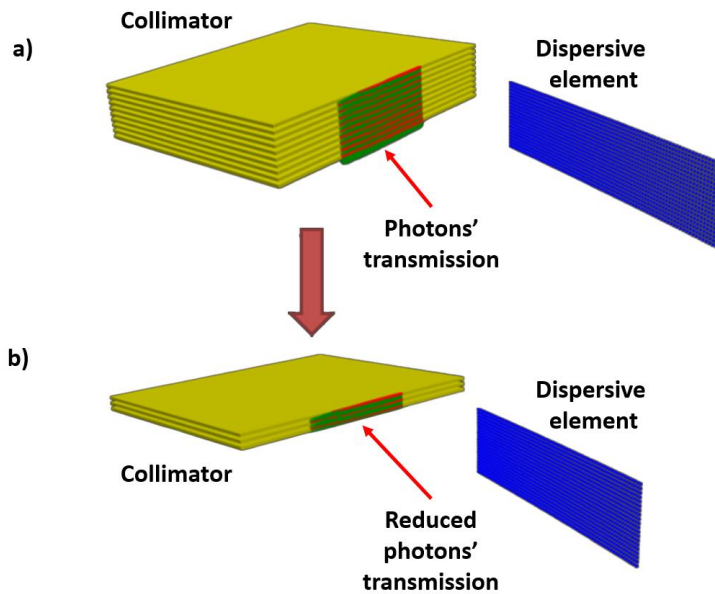
Figure 3.2. A scheme of the numerical representation of photon transmission through a grid collimator: a) shows fully opened apertures, b) apertures 70% closed.

This is an ideal situation assuming the highest possible manufacturing precision. In reality, however, the collimator is affected by small deviations of the grid resulting in unintended transmission of a light reaching the surface of the detectors at the angle different than ±1 degree in the vertical direction. This implies rather different observed plasma volume (but not significantly) and hence might have an impact on the output signals.

3.1.3.3 Dispersive elements

Further step was to create a numerical representation of the dispersive elements. The model includes basic parameters in cartesian coordinate system containing coordinates of crystals' vertices, radius of cylindrically curved surface, coordinates of the circle center tangential to the crystals' surfaces and the orientation vectors. With this set of information, it is possible to create their discrete representation (see Figure 3.3). All the required data are stored in a separate file, being also a coordinates database of other subcomponents. The only thing that needs to be specified by a user is the implementation of the measuring channel as well as accuracy of the crystal's surface grid. This is done by the implementation of points number representing crystals height and length. Since too high precision results in a significant (exponential)

increase of computing time, to perform calculations with reasonable precision and in possibly shortest period, the optimal grid accuracy step adequate to the computing power needs to be found. Numerous calculations showed that the most optimal setup in order to enable relatively short computing time and high precision is to define crystals' length up to maximum 200 (but not less than 100) and height up to 80 points.
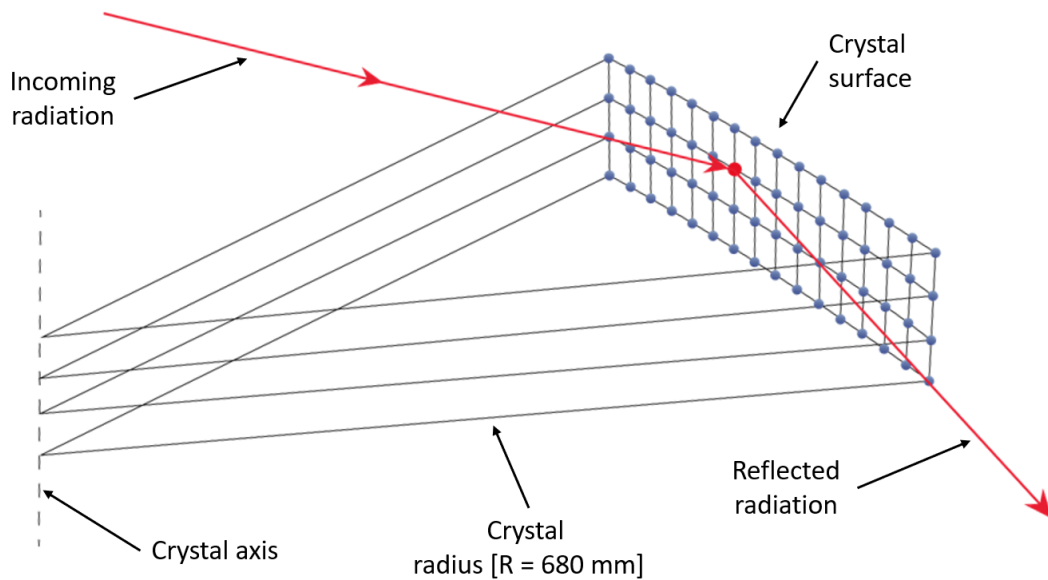
Figure 3.3. Numerical representation of the cylindrically curved crystal dedicated to the measurement of O line (R = 680 mm).

Each dispersive element is associated with its unique rocking curve in the shape of gaussian profile as presented in Figure 3.4. These are included in the dataset and are applied for calculating the fraction of reflected incidence photons. Since the reflectivity strongly depends on the AOI (angle of incident), it needs to be included into the model.
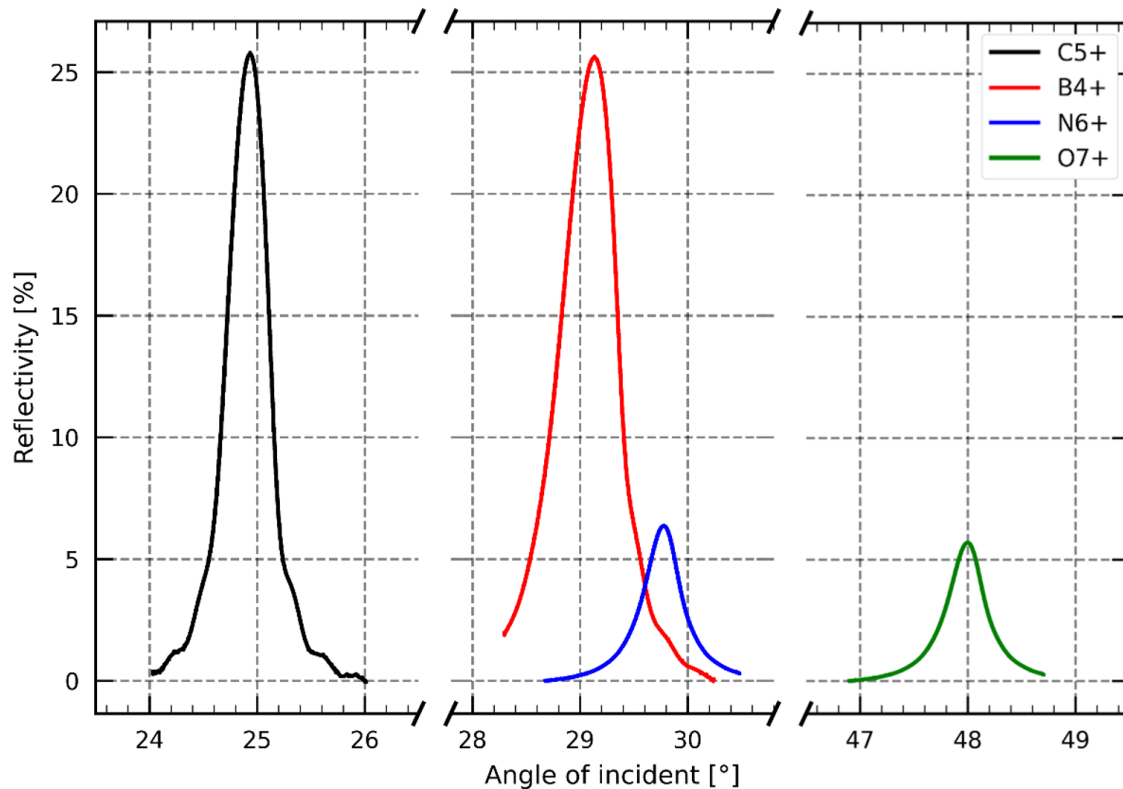
Figure 3.4. Rocking curves of all dispersive elements reflecting B (red), C (black), N (blue) and O (green) Lyman-α transitions.

When the AOI is calculated, the reflectivity is automatically checked – this is described in details in the latter section.

3.1.3.4 Detectors

The last diagnostic's subcomponent included in the code is a detector. Its numerical representation is important since the observed plasma region depends strongly on its relative position towards the respective dispersive element. Since the height of the selected detectors' active areas are significantly lower than the height of the crystals (6,7 mm compared to 20 mm of the crystal's height), means that not the whole plasma radiation reflected by the respective dispersive element will be covered by the detectors. Therefore, it is essential to investigate how much of the emitted light reflected by the crystal is visible and how even a small shift in its position can affect the output signal. For these reasons, the geometric representation of the detectors was introduced. The approach adapted here is like the one used in previously described modules, and is based on the designation of plane's equation, so called hull

volume (volume in space) and gathering information about the rays crossing the plane inside that hull (respective plasma coordinates, AOI towards the crystal, plasma-crystal distance etc.).

3.1.4 Ray tracing calculation

The main module is the 'simulation' part. Its purpose is to create the numerical representation of all the components, i.e. plasma volume, dispersive elements, detectors and components of the optical system as detector, collimator, aperture etc.. The way, that final data array (matrix containing all obtained information) calculation is performed is presented in this section.

The code initially defines numerical description of represented plasma volume (as it was indicated in the section 3.1.2). Table 3.1 presents the exemplary data array format with plasma points in cartesian coordinate system. The '*idx_sel_plas_points*' represents the corresponding index numbers of a plasma. Each index of a plasma point refers to the unique plasma volume represented by a set of 3 float numbers describing its location in 3D space (x = '*plasma_x*', y = '*plasma_y*' and z = '*plasma_z*').

Table 3.1. Schematic of the data array with plasma coordinate in three-dimensional space with corresponding index column assignments.

idx_sel_plas_points	PLASMA COORDINATES		
	plasma_x [mm]	plasma_y [mm]	plasma_z [mm]
pp_1	0	0	0
pp_2	1	1	1
pp_3	2	2	2

In the next step, the code calculates coordinates of the selected dispersive element corresponding to a specific spectral line channel and returns the data in a similar form. Table 3.2 presents schematic data array containing index number of each crystal's point ('*idx_crys_points*' – 1st column) and corresponding three columns ('*crystal_x*', '*crystal_y*', '*crystal_z*'). Alike in data array with plasma point cloud representation, each index ('*pc_1*' – '*pc_5*') corresponds to a different crystal point represented by a set of 3 floating numbers referring to its position in space.

Table 3.2. Schematic of the data array containing the coordinates of the crystal points.

idx_crys_points	CRYSTAL COORDINATES		
	crystal_x [mm]	crystal_y [mm]	crystal_z [mm]
pc_1	1	1	1
pc_2	2	2	2
pc_3	3	3	3
pc_4	4	4	4
pc_5	5	5	5

Next, the code combines each of the plasma locations with all the points representing the surface of selected dispersive element. In the Table 3.3 exemplary combination data array product is presented.

Table 3.3. Schematic of the data array containing combination of all plasma coordinates of the plasma (yellow columns) and crystal points (blue columns).

Nr	idx	PLASMA COORDINATES			idx	CRYSTAL COORDINATES		
		plasma_x [mm]	plasma_y [mm]	plasma_z [mm]		crystal_x [mm]	crystal_y [mm]	crystal_z [mm]
1	pp_1	0	0	0	pc_1	1	1	1
2		0	0	0	pc_2	2	2	2
3		0	0	0	pc_3	3	3	3
4		0	0	0	pc_4	4	4	4
5		0	0	0	pc_5	5	5	5
6	pp_2	1	1	1	pc_1	1	1	1
7		1	1	1	pc_2	2	2	2
8		1	1	1	pc_3	3	3	3
9		1	1	1	pc_4	4	4	4
10		1	1	1	pc_5	5	5	5
11	pp_3	2	2	2	pc_1	1	1	1
12		2	2	2	pc_2	2	2	2
13		2	2	2	pc_3	3	3	3
14		2	2	2	pc_4	4	4	4
15		2	2	2	pc_5	5	5	5

Such combined data array serves as a basic input for the next sub-module of this executive code section. Each combination of plasma-crystal point represents single ray transmission which in order to be detected cannot to be blocked by components of the

system as port liner, both ECRH shields and collimator (with selected shutter position). All the calculations are performed based on the numerical representations of diagnostic's components (created by the modules previously described) and the *'transmission'* of each beam/ray is determined independently. An example of such matrix data is presented in the Table 3.4 – the transmission of each ray through individual obstacles (*'Transmission checkout'*) is implemented as a Boolean value representing possible transfer of plasma radiation (*'True'* in the green cell) and indicating components that blocked the transmission (*'False'* in the red cells). Finally, it is assumed, that if any of those components blocked the incoming ray, the indicated plasma-crystal transmission is not investigated and removed from the analyzed dataset.

Table 3.4. Schematic of the data array showing photon transmission between all plasma points and crystals points. Green cells represent photons whose transmission was not blocked by any obstacle (collimator, ECRH shield etc.) while red cells ("False") represent blocked photons.

PLASMA COORD	CRYSTAL COORD	TRANSMISSION CHECKOUT (BOOL)				DISTANCE [mm]	ANGLE [°]
idx	idx	Port Liner	ECRH_shield_1	ECRH_shield_2	collimator	plasma_crys	plasma_crys
pp_1	pc_1	True	True	False	False	-	-
	pc_2	True	True	True	False	-	-
	pc_3	True	True	False	False	-	-
	pc_4	False	False	False	False	-	-
	pc_5	True	True	True	True	x_5	$\alpha = angle_5$
pp_2	pc_1	True	False	False	False	-	-
	pc_2	True	True	False	False	-	-
	pc_3	True	True	True	False	-	-
	pc_4	True	True	True	True	x_9	$\alpha = angle_9$
	pc_5	True	True	True	True	x_{10}	$\alpha = angle_{10}$
pp_3	pc_1	True	True	True	False	-	-
	pc_2	True	True	False	False	-	-
	pc_3	True	False	False	False	-	-
	pc_4	True	True	True	True	x_{14}	$\alpha = angle_{14}$
	pc_5	True	True	True	True	x_{15}	$\alpha = angle_{15}$

After determination of the set of plasma volumes (plasma coordinates), which are *'visible'* and in unblocked way associated with set of defined fragments of crystal's surface (crystal's coordinates), the distances between those points are calculated.

Since the dispersive elements are cylindrically curved and the reflectivity depends strongly on the AOI of the incoming light, for each of the corresponding indexes referring to the calculated distances the angle of incident on the crystal's surface ("*ANGLE*") is calculated. It is defined as angle between the incident beam and normal to the crystal's surface. Assuming photon emission of the plasma to be isotropic to the full solid angle (see Figure 3.5), the respective radiation fraction reaching individual points on the crystal's surface is calculated ($\frac{a}{4\pi R^2}$). This, strongly depends on the crystal's grid density, however, is automatically calculated and included in the formula calculating registered radiance flux.
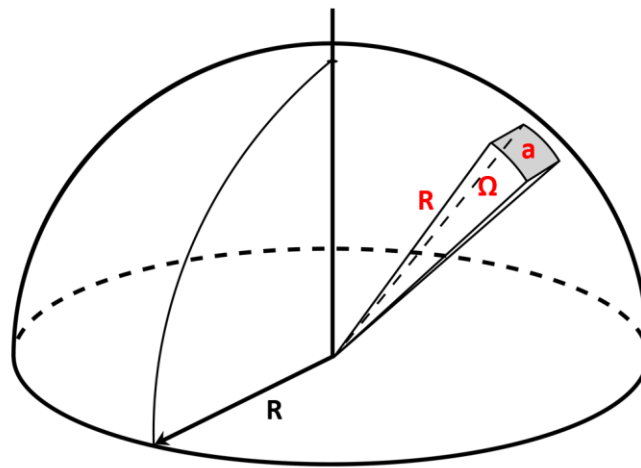
Figure 3.5. Isotropic radiation emission into a solid angle (Ω) passing through area (a).

Calculated information are then stored in one large data array including all 'visible' plasma points with a set of related parameters (described above). From this, the photon flux emitted by a given plasma region and hence reflected by respective crystal point is calculated. This operation is performed simply by multiplication of radiation fraction ('*fraction*') and reflectivity of the crystal ('*calc_reflect*') what is presented in the Table 3.5 as the '*intensity_fraction*' column.

Table 3.5. Data array containing set of calculated parameters required for emissivity calculation.

idx	plasma_x [mm]	plasma_y [mm]	plasma_z [mm]	DIST [mm]	ANGLE [º]	fraction [%]	calc_reflect [%]	intensity_fraction [%]
pp_1	0	0	0	a5	α = 5	f5	r5	f5 · r5 = int5
pp_2	1	1	1	a9	α = 9	f9	r9	f9 · r9 = int9
pp_2	1	1	1	a10	α = 10	f10	r10	f10 · r10 = int10
pp_3	2	2	2	a14	α = 14	f14	r14	f14 · r14 = int14
pp_3	2	2	2	a15	α = 15	f15	f15	f15 · r15 = int15

Nevertheless, such large dataset when assuming point cloud represented by e.g., 15,000 points and high-level discreet crystals surface grid with, e.g., 16,000 (200 x 80) points, results in a combination of up to 240 million of rows (assuming 100% transmission through collimator and other mechanical obstacles). Such large dataset is no longer handy in operation and consumes huge amount of memory (approximately 25 GB) and time required for its processing. Therefore, for a high precision computation, an intermediate step of a dataset compression was implemented (see Table 3.6).

Table 3.6. Compressed dataset containing coordinates within the observable plasma vicinity with intensity fraction emitted.

Idx	plasma_x [mm]	plasma_y [mm]	plasma_z [mm]	total_intensity_fraction [%]
pp_1	0	0	0	int5
pp_2	1	1	1	int9 + int10
pp_3	2	2	2	int14 + int15

This final dataset contains only plasma coordinates with their initially assigned indexes and the total intensity fraction emitted by the selected plasma point. The column '*total_intensity_fraction*' represents the sum of the radiation emitted by the selected plasma point and reflected by dispersive element, integrated along the crystal surface into one value. The presented solution allows to significantly reduce the memory requirement (down to dozens of MB) what is extremely valuable from the point of view of regular working station with limited computing resources. On the other hand, some information are irretrievably lost and cannot be recovered until the next computing session. For that reason the possible calculations requiring those data need

to be performed separately. Finally – since the described code simulates the emissivity of the selected Lyman-α line transitions only – it is important to emphasize, that the continuum radiation modelling is currently not included. The calculated points clouds representing registered plasma regions of all considered ions is presented in Figure 3.6.
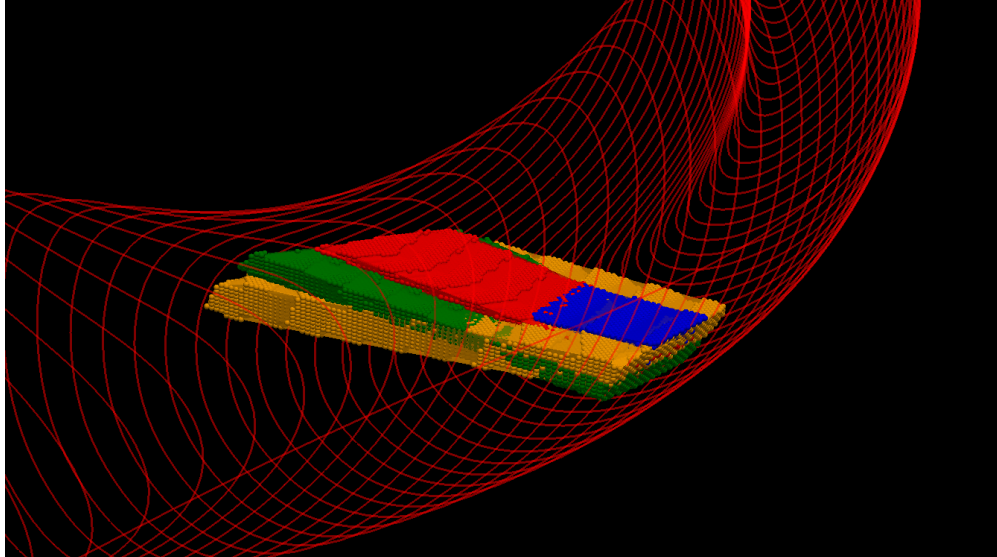
Figure 3.6. Graphical representation of the observed plasma volumes of all investigated ions: red color represents the plasma volume observed by the B channel, blue by channel C, green refers to the N channel and O is represented by orange.

To process all the above-described operations with relatively high precision, a significant computing power as well as of available RAM memory is required. Since Python programming language nominally works using 1 thread – the dedicated tool supporting multiprocessing and distributed computing needed to be applied. A tool that meets these requirements is DASK [68] – the convenient framework ensuring parallel computations using available CPU potential.

3.1.5 r_{eff} calculation

In order to compare parameters from different regions of the W7-X plasmas, it is necessary to standardize the position of selected points in reference to the stellarator's magnetic axis. For this reason, the poloidally varying shapes of the stellarator's poloidal cross sections are normalized to the circular poloidal cross sections (Figure 3.7), thus providing a way to compare results from different diagnostics systems at different locations.
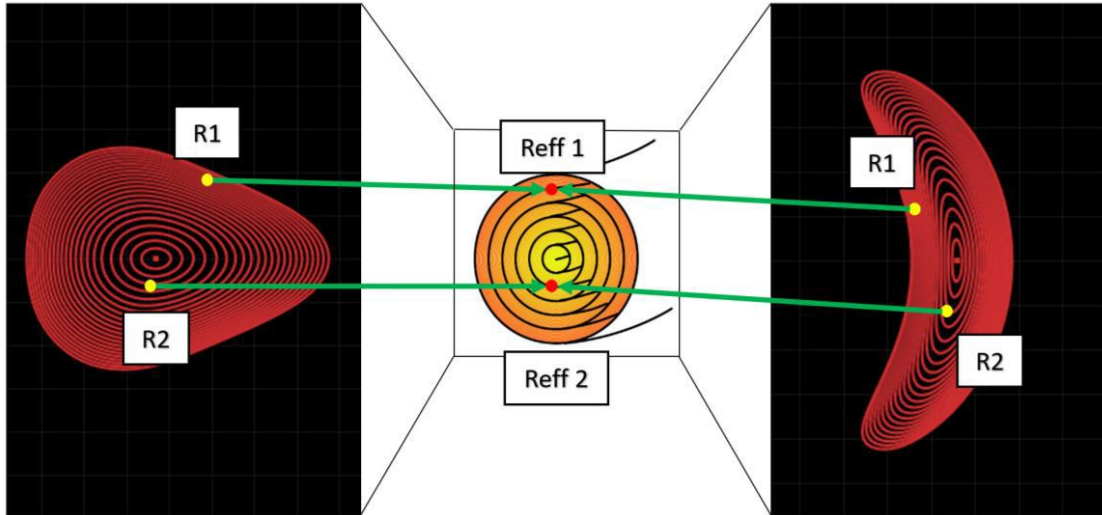
Figure 3.7. Normalization of the stellarator's poloidal cross-section to the circular cross-section.

The matrix of observed plasma coordinates (obtained by solving system's geometry – see Table 3.6), serves as an input for the effective radius calculations. In order to proceed, the VMEC (Variational Moments Equilibrium Code) which is dedicated tool to solve the magnetohydrodynamics (MHD) force balance equations in a three dimensional space was used [69]. This code became a standard code for solving 3D equilibria in computing the MHD problems. Therefore the specific magnetic field configuration needs to be chosen for which the r_{eff} values of the observed plasma volume will be determined. The final output data array containing plasma coordinates with corresponding r_{eff} values and emitted radiation fraction is presented in the Table 3.7.

Table 3.7. Final data array containing all the information required to calculate the line emissivity.

idx	plasma_x [mm]	plasma_y [mm]	plasma_z [mm]	Reff [m]	total_intensity_fraction [%]
pp_1	0	0	0	'NaN'	int5
pp_2	1	1	1	r_{eff1}	int9 + int10
pp_3	2	2	2	r_{eff2}	int14 + int15

If the given point is outside the LCFS – the '*NaN*' ('*not a number*') value is returned and consequently removed from the dataset. Therefore only the points positioned within the plasma region are considered.

3.2 Emissivity calculation

The last module is developed for calculation of emissivity radiated by all the considered plasma points and, finally, a fully volume integrated emissivity for the respective energy channel. For that reason, the essential input such as plasma electron temperature and density profiles, fractional abundances of respective ions as well as PECs (Photo Emissivity Coefficients) are required. Below, the methodology of data processing as well as specific parameter calculation is described.

3.2.1 Temperature and density profiles

In order to represent different kinetic profiles one may use raw experimental data from the W7-X database and apply them as input for further calculations. Such profiles, however, usually can be easily approximated by a simple analytical function – a sum of two Gaussians (24):

$$T_e, n_e(r_{eff}) = A_1 \cdot exp\left(-\frac{r_{eff}^2}{2 \cdot w_1^2}\right) + A_2 \cdot exp\left(-\frac{(r_{eff} - x_2)^2}{2 \cdot w_2^2}\right) \qquad (24)$$

Parameters for the exemplary temperature and density profiles calculations (fitted to the profiles from discharge *20181011_012* – see also Figure 4.4) are listed in the Table 3.8:

Table 3.8. Parameters used to determine approximate temperature and density profiles.

Approx. Function parameters	A_1	w_1	x_1	A_2	w_2	x_2	A_1/A_2 ratio
Electron temperature $[keV]$	1.87	0.155	0	0.21	0.07	0.38	8.9
Electron density $[\boldsymbol{m^{-3}}]$	$7.0 \cdot 10^{19}$	0.37	0	$9.8 \cdot 10^{18}$	0.11	0.5	7.1

where $A_{1,2}$ – maximum of a Gaussian distribution, $w_{1,2}$ – width, $x_{1,2}$ – cener position and A_1/A_2 – ratio of Gaussian distributions.

To investigate intensity changes as a function of different kinetic plasma parameters (n_e, T_e), this module provides easy and quick procedure for profiles calculations which serves as input for the emissivity calculations.

3.2.2 Fractional abundance

Since the impurity transport in the MCF plasmas is always presented, the corona equilibrium cannot be considered as a basic theoretical model for stellarators. Due to that fact, it is necessary to implement approach based on the impurity transport occurring in the W7-X plasmas. For this purpose, the pySTRAHL code [7] was used to calculate the fractional abundances of respective ionization states of considered elements.

Using an information about the electron temperature distribution in the plasma, the respective fractional abundance (FA) values for the specific H-like ions based on the coronal balance model were calculated. Figure 3.8 presents example of fractional abundances of carbon assuming corona equilibrium (left) and including impurity transport (right).
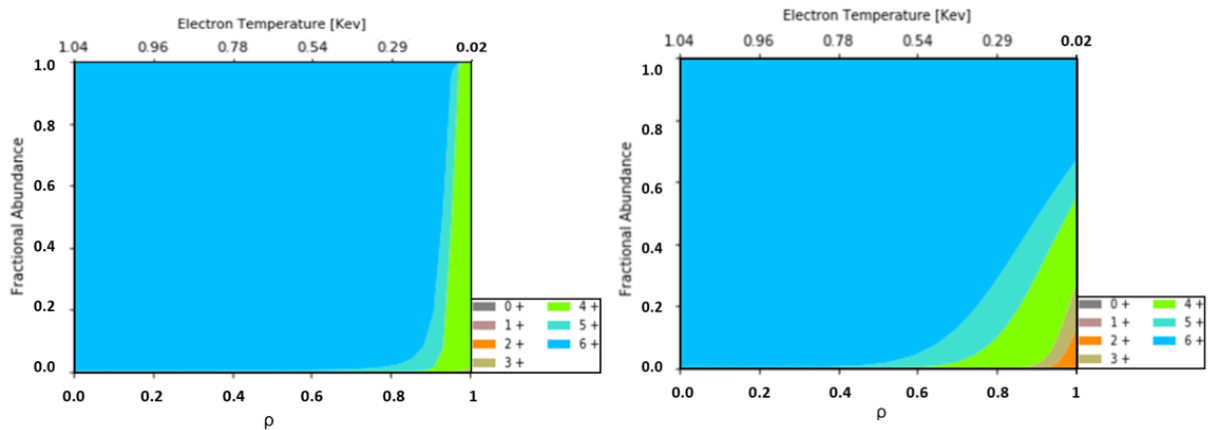
Figure 3.8. Fractional abundance of different ionization states of carbon lines as a function of electron temperature assuming corona equilibrium (left) and including impurity transport (right) [70]*.*

3.2.3 Photon emissivity coefficients

The last part required for the calculation is application of Photon Emissivity Coefficients (PEC) provided by the ADAS database [42]. Based on the information

about the local temperature it is possible to calculate the PEC values both for excitation and recombination radiation.

Since the structure of PEC files is rather complex, the data is stored as a n_e - T_e nodes (with fairly poor 'resolution'). Therefore, it was essential to develop fully automated way of its readout and interpolation. Since the data is represented as a three dimensional matrix (n_e - T_e - PEC), the step by step 2D (n_e - PEC and T_e − PEC) interpolation was implemented. The interpolation step may be specified by user, however, it is nominally set-up for the highest optimal precision/calculation time.

Each PEC value corresponds to the respective plasma region (determined by a given kinetic parameters) and needs to be calculated for all plasma points. An array of designated plasma coordinates and corresponding r_{eff}, n_e, T_e, PEC and FA values serves as an input for emissivity calculation assuming corona model.

3.2.4 Impurity profiles shapes and CXRS system

Last but not least, in order to calculate the total radiated emissivity it is crucial to determine the radial impurity distribution along the minor radius (r_{eff}) of the plasma. In the presented numerical code the linear impurity distribution is set by default. Nevertheless, during former experiments in MCF plasmas it was proved, that under specific conditions some impurity fraction becomes accumulated in a specific plasma region leading to their non-linear radial distribution (this process was already explained in section 1.6). To accommodate this, the code provides a way to use their different shapes. These are derived from the Charge Exchange Recombination System (CXRS) which was set up at W7-X as an active spectroscopy diagnostic. The principle of its operation is based on the NBI [34] heating system as the neutrals injected by this system state as a neutral source for the charge exchange processes. The CXRS diagnostic provides spatially resolved information about the impurity content in the plasma. This is obtained from the intersection of NBI beam line and CXRS line-of-sight and derives spatially resolved information about the profiles of the intrinsic fully stripped low-Z impurity densities (n_Z) and ion temperature (T_i). It provides also radial electric field measurements (E_r) and toroidal flow velocity profiles from the edge to the plasma core. The active beam spectroscopy is the only system at W7-X providing

information about the low-Z impurity distribution in the central plasma region. The detailed characteristic of this system is presented in [71].

The radial impurity shapes are of great importance since the total emitted radiation from plasma depends strongly on their radial position in the confined plasma region. This impact is presented in more details in the further section (3.2.5). Moreover, these data can also be applied for the C/O monitor system's calibration.

3.2.5 Average impurity density calculation

Since the W7-X plasma is in the cylindrical shape (after normalization to r_{eff}), the radial impurity distribution will play a significant role in the final photon intensities measured by the system. When comparing different plasma scenarios with an assumption of equal impurity content in the plasma, their average values had to be considered. Because the W7-X plasma is characterized by a non-regular shape, it is also nontrivial task and could generate some issues to reliably calculate average e.g., densities. However, its normalization to the cylindrical shape using VMEC code (r_{eff}) simplified this procedure leading to a straightforward volume integral over cylindrical shape. The method to calculate any average values in a considered plasma shape is presented below.

Considering N as a number of particles as concentration of particles (e.g., ions) and V as considered plasma volume in a cylindrical (normalized) shape:

$$n = \frac{N}{V} \qquad (25)$$

$$V = \pi \cdot h \cdot (r_{k+1}^2 - r_k^2) \qquad (26)$$

Mean

$$n_k = \frac{N_k}{V} = \frac{N_k}{\pi \cdot h \cdot (r_{k+1}^2 - r_k^2)} \qquad (27)$$

Hence

$$N_k = n_k \cdot \pi \cdot h \cdot (r_{k+1}^2 - r_k^2) \qquad (28)$$

and average n_{avg}

$$n_{avg} = \frac{N_{total}}{V_{total}} \qquad (29)$$

$$V_{total} = \pi \cdot h \cdot r_{max}^2 \qquad (30)$$

$$N_{total} = \sum_{k=0}^{m} N_k = \pi \cdot h \cdot \sum_{k=0}^{m} n_k \cdot (r_{k+1}^2 - r_k^2) \qquad (31)$$

Therefore

$$n_{avg} = \frac{\pi \cdot h \cdot \sum_{k=0}^{m} n_k \cdot (r_{k+1}^2 - r_k^2)}{\pi \cdot h \cdot r_{max}^2} = \frac{\sum_{k=0}^{m} n_k \cdot (r_{k+1}^2 - r_k^2)}{r_{max}^2} \qquad (32)$$

In order to simplify performed analyses (presented in further sections) and benchmark results of calculations under different plasma parameters (while not exceeding 2 - 3% of total impurity concentrations), the average impurity density in the plasma was assumed $n_z = 2 \cdot 10^{17} \ m^{-3}$.

3.2.6 Radiation intensity calculation

Finally, the emitted radiation is calculated. The corresponding spectral emission from a unit plasma volume ($\epsilon(r)$) can be obtained using the formula (33) [41]:

$$\epsilon(r) = PEC^X(r) \cdot n_e(r) \cdot n_Z(r) \cdot FA^X(r) \left[\frac{ph}{m^3 \cdot s}\right] \qquad (33)$$

where r is the minor plasma radius, $n_Z(r)$ and $n_e(r)$ $[m^{-3}]$ – impurity and electron densities, $PEC^X(r)$ $[ph \cdot m^3 \cdot s^{-1}]$ – Photon Emissivity Coefficient for a given spectral line (from ADAS database) and $FA^X(r)$ [a.u.] - fractional abundance of a given ion at a minor plasma radius r. Nominally the code assumes 'flat' impurity distributions along the r, however, there is also a possibility to implement profiles defined by a user e.g., with the peak on the axis of the plasma (in the latter sections called as 'peaked' profiles). To increase the reliability of the performed modelling, an absolutely calibrated radial impurity distributions (provided by the CXRS system) were used.

4 Study of the impact of kinetic and impurity profiles on the photon intensities measured by the use of the C/O monitor system

Experimental data measured by the C/O monitor system will not be easy for interpretation in real time. It will be associated with:

- integration of the signal from a large and unique geometry of observed plasma volume;
- monitoring only one spectral line per channel;
- impact of kinetic (T_e, n_e) parameters on emissivity profile;
- impact of impurity level as well as its radial distribution (as a consequence of impurity transport) on the obtained output signals.

Such conditions can make the measured data difficult to analyze, and thus to draw some reliable conclusions. Therefore it is crucial to thoroughly understand the impact of different plasma and geometrical parameters on the output intensities. In order to estimate the signal provided by the system, evaluate its capabilities and limitations, a complex numerical procedure was developed. Since the main goal of the system is to monitor the level of light impurities and their changes during the discharge, only the linear radiation will be calculated and line shapes (which result from other factors) will be neglected.

4.1 Description of the calculation procedure

To study the impact of the aforementioned factors on the output signals obtained by each energy channel, number of simulations were performed. To achieve this goal the pySTRAHL and the recently developed C/O monitor codes were used. The entire procedure is divided into two major procedures:

a)   **pySTRAHL code:**
- calculation of the radial ionic distributions along the minor radius. Required inputs are:

- o kinetic (n_e, T_e) profiles,
- o diffusion (D) and convection velocity (V) profiles;
- calculation of fractional abundances of considered impurity (see Figure 4.1):
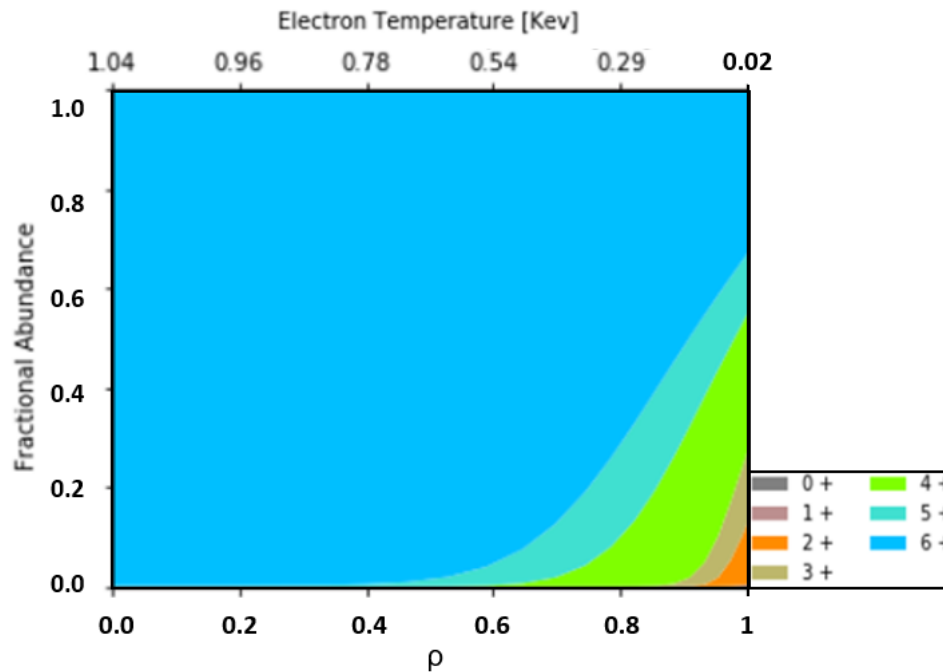
Figure 4.1 Example of ionic distribution of C along the plasma minor radius calculated using pySTRAHL [70].

- calculation of the total impurity density profile being a sum of its all ions.

b) C/O monitor code procedure:
- calculation of r_{eff} assuming standard magnetic field configuration by the use of VMEC code (via the dedicated API);
- solving the system's geometry (by performing ray tracing operation) and assignment of r_{eff} values to the corresponding point of a meshed plasma volume observed by each energy channel;
- calculation of the fraction of the emitted radiation reaching the respective detectors;
- assignment of kinetic parameters and impurity concentrations values to the considered elementary plasma volume at a given r_{eff} location;

- such dataset (kinetic profiles, FA) together with PECs from ADAS database serve as input for the radial emissivity calculations of each ion from a plasma based on equation (33). As a result the radial photon emissivity [$ph \cdot m^{-3} \cdot s^{-1}$] as a function of r_{eff} is determined:
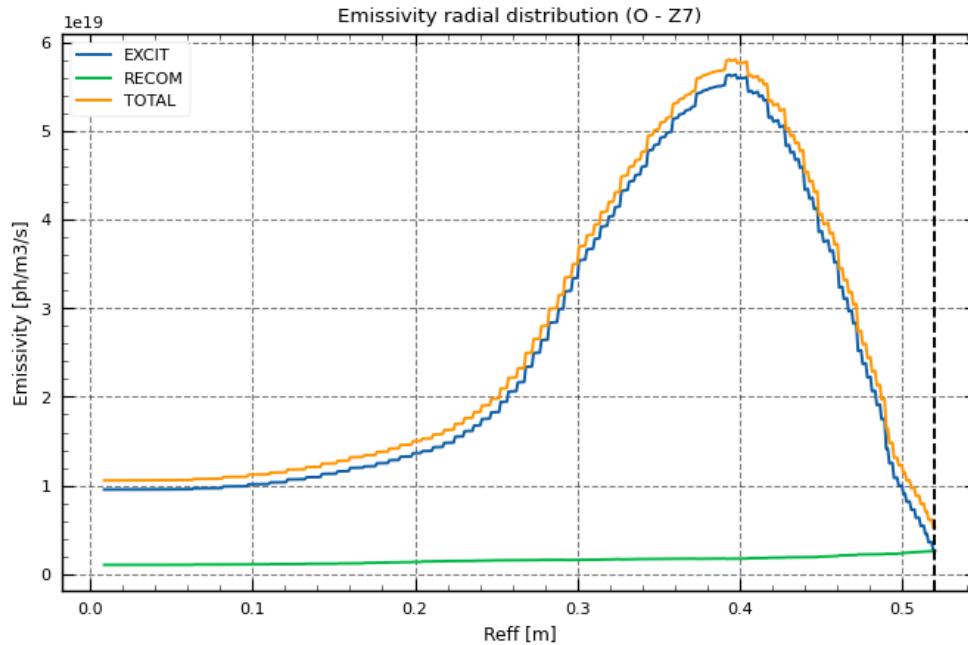
Figure 4.2 An example of calculated radial emissivity distribution of O^{7+} as a function of R_{eff} [m]. LCFS is located at R_{eff} = 0.53 m.

- peraparation of the inputs for the calculation of the total radiation flux on the detectors based on the radial emissivity distribution and the system's geometry (defining the volumes and corresponding solid angles 'seen' by each of detectors). Thus, a map of 'total_intensity_fractions' is built;
- calculation of the total radiation flux by a numerical integration of all 'total_intensity_fractions' points representing elementary plasma volume defined by their spatial coordinates, r_{eff}, kinetic parameters (n_e, T_e) and impurity density (n_z). This approach is equivalent to the volume integral over the radial emissivity distribution (in carthesian coordinate system).

All calculations were carried out in the confined plasma region, from the axis up to the last closed flux surface - $0 \leq \rho \leq 1$. The ρ is a radial coordinate defined as 0 at the magnetic axis and 1 at the LCFS as an alternative average radius. For plasma located at $\rho > 1$ the model cannot perform reliable calculations.

The main purpose of this work was to get qualitative rather than quantitative information about the volume-integrated signals and to prove, that the system will be reliable for the measurements it was designed for. Therefore in order to investigate impact of different parameters on the C/O monitor signals, two major studies were performed, namely:

- Study of T_e, n_e and impurity profiles impact on the C/O monitor system' signals;
- Case study of radiated photon intensities with respect to the system's efficiency – simulation approach.

The description of the aforementioned analyses is in the scope of sections 4.2 and 4.3 respectively.

4.2 Study of kinetic and impurity profiles impact on the C/O monitor system' signals

The first analysis examines impact of kinetic profiles (T_e, n_e) and radial impurity distributions on the output photon flux intensities. Here, two different impurity profile distributions were considered (so called 'flat' and 'peaked' – explained in the next paragraph). Their shapes reflect different impurity transport regimes (anomalous and neoclassical, respectively) that were observed at the W7-X. However, it needs to be stressed, that within this work the impurity transport itself is not investigated, but rather its impact on the obtained photon intensities. Therefore, it is important to investigate how sensitive on that phenomenon the system will be. Secondly, it is worth to check if the diagnostic could serve as a straightforward tool providing fast, high-quality information about the impurity content in the plasma. Positive verification of the issue motivates application of C/O monitor as a reliable diagnostic system during the W7-X operation.

For all the considered examples the average impurity density was established at $2 \cdot 10^{17} m^{-3}$. The magnetic field configuration used in these considerations is standard magnetic configuration [72]. In the analysis, two radial impurity distribution profiles were considered, assuming their equal average content in a plasma. The impurity profile labeled as 'flat' represents uniform distribution of impurities along the minor radius of the plasma (Figure 4.3 – area under orange line). This is the basic example,

commonly observed at the W7-X plasmas. However, in some specific conditions, when neoclassical impurity transport becomes dominant, the enhanced impurity confinement in a plasma may be observed. In this work radial impurity profile shape is considered as a 'peaked' profile (Figure 4.3 – area under blue line). This may occur under some specific plasma conditions (such as high electron density, negative radial electric field (ion root confinement – IRC)). It was also noticed that the impurity accumulation was more likely to be observed during NBI heating or strong pellet fueling (with frozen hydrogen) in the core [73].
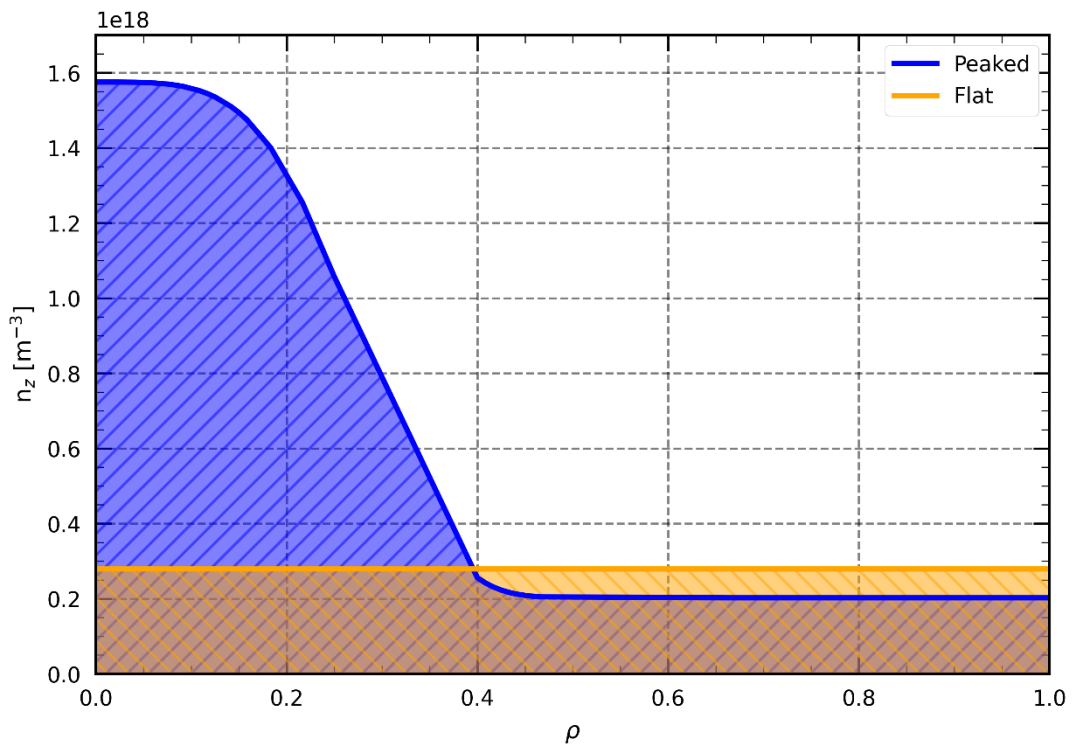
Figure 4.3. Example of 'peaked' (blue area) and 'flat' (orange) radial impurity distributions in the observed plasma volume assuming their equal average densities.

This analysis was performed using the set of various range of T_e and n_e parameters. The basis for kinetic profiles determination were two experimental results measured during the OP1.2b: first discharge *20181011_012* characterized by high value of on-axis electron density ($7 \cdot 10^{19}$ m^{-3}) and low central electron temperature (1.87 keV) while the second discharge *20180816_022* was characterized by low central electron density ($n_e = 2 \cdot 10^{19}$ m^{-3}) and high central electron temperature ($T_e = 8$ keV) – see Figure 4.4.
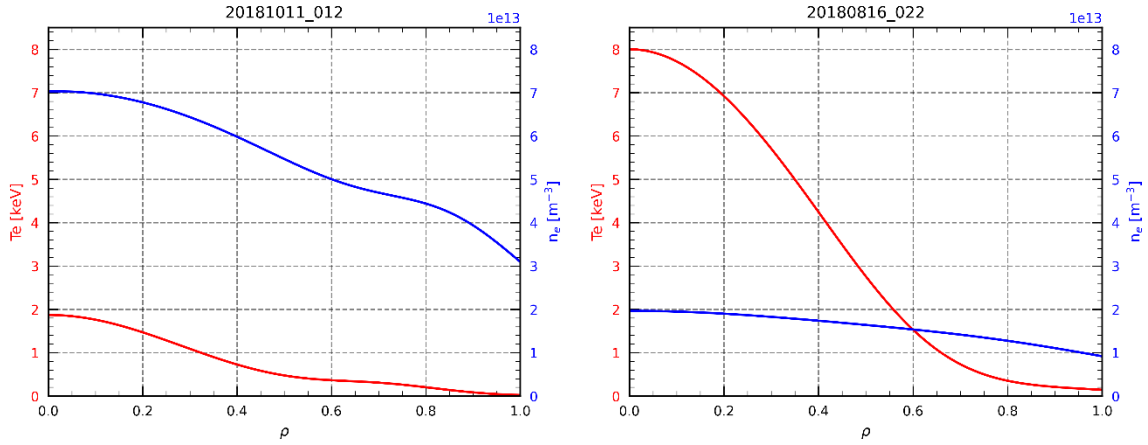
Figure 4.4. Examples of experimentally measured plasma kinetic profiles for low T_e – high n_e case (20181011_012 – left) and high T_e – low n_e case (20180816_022 – right). T_e profiles are indicated with red color and n_e with blue.

The interpolation between the respective density and temperature profiles was performed using analytical method based on the sum of two Gaussian profiles that was already described using equation (24). The interpolation step for T_e profiles was set to 1 keV and 10^{19} m^{-3} for n_e profiles.

However, since the strongest line emissions of considered Lyman-α transitions are observed in the low temperature ranges, the interpolation interval for low T_e (1 – 2.5 keV) was assumed to be more 'dense' in this range. Finally, the set of 14 T_e and 10 n_e profiles was determined and used in further analysis (see Figure 4.5).
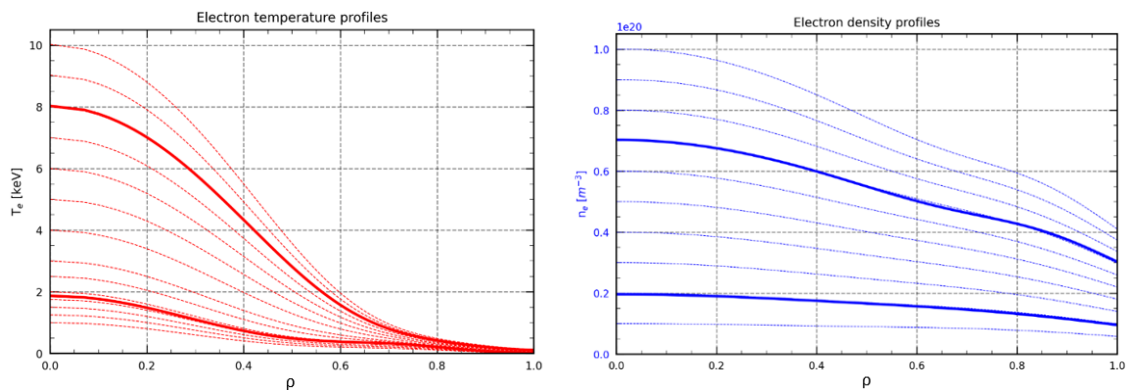
Figure 4.5. Interpolated set of T_e (red - left) and n_e (blue - right) profiles used for the analysis. Dashed lines represent calculated profiles while solid lines represent experimentally measured profiles introduced in the Figure 4.4.

The presented analysis is divided into four parts, each focused on understanding of impact of kinetic parameters on the emitted photon fluxes (related to different elements). Furthermore, two radial impurity distributions - 'flat' and 'peaked' - were also taken into considerations. These combinations of plasma conditions (presented in Table 4.1) were thoroughly investigated and are described in the next sections.

Table 4.1. Summary of considered plasma scenarios depending on kinetic parameters and impurity profiles shapes.

Impurity profile/ kinetic profile	**'Flat'**	**'Peaked'**
Electron density	a) **'Flat'** impurity profile – density dependence	c) **'Peaked'** impurity profile – density dependence
Electron temperature	b) **'Flat'** impurity profile – temperature dependence	d) **'Peaked'** impurity profile – temperature dependence

4.2.1 Photon intensity dependencies for 'flat' impurity profiles

4.2.1.1 Dependence of the electron density

First, the photon intensities for different energy channels (B, C, N and O), as a dependence of electron density, was considered. Each point in Figure 4.6 represents the radiated photon flux intensity being a result of volume-integrated emissivity radiated towards the detectors, while the solid line represents their interpolation.

Mapping of all n_e profiles assuming low T_e case (central T_e = 1 keV) shows that the increase of electron density is positively correlated with the photon intensities. The dependence is almost linear, however, for the heaviest element - oxygen, the intensity increases approximately 4 times whereas for the lightest element (boron) it doubles. It can also be noticed that the total intensity associated with nitrogen line is the lowest, even though this spectral line is emitted in the broader range of electron temperatures (above 600 eV) compared to the B and C lines. The reason is the reflectivity of the MLM applied for this channel, which is very poor. Its reflectivity (declared by the manufacturer) is approx. 2 – 3 times lower compared to the MLMs applied for B and C energy channels.
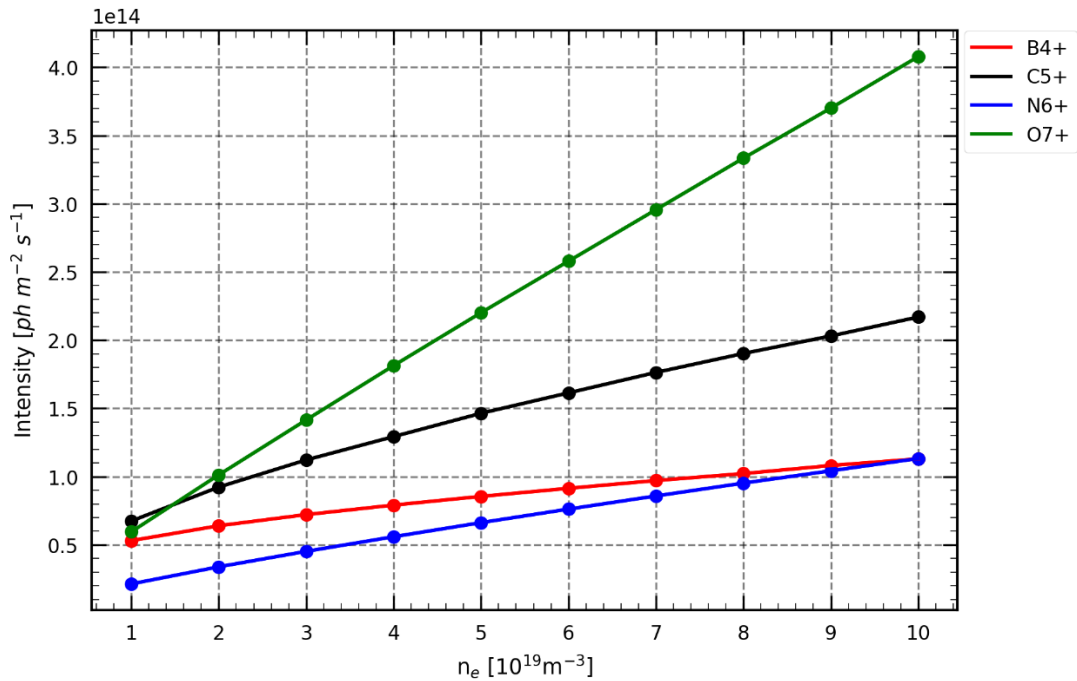
Figure 4.6. Spline fit of radiated photon intensities of selected ions as a function of electron density assuming the maximum electron temperature at $T_e = 1\,keV$ and 'flat' impurity profile. Each point represents ONLY a fraction of the radiation reaching the surface representing the respective detector.

To illustrate gradients of this dependence as a function of electron densities, the radiation intensities were normalized to their maxima. As the atomic number increases (B_5 -> C_6-> N_7 -> O_8), so does the gradient of the photon flux intensities as a function of n_e (see Figure 4.7). The strongest impact of electron density is observed sequentially for O and N lines ($\approx$5× increase of a photon intensity in the given n_e range) and the weakest for B line ($\approx$2×). This example shows, that for plasma with low central T_e, the impact of electron density increases with the Z number.
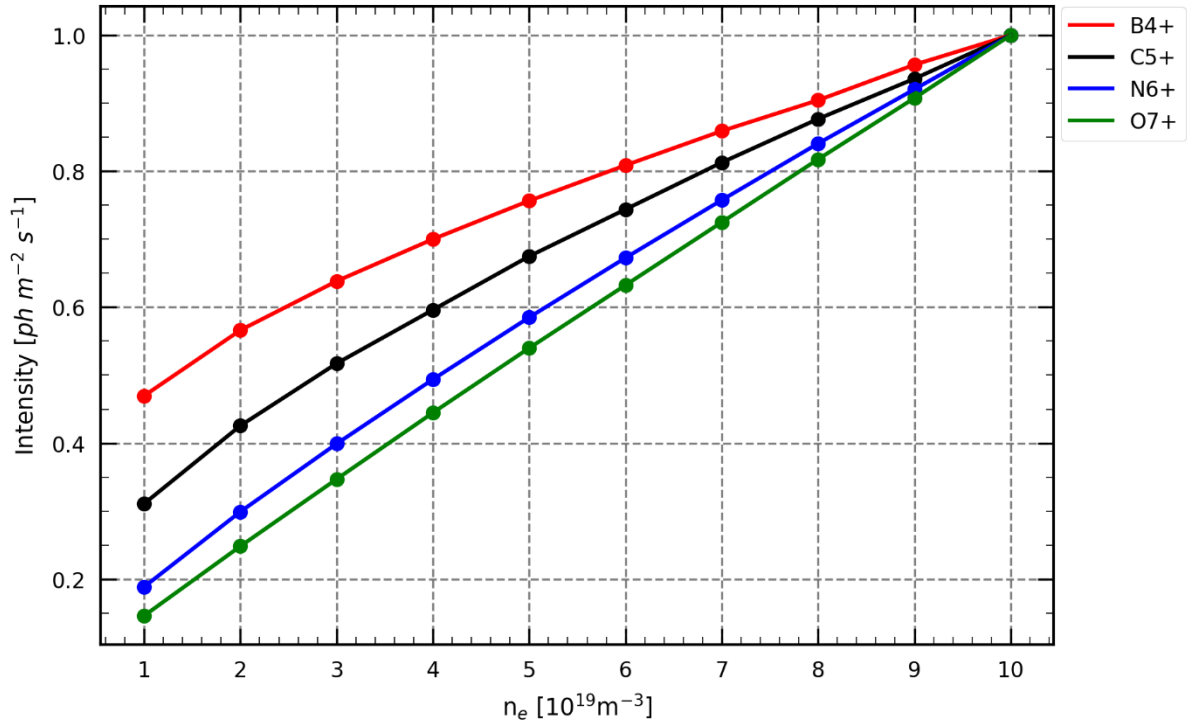
Figure 4.7. Spline fit of radiated photon intensities (normalized to 1) of selected ions as a function of electron density assuming the maximum electron temperature at $T_e = 1\ keV$ and 'flat' impurity profile.

In Figure 4.8 the radial emissivity distributions of all considered Lyman-α transitions as a function of n_e are presented in a form of colormap. X axis represents the increase of electron density n_e from 10^{19} m^{-3} to 10^{20} m^{-3} while Y axis represents the radial emissivity distribution along the radius $0 < \rho < 1$. Color scale is associated with emissivity intensity along the minor radius of the plasma. Analysis of obtained results assuming fixed low T_e profile (1 keV on-axis), clearly shows that total radial emissions of all elements are located within the plasma region $\rho < 1$. The heavier element, the broader emissivity area in the plasma and the closer its maximum emission to the central plasma region. For 'flat' impurity profile the emissivity is mainly distributed in the area closer the plasma edge ($\rho > 0.4$). For the higher electron densities some noticeable part/component of radiation of O Lyman-α transition is observed close to the plasma core.
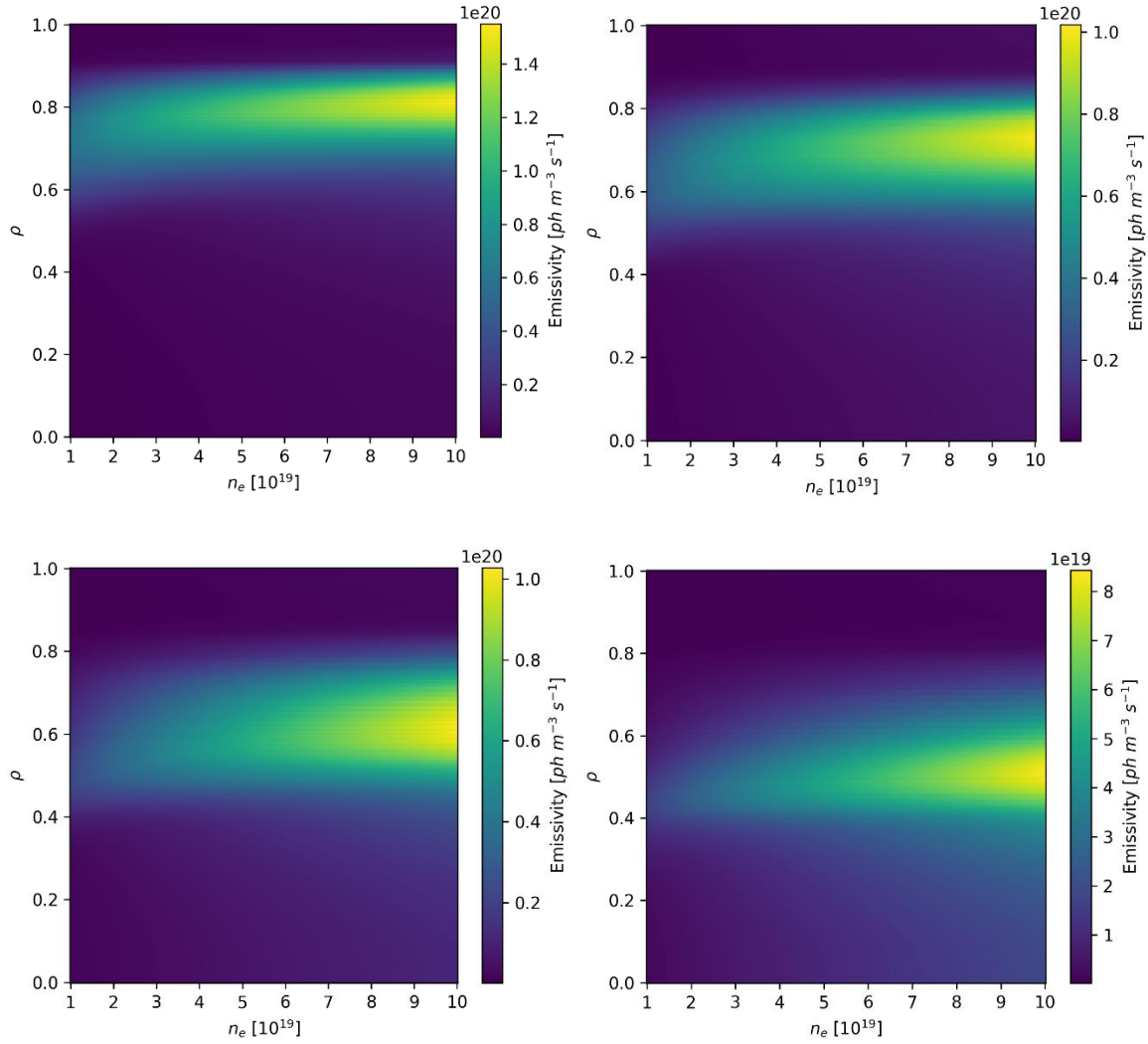
*Figure 4.8. Colormap representing radial emissivity distributions of all considered ions (from top left B^{4+}, C^{5+}, N^{6+}, O^{7+}) as a function of electron density assuming the maximum electron temperature at $T_e = 1\ keV$ and '**flat**' impurity profile.*

When considering radiation intensity changes as a function of n_e at high central T_e and 'flat' impurity profile it can be noticed, that these trends are similar to those observed for the low T_e case (see Figure 4.9). For oxygen and nitrogen lines, trends are very similar to the low central T_e case especially for $n_e > 4 \cdot 10^{19}$ m^{-3}. For C line the intensity remains almost unchanged above $n_e > 5 \cdot 10^{19}$ m^{-3}. However, one may notice that for boron line consequently decreases over the entire n_e range. Again, the line intensity for nitrogen is the lowest of all elements for the same reason as explained before.
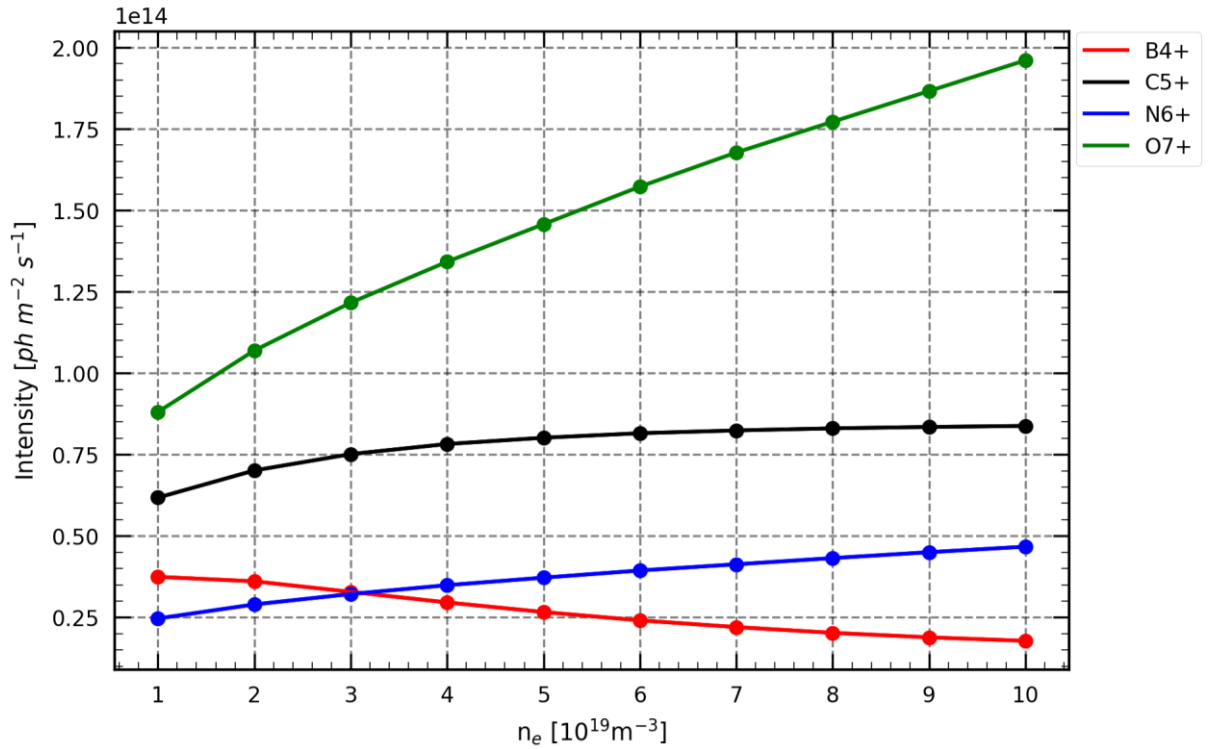
Figure 4.9. Spline fit of radiated photon intensities of selected ions as a function of electron density assuming the maximum electron temperature at $T_e = 10\ keV$ and 'flat' impurity profile. Each point represents ONLY a fraction of the radiation reaching the surface representing the respective detector.

Figure 4.10 presents the normalized radiated photon flux intensities of all ions and illustrates their gradient as a function of electron density. Although an increase of n_e in general leads to the photon flux intensity increase, here the B line signal drops by approximately 50%. Also, with increase of n_e the intensity gradient of C line is continuously reduced. Above $n_e > 6 - 7 \cdot 10^{19}\ m^{-3}$ the increase of the total photon intensity does not exceed 4%. These results indicate that plasma behaves differently than for low T_e case.
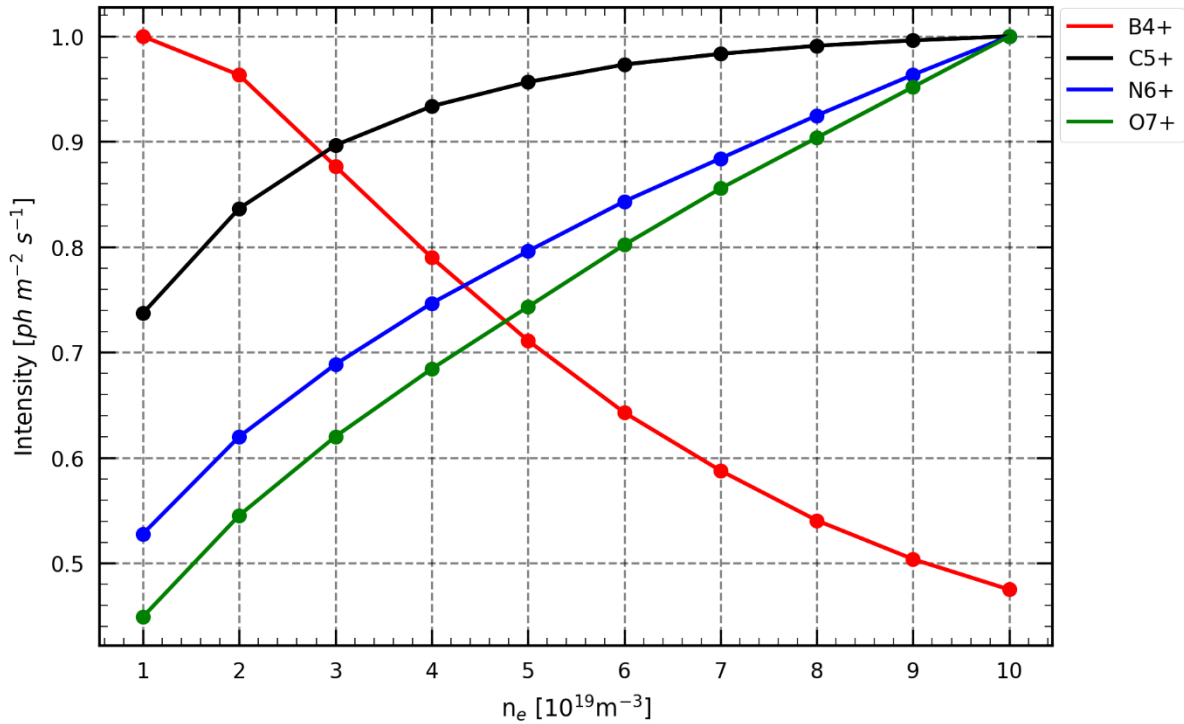
Figure 4.10. Spline fit of radiated photon intensities (normalized to 1) of selected ions as a function of electron density assuming the maximum electron temperature at $T_e = 10$ keV and 'flat' impurity profile.

The reason for such a behavior of the B line intensities is, that most of the B Lyman-α line radiation is partially emitted from the central plasma entering into the scrape-off layer region (SOL) which is not taken into account in the simulations – see Figure 4.11. Due to lack of the normalized r_{eff} data above the LCFS (represented by ρ = 1), it is very difficult to provide reliable information about radiation emitted from this region.

Similar behavior may be observed when analyzing C emissivity. Above $T_e \approx 3$ keV the signal 'loss' caused by the shift of its radial emissivity outside the LCFS leads to a situation when the increase of emitted radiation along the minor radius is 'negatively compensated' by the amount of 'missing radiation' outside LCFS. Therefore one has to be careful when drawing conclusions from examining these regions on the basis of a simulated approach. This is a well-known issue which is planned to be solved in the future (e.g., by the use of numerical codes dedicated to the SOL modelling). Of importance to our consideration here is the fact that the plasma conditions with simultaneously high n_e and T_e values, in which this behavior can be observed (especially for the B and C Lyman-α emissions), are rather specific and hence difficult to maintain in the W7-X case. Nevertheless, since the B and N related channels are not

going to be commissioned during the forthcoming experimental campaign OP2.0 - it is planned to work on that issue in the near future.
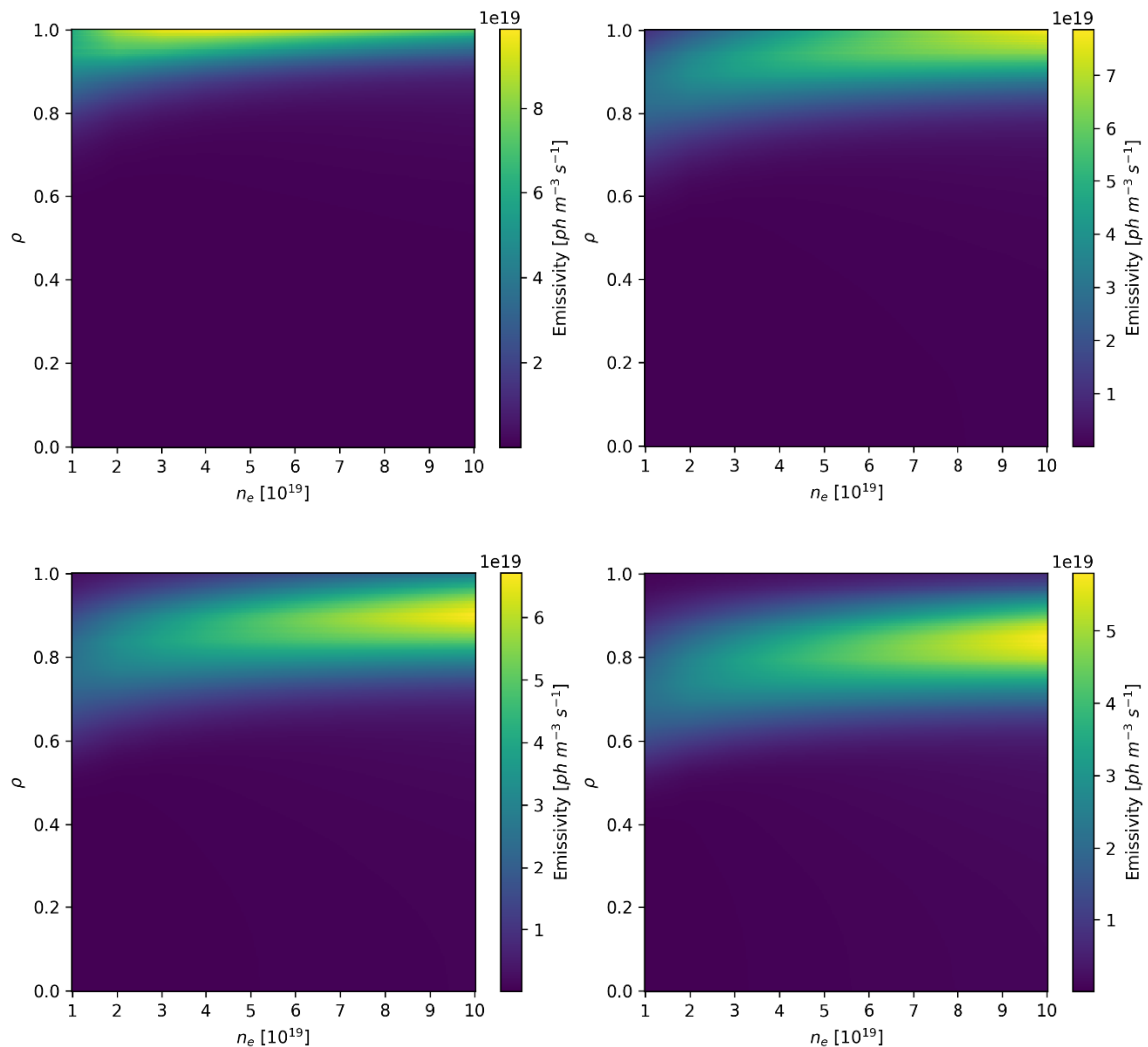
Figure 4.11. Colormap representing radial emissivity distributions of all considered ions (from top left B^{4+}, C^{5+}, N^{6+}, O^{7+}) as a function of electron density assuming the maximum electron temperature at $\boldsymbol{T_e = 10}$ $\boldsymbol{keV}$ and $\boldsymbol{'flat'}$ impurity profile.

4.2.1.2   Dependence on the electron temperature

The goal of this analysis was to examine the dependencies of the spectral lines' intensities with change of the T_e profile assuming low ($10^{19}\,m^{-3}$) and high ($10^{20}\,m^{-3}$) n_e central values (see Figure 4.12). In the first case, the low n_e was taken under consideration. At such low electron temperatures one may notice that each element behaves quite differently. A closer look on the investigated trends of O and N lines shows, that with the increase of T_e between 1 - 2 keV range, the signal increases so

that after reaching its local maximum at 2 keV, it begins to drop until 6 keV, which is followed again by a very slight rise of the signal. The C line reaches its maximum intensity at a lower temperature (approx. 1.25 keV). This is understandable since the electron temperature required for the excitation of C^{5+} ion is lower than in the case of N and O lines. After hitting the local 'bottom' (at approx. 4 - 5 keV) of the radiation intensity profile dependence on T_e, the intensity trend begins to slightly increase again.
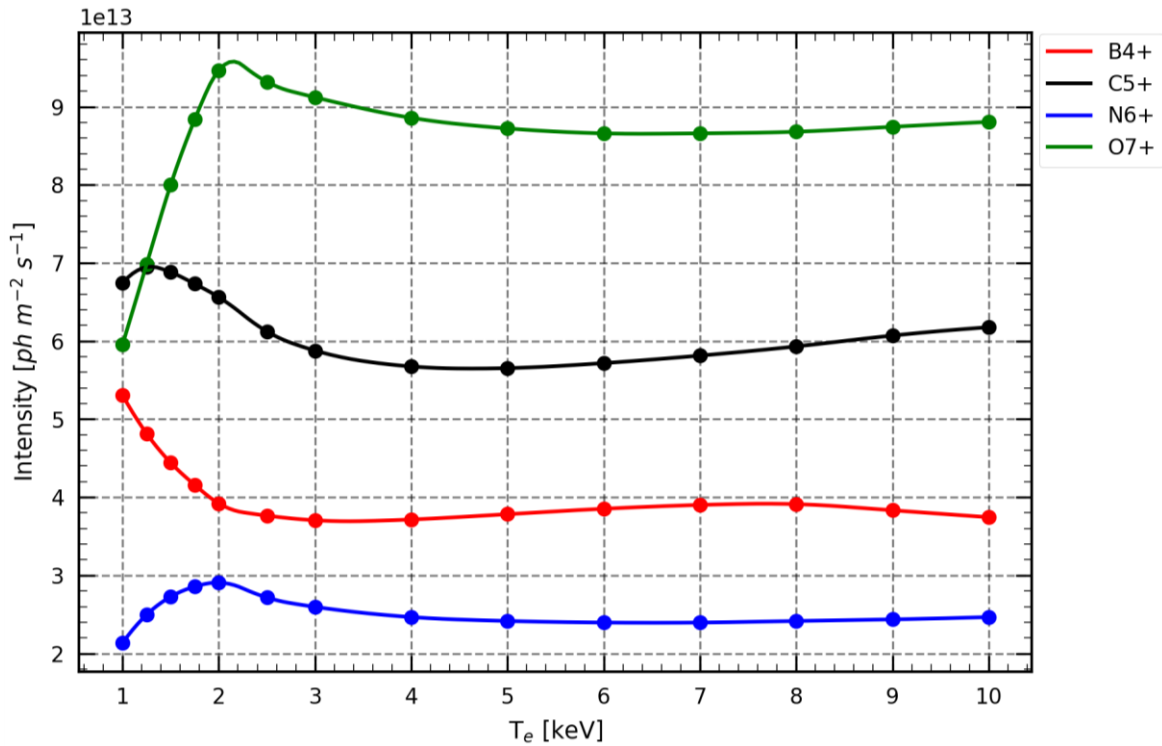
Figure 4.12. Spline fit of radiated photon intensities of selected ions as a function of electron temperature assuming the maximum electron density at $n_e = 10^{19}\,m^{-3}$ and 'flat' impurity profile. Each point represents ONLY a fraction of the radiation reaching the surface representing the respective detector.

Relative changes of normalized elemental line intensities are shown in Figure 4.13 (max. value normalization). For N and O lines the strongest signal' increase is observed in the range between 1 - 2 keV and equals approx. 30% and 50% respectively. The temperature range between 1 – 2.5 keV is characterized by a stronger signal volatility being a consequence of a high system sensitivity on the electron temperature. This is associated with the highest emission of considered lines in the specific electron temperatures increasing with the element's atomic number. Therefore the O Lyman-α line can be observed also in the plasma center while the B Lyman-α line can be seen

almost exclusively at the plasma edge where the electron temperatures are the lowest and does not fully ionize the atom.

After reaching the maximum intensity by C line at 1.25 keV, it begins to drop and reaches its local minimum at a T_e range 4 – 5 keV, which is lower by almost 20%. A similar behavior can be noticed for N and O lines, the maximum intensities of which are observed at 2 keV being followed by a signal drop at a range 6 - 7 keV. These intensity levels are lower by almost 20% and 10% for N and O respectively compared with their maxima. For all these elements hitting the local minima is followed by a re-rise of a signal until 10 keV. Slightly different behavior was observed for B. Since its line intensity over the considered temperature range decreases from the very beginning, its maximum would be observed below T_e < 1 keV. The initial intensity drop equals approx. 30% until it reaches its local minimum at $T_e \approx 3$ keV which is followed by a re-rise of the signal' intensity until 8 keV. Above this level the signal begins to drop again.
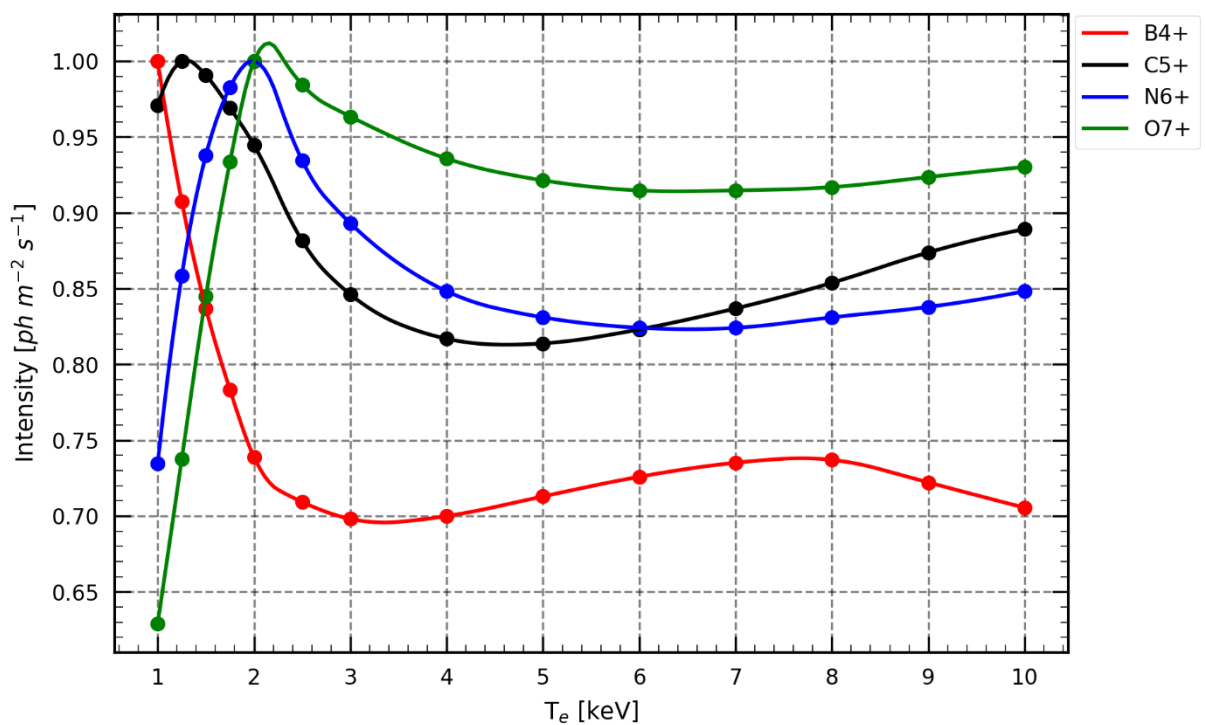
Figure 4.13. Spline fit of radiated photon intensities (normalized to 1) of selected ions as a function of electron temperature assuming the maximum electron density at $n_e = 10^{19}$ m^{-3} and 'flat' impurity profile.

Such a re-rise of a radiated intensity trends with the increase of T_e may appear counterintuitive, since the further T_e increase leads to a full ionization of an atom, and hence should lead to a continuous drop of a signal. Nonetheless, further investigation

of radial impurity emission shows that with increase of electron temperature in the plasma the emissivity distribution along minor radius shifts towards plasma edge (see Figure 4.14). The reason for that lies in geometry of the W7-X plasma. When the rise of electron temperature is observed (on the axis as well as closer to the edge), the radial emission is being pushed out from the central plasma regions towards the edge. Because the W7-X plasma is in the shape of twisted mobius strip normalized to a cylindrical volume, the further from the plasma axis the larger plasma volume of a specific parameters (n_e, T_e, impurity density). As a result, a shift of emission profile (with its unchanged shape) towards plasma edge, leads to an increase of radiated photon intensities being a consequence of a larger plasma volume emitting such radiation (as described by equation (30)). As the C/O monitor observes large semi-conical plasma volume-integrated along the cone of view, this effect plays a crucial role in analysis of a measured data.
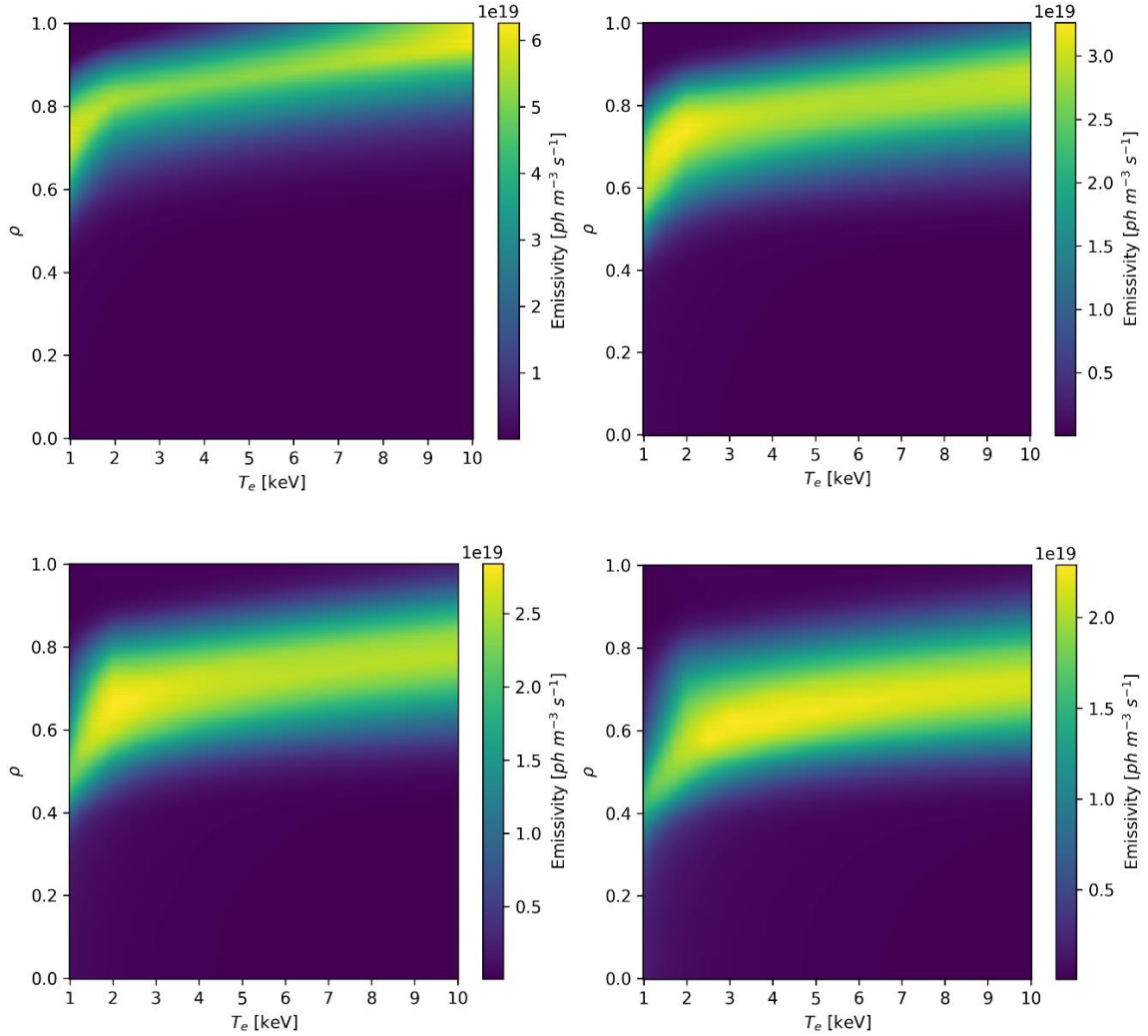
Figure 4.14. Colormap representing radial emissivity distributions of all considered ions (from top left B^{4+}, C^{5+}, N^{6+}, O^{7+}) as a function of electron temperature assuming the maximum electron density at $n_e = 10^{19}$ m^{-3} and 'flat' impurity profile.

On the other hand, comparing the obtained results with the issue discussed in the previous paragraph (4.2.1) related to the photon intensity dependencies on the electron density - in case of B line, one may notice that at $7 - 8$ keV its emissivity profile becomes pushed out of the simulation area (similarly to the n_e dependence at high T_e case). This leads to a 'drop' of the calculated photon intensities. Such a result, however, is again misleading since the impurities can also be emitted outside the LCFS (from the SOL region). Nevertheless, due to the lack of proper data, it is impossible to perform reliable simulations of the outside of LCFS plasma using the presented method.

To sum up - it is essential to notice, that assuming low electron density case, the level of impurity changes within the $T_e = 3 - 10$ keV range is approximately ±5 %, thus probably it will be difficult to measure its fluctuations accurately during experiments. Therefore one can assume, that for such plasma conditions signal rather weakly depends on the electron temperature (especially above 3 keV). As a consequence, observed changes of photon intensities can be associated with the fluctuations of the impurity level.

For a higher density case (Figure 4.15) the points of maximum intensities for all elements are shifted into the lower T_e regions compared to the low n_e case. For oxygen Lyman-α transition the strongest intensity is observed at $T_e = 1.5$ keV, while for other elements the maximum radiation seems to be emitted below the investigated T_e range. Thus, the intensities of B, C and N lines drop from the begin of the presented trends and 'stabilizes' at $T_e ≈ 3$ keV. For O line intensity trend, the plateau shape is reached above approx. 7 keV.
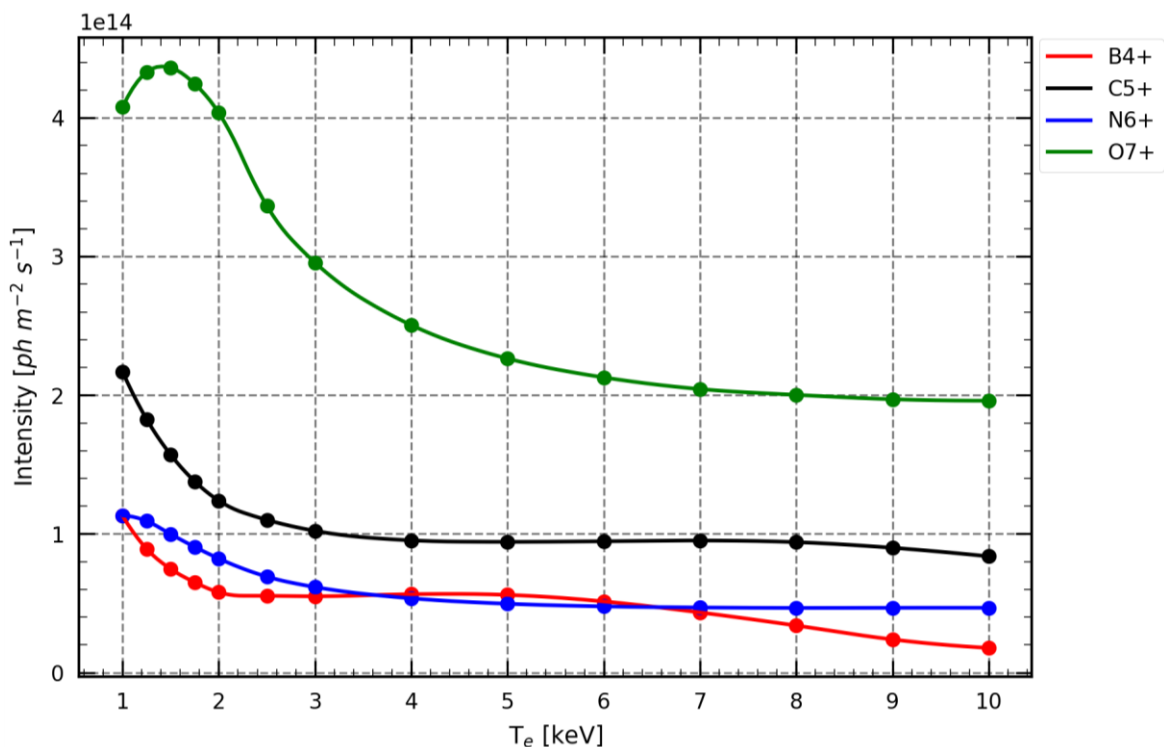
Figure 4.15. Spline fit of radiated photon intensities of selected ions as a function of electron temperature assuming the maximum electron density at $n_e = 10^{20}$ m^{-3} and 'flat' impurity profile. Each point represents ONLY a fraction of the radiation reaching the surface representing the respective detector.

Study of the normalized dependencies (illustrated in Figure 4.16) presents, that with the increase of T_e the initial intensity drop exceeds 50%, which is much stronger effect than in the low n_e case. Moreover, the lower Z, the signal drop is more rapid and occurs within the shorter temperature range: $B - 2$ keV, $C - 3$ keV, $N - 4$ keV, $O - 6$ keV. Similar behavior (referring to the B and C lines' intensities) was observed as in the case of trend of B line for the low n_e case, where the further temperature increase leads to a significant photon intensity drop.
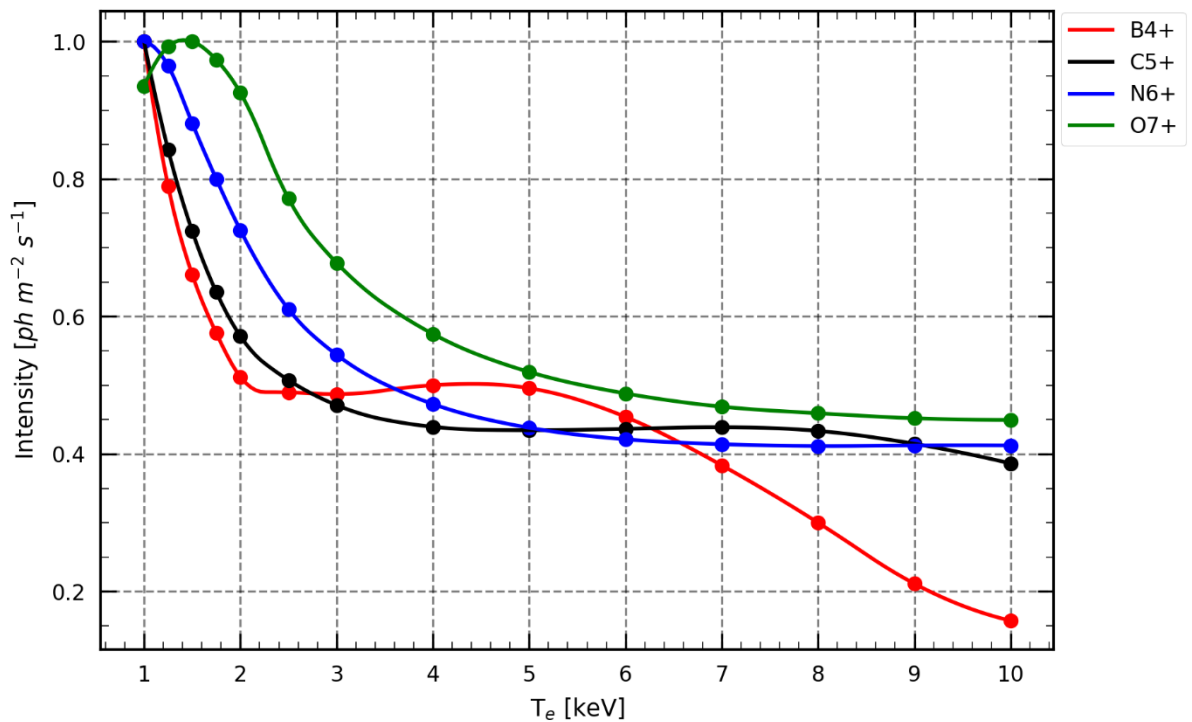
Figure 4.16. Spline fit of radiated photon intensities (normalized to 1) of selected ions as a function of electron temperature assuming the maximum electron density at n_e = 10^{20} m^{-3} and 'flat' impurity profile.

Figure 4.17 shows, that the radial emissivity distribution of B line above the 5 keV and C line above 8 keV, clearly coincides with the previous observations, where the radial emission of B line (mostly) is shifted outside the simulation region ($\rho > 1$). The total emissivity profile of B Lyman-α transition is radiated only in the simulation range with T_e less than 4 keV (upper left in Figure 4.17). Above this temperature, the emission is dominant in the edge plasma region. Similarly, for C line (upper right in Figure 4.17) only for T_e below 8 keV emitted radiation remains in the spatial range what can be included in the simulation. The N and O radial emission is fully covered by the simulation range (bottom in Figure 4.17).
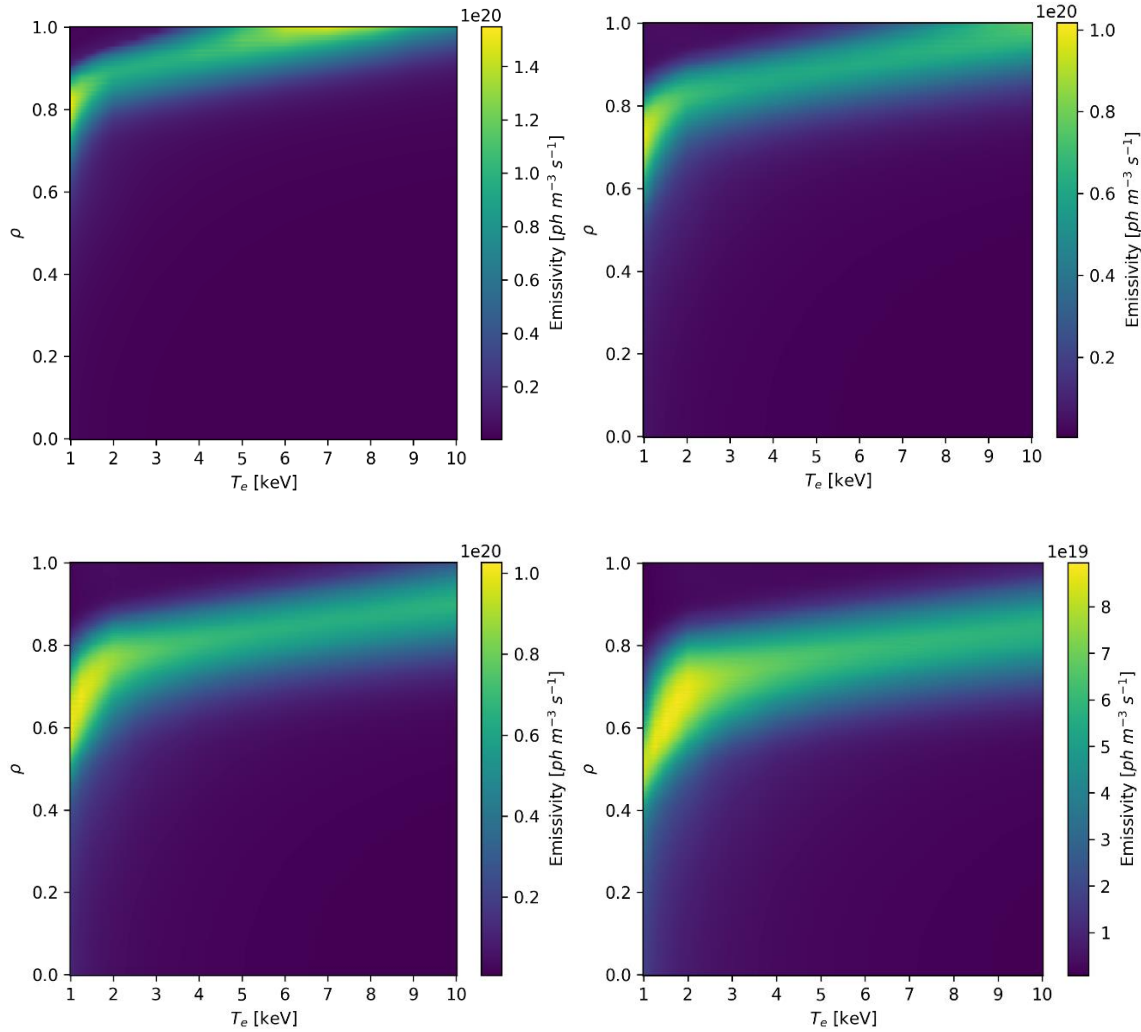
*Figure 4.17. Colormap representing radial emissivity distributions of all considered ions (from top left B^{4+}, C^{5+}, N^{6+}, O^{7+}) as a function of electron temperature assuming the maximum electron density at $n_e = 10^{20}\ m^{-3}$ and **'flat'** impurity profile.*

To summarize: this analysis shows, that for 'flat' impurity profile the calculations of N and O lines' intensities within relevant density and temperature ranges provide accurate results with reliable data, while for C and especially B cases they can become imprecise due to lack of the data describing the radiation fraction emitted outside LCFS. For high density case and T_e range above 3 keV, the radiated intensities of C, N and O almost do not depend on electron temperature. The photon flux intensities varies by ±5% (similar to the low n_e case) within the given T_e ranges. Therefore, if assuming 'flat' radial impurity distribution it can be concluded, that above low temperature range (Te > 3 keV) – the change of a potential signal being larger than 10% could be an indicator of increase of impurity content in the plasma.

4.2.2 Photon intensity dependencies for 'peaked' impurity profiles

4.2.2.1 Dependence on the electron density

During W7-X operation plasma may be characterized by a certain conditions under which the impurity accumulation may occur. These would be e.g., high electron density, negative radial electric field due to the IRC scenario [74]. This could be a sign of a transition from anomalous to neoclassical impurity transport regime (more detailed description was already presented in the section 1.7). Such phenomena are characterized by a strong impurity confinement close to the plasma axis, and thus more significant part of radiation of light impurity (B, C, N and O) originate from the central plasma. The transition from and to neoclassical impurity transport (leading to a different radial impurity distributions) can take approx. 200 ms [74] and within the given time the radial impurity distribution reshapes to the 'peaked' impurity profile. In contrast to the aforementioned study, here the 'peaked' impurity profile is taken under consideration. The profile shape (radial impurity distribution) was based on experimental results from the discharge *20181009.016*. These results were obtained by measuring the C line, however, since all the elements are characterized by a low atomic number ($Z = 5 - 8$), it can be assumed, that their 'peaked' distribution shapes will be similar [75]. To facilitate data analysis and enable their comparison, the average value of density of both ('peaked' as well as 'flat') radial impurity distributions were assumed to be the same and equal $2 \cdot 10^{17}\,\mathrm{m^{-3}}$.

When considering low electron temperature (1 keV), the O line intensity is significantly stronger than assuming 'flat' impurity profiles (see Figure 4.18). As with the results obtained in the first analysis (where 'flat' impurity distribution was assumed), there is a clear dependency of intensity radiated towards the detectors and the electron density. The most intense radiation corresponds to the heaviest element (O) and decreases with atomic number. The N line, however, is still the weakest due to the MLM's poor reflectivity.
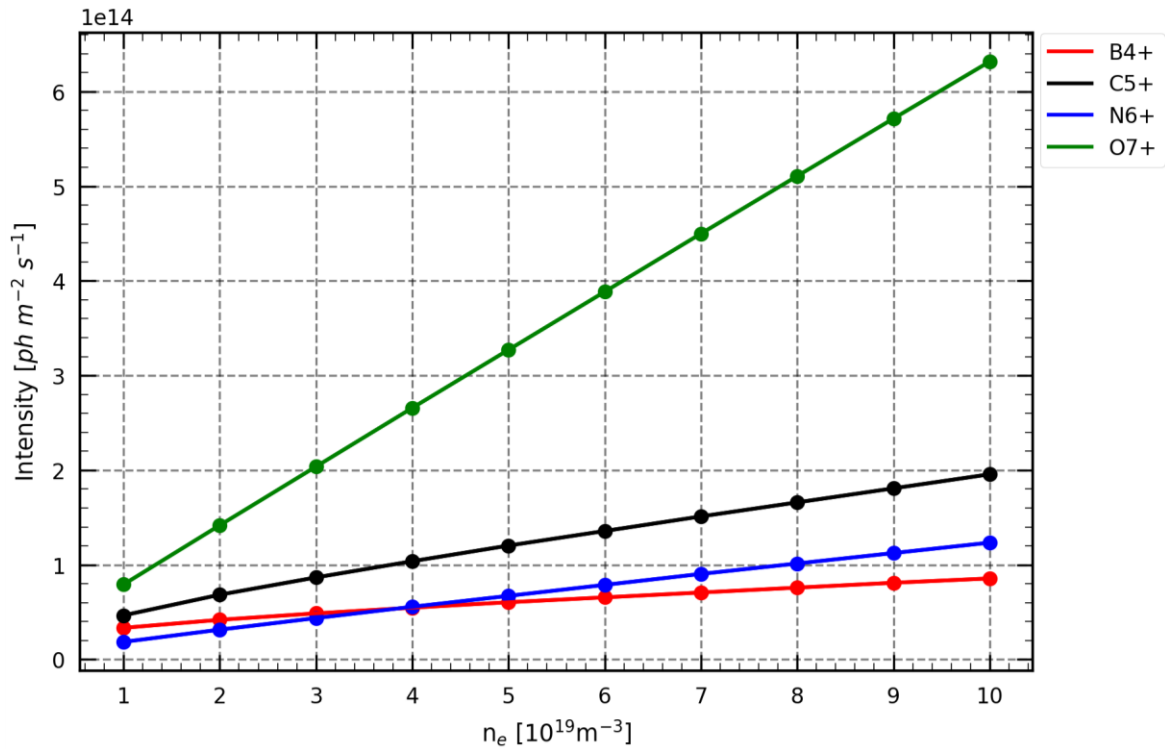
Figure 4.18. Spline fit of radiated photon intensities of selected ions as a function of electron density assuming the maximum electron temperature at T_e = 1 keV and 'peaked' impurity profile. Each point represents ONLY a fraction of the radiation reaching the surface representing the respective detector.

The strongest, linear gradient is observed for the heaviest element (O) and the lowest for B line (see Figure 4.19). Within the given density range the signal can increase c.a. 5× for O and about 2.5× for B. It is essential to notice, that for these set of kinetic profiles the O^{7+} Lyman-α intensity is significantly stronger than for other elements.
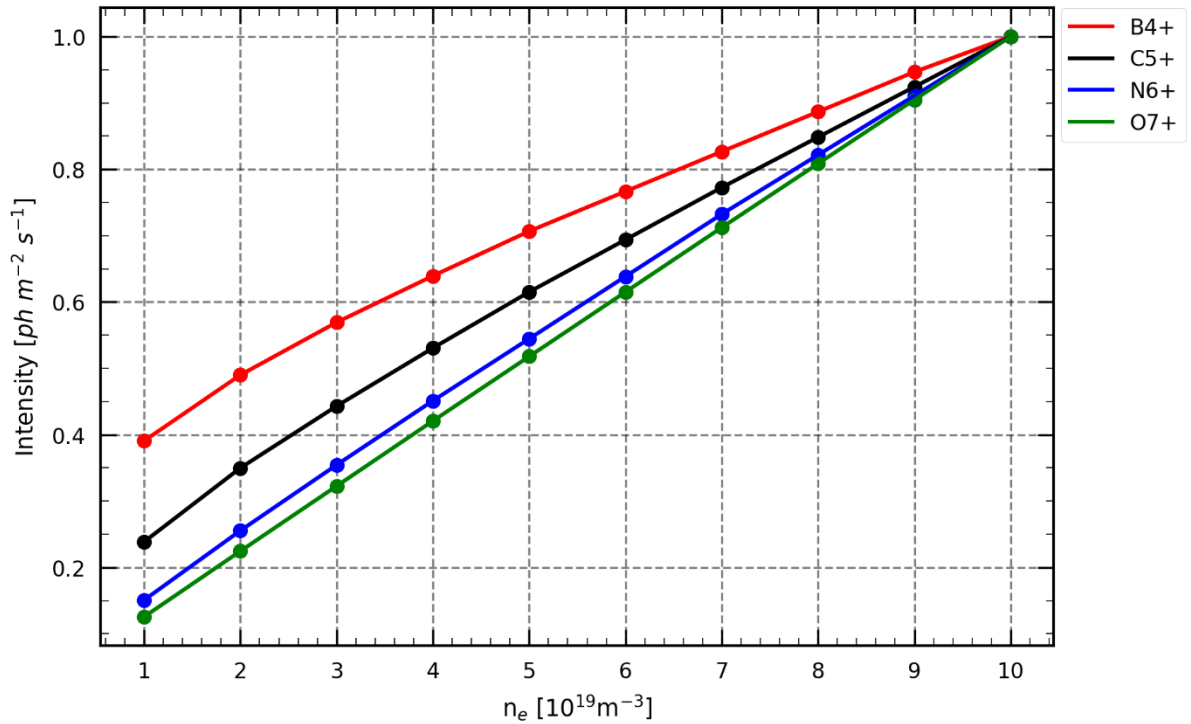
*Figure 4.19. Spline fit of radiated photon intensities (normalized to 1) of selected ions as a function of electron density assuming the maximum electron temperature at $T_e = 1\,keV$ and **'peaked'** impurity profile.*

The radial emissivity distributions (Figure 4.20) for 'peaked' profile under the given plasma conditions again show that the larger electron density, the more radiation is emitted from the plasma center. This effect is weaker when considering B Lyman-α transition, but becomes substantial for heavier elements. The C line is emitted mostly from the $\rho = 0.6 - 0.8$ region, however some radiation fraction originates also from the central plasma region at $\rho \approx 0 - 0.4$. While for N the most intense radiation is distributed both in the plasma axis and in the half radius at $\rho \sim 0.6$, the O line emission originates mostly from the plasma center. For B and C lines the central plasma temperatures are too high leading to their full ionization. Therefore most of their emission comes from the outer plasma regions.
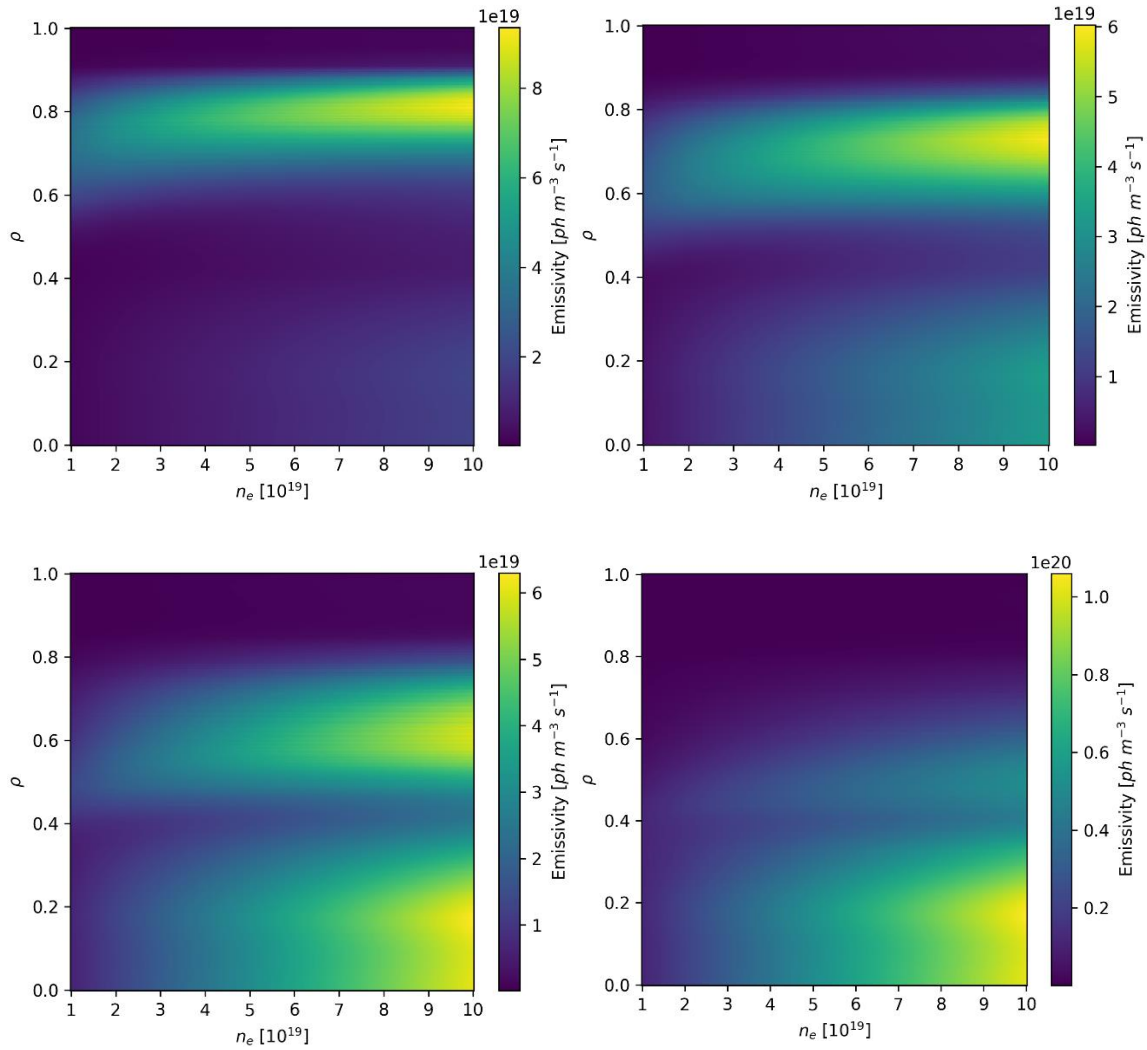
Figure 4.20. Colormap representing radial emissivity distributions of all considered ions (from top left B^{4+}, C^{5+}, N^{6+}, O^{7+}) as a function of electron density assuming the maximum electron temperature at $T_e = 1$ keV and 'peaked' impurity profile.

Similar conclusions can be drawn when considering photon intensities of N and O lines at the high temperature case ($T_e = 10$ keV) - Figure 4.21. Within the given density range the maximum intensity of O line increases by approx. ≈2.5×, which is approx. 2× less significant than for the low temperature case ($T_e = 1$ keV). However, when analyzing C line intensity change, the intensity gradient was continuously decreasing with the increasing of electron density, that was not the case when assuming low T_e profile (Figure 4.22). For $T_e = 10$ keV the B line photon intensity drops over the whole density range by almost 50% compared to the low T_e case.
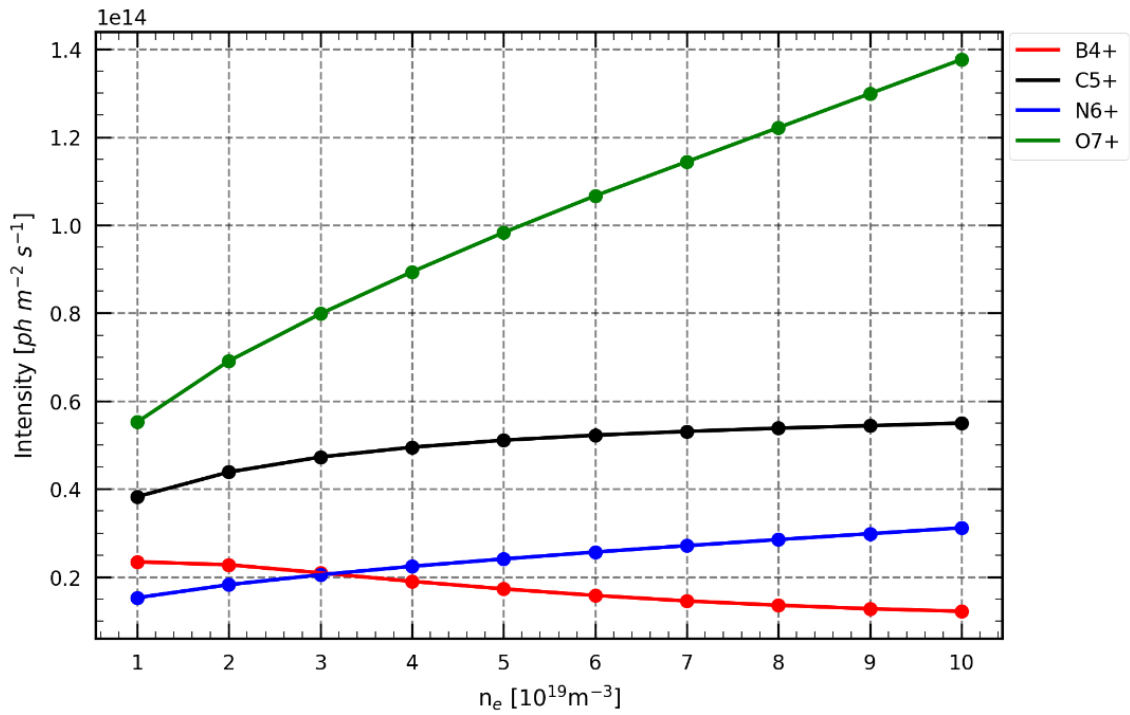
Figure 4.21. Spline fit of radiated photon intensities of selected ions as a function of electron density assuming the maximum electron temperature at $T_e = 10 \, keV$ and 'peaked' impurity profile. Each point represents ONLY a fraction of the radiation reaching the surface representing the respective detector.
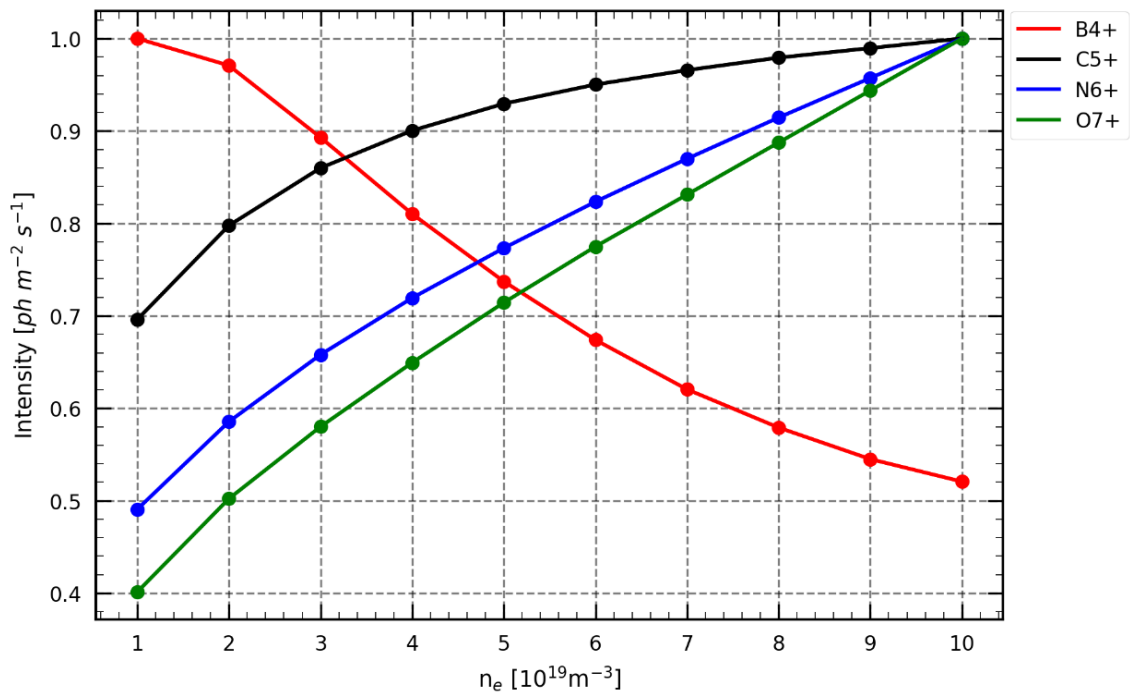
Figure 4.22. Spline fit of radiated photon intensities (normalized to 1) of selected ions as a function of electron density assuming the maximum electron temperature at $T_e = 10 \, keV$ and 'peaked' impurity profile.

Similarly to the low T_e scenario - the reason for that is the radial emissivity of the B line which is emitted from the very edge of a central plasma and SOL region. As for the C, the most intense radial emissivity within the density range $n_e = 1 - 2 \cdot 10^{19}$ m^{-3} is emitted in the central plasma region. At higher densities the emissivity profile is pushed out into the SOL region. These radial emissivity distributions are presented in Figure 4.23.
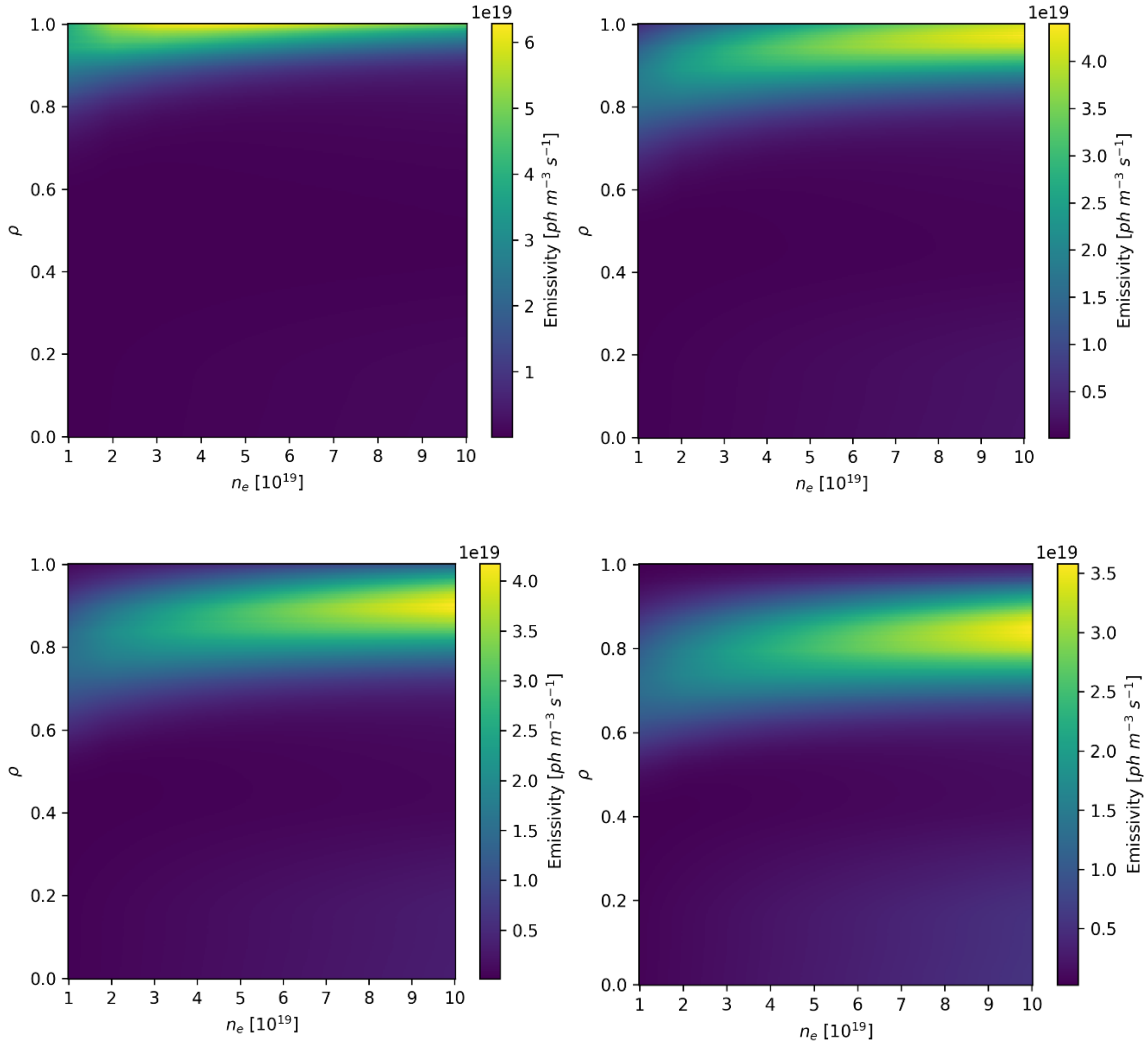
Figure 4.23. Colormap representing radial emissivity distributions of all considered ions (from top left B^{4+}, C^{5+}, N^{6+}, O^{7+}) as a function of electron density assuming the maximum electron temperature at **$T_e = 10$ keV** *and* **'peaked'** *impurity profile.*

4.2.2.2 Dependence on the electron temperature

The last part of this analysis was devoted to the dependencies of photon flux intensities as a function of electron temperature assuming 'peaked' impurity profile

(see Figure 4.24). For the O-line a decrease of the radiated intensity is observed from begin of the trendline at 1 keV reaching the local maximum again at 2 keV followed by a continuation of the downward trend. The N-line reaches its local maximum at about 2 keV followed by the similar trend as for the O-line. The maximum photon intensities of B and C-lines are observed at the lowest considered temperatures (1 keV), but above some certain T_e levels ($T_e \approx 3 - 5$ keV) their intensities begin to raise. For B-line, however, above 8 keV the signal slightly drops again.
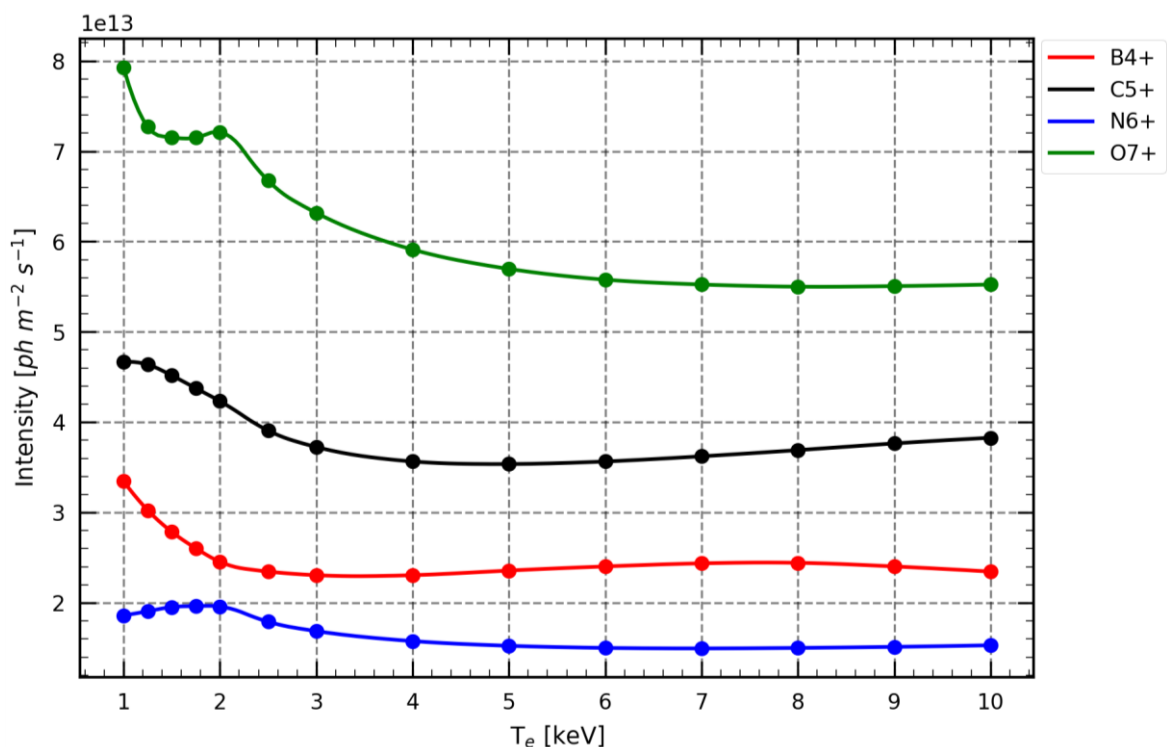
Figure 4.24. Spline fit of radiated photon intensities of selected ions as a function of electron temperature assuming the maximum electron density at $n_e = 10^{19}$ m^{-3} and 'peaked' impurity profile. Each point represents ONLY a fraction of the radiation reaching the surface representing the respective detector.

This effect is better seen in Figure 4.25 presenting the normalized trends. In the temperature range from 1 to 2 keV there is a clear drop of O photon intensity followed by its local maximum at $T_e = 2$ keV, however it is still approximately 10% lower than for 1 keV. Again, there is clear intensity signal increase above some characteristic temperature: B – 3 keV, C – 5 keV, N – 7 keV and O – very slight increase above 9 keV. Nevertheless, above 3 – 4 keV the intensity changes of all considered elements may be assumed as not crucial since they does not exceed ± 5%. In the low T_e range the

photon intensities variations are more significant, what leads to growing difficulty of interpretation of experimental data. Therefore, in order to draw some reliable conclusions, a detailed modelling will be needed.
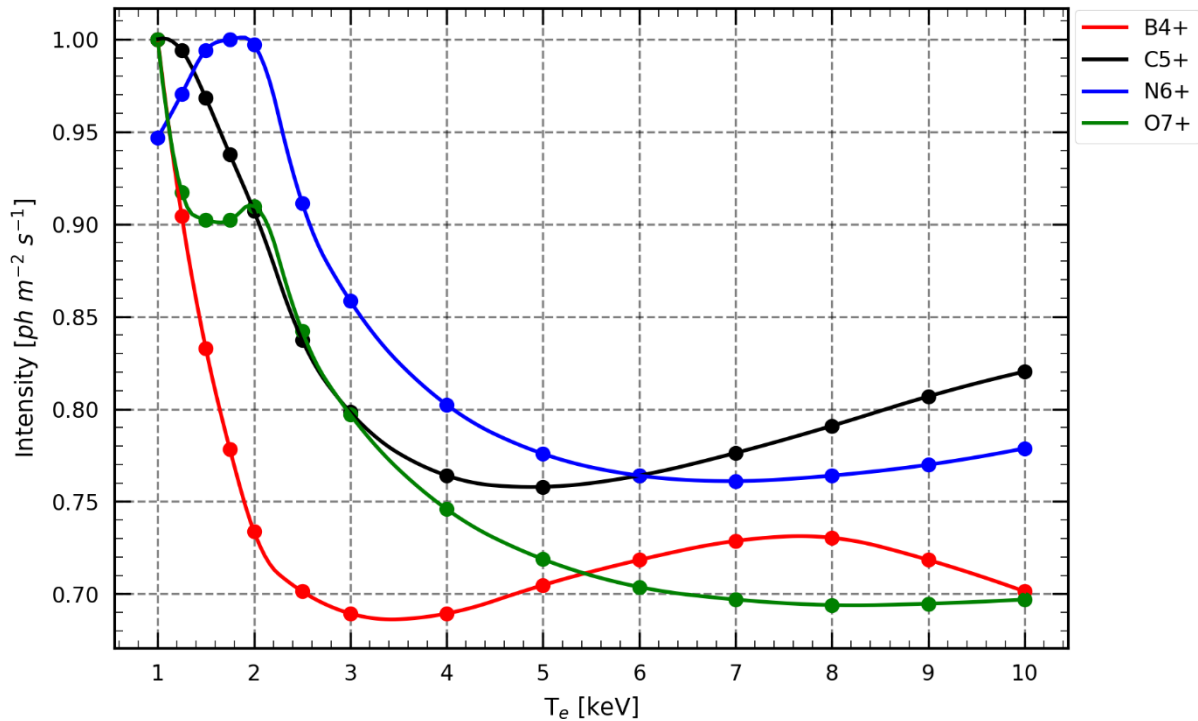
Figure 4.25. Spline fit of radiated photon intensities (normalized to 1) of selected ions as a function of electron temperature assuming the maximum electron density at $n_e = 10^{19}\ m^{-3}$ and 'peaked' impurity profile.

Like for the 'flat' impurity distribution profile – the reason for a signal increase above some characteristic temperature levels is correlated with radial emissivity profile being shifted from the center towards the edge plasma region (see Figure 4.26). Therefore, most of the radiation originates from larger plasma volume and even though the maxima of emissivity profiles are less intense for higher T_e (especially for C and O lines), their location in the plasma determines the larger number of emitted photons. Moreover, for O-line it is clearly seen that with $T_e = 1$ keV the significant fraction of emitted radiation originates from the center of the plasma (similarly to the N-line). At the lowest temperature the total emissivity was radiated strongly from the center ($\rho \approx 0 - 0.4$) while at $T_e = 2$ keV this region is shifted towards $\rho \approx 0.5 - 0.7$. Between 1 and 2 keV the emissivity distribution reshapes becoming dominant in the mid-radius

region. This reflects the shape of a O intensity trendline observed between 1 and 1.5 keV (Figure 4.25), where the signal drops to reach the local minimum.
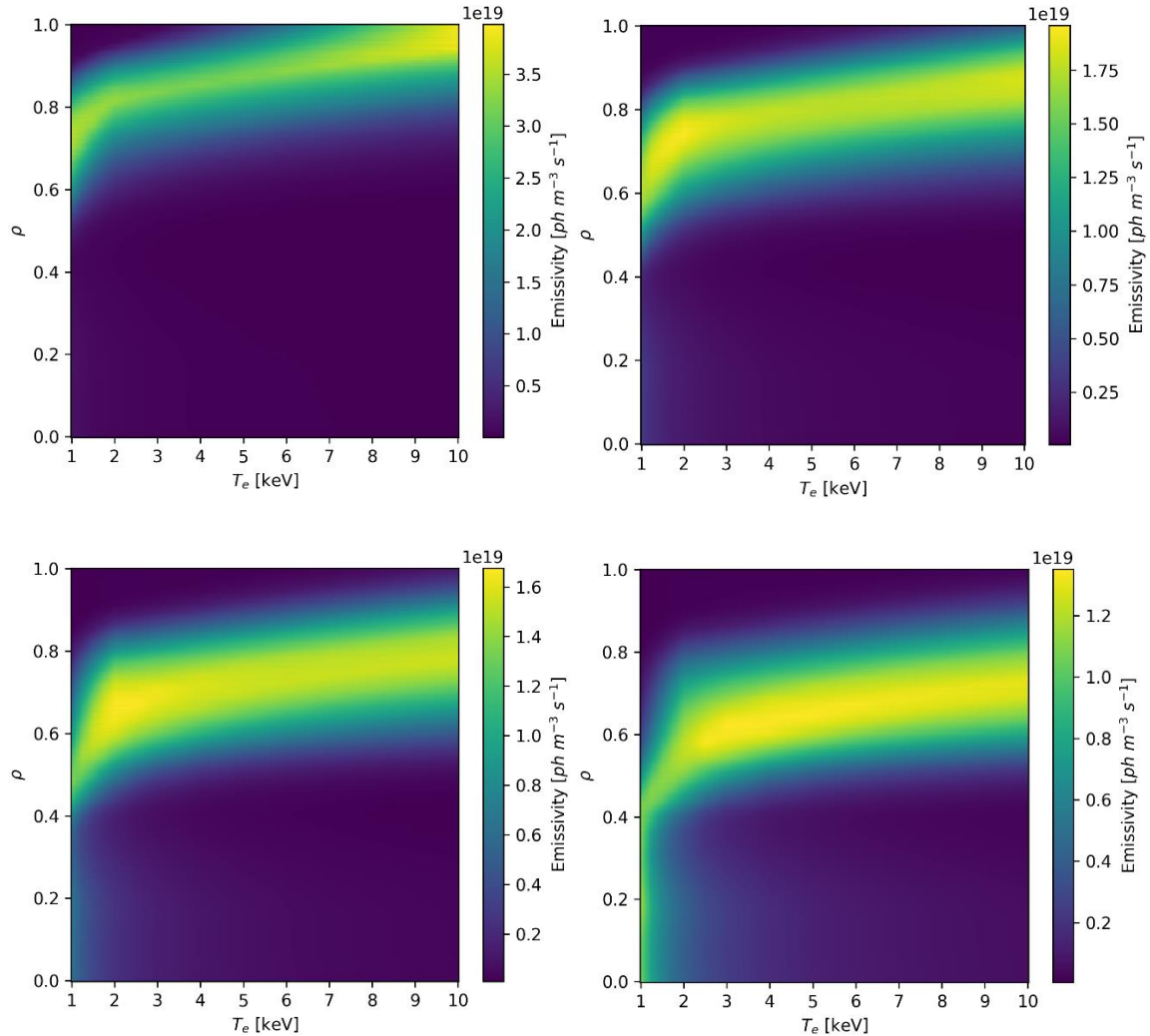
Figure 4.26. Colormap representing radial emissivity distributions of all considered ions (from top left B^{4+}, C^{5+}, N^{6+}, O^{7+}) as a function of electron temperature assuming the maximum electron density at $n_e = 10^{19}$ m^{-3} and 'peaked' impurity profile.

The spline fits presented in Figure 4.27 illustrate the dependencies of the intensities on the electron temperatures assuming $n_e = 10^{20}$ m^{-3}. Again, the most intense radiation is emitted by oxygen and decreases almost exponentially with increase of T_e. Similar behavior is observed for other elements.
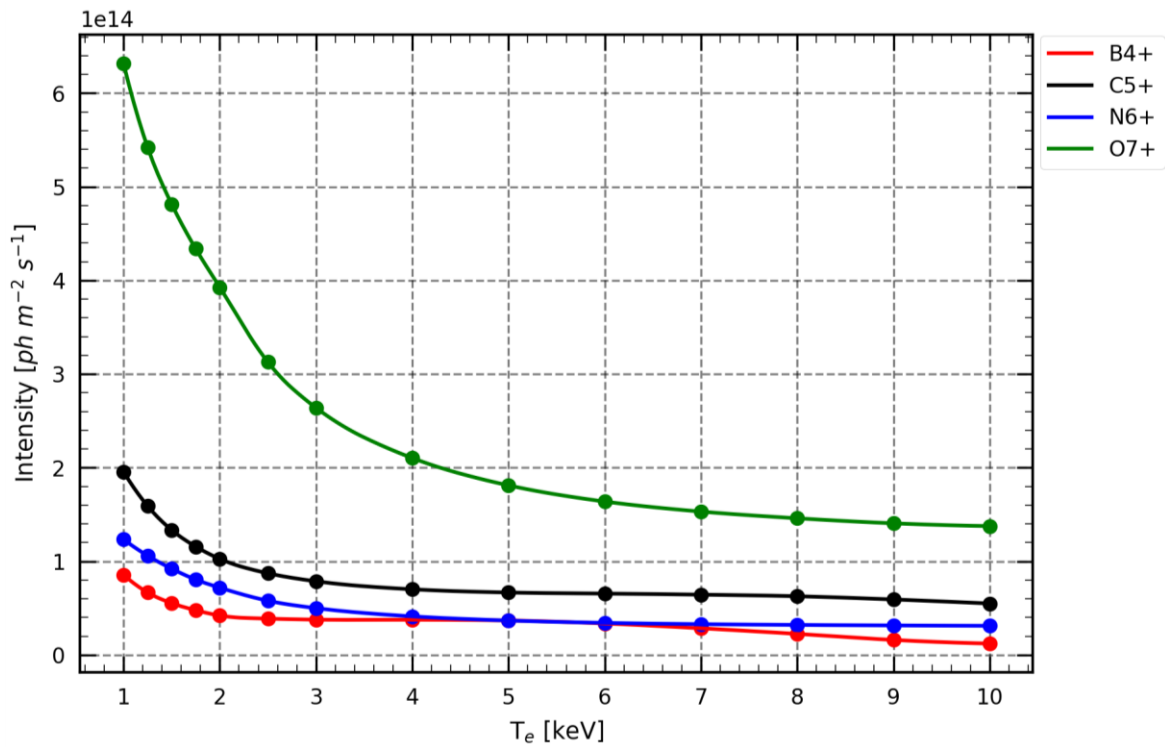
Figure 4.27. Spline fit of radiated photon intensities of selected ions as a function of electron temperature assuming the maximum electron density at $n_e = 10^{20}$ m^{-3} and 'peaked' impurity profile. Each point represents ONLY a fraction of the radiation reaching the surface representing the respective detector.

The normalized intensities illustrated in Figure 4.28 show, that the percentage drop of signals is very similar for all considered elements. Similarly to the afore described cases, the B-line begins to drop above some certain temperature level (T_e = 5 keV) what is caused by a radiance profile expansion outside the ρ = 1.
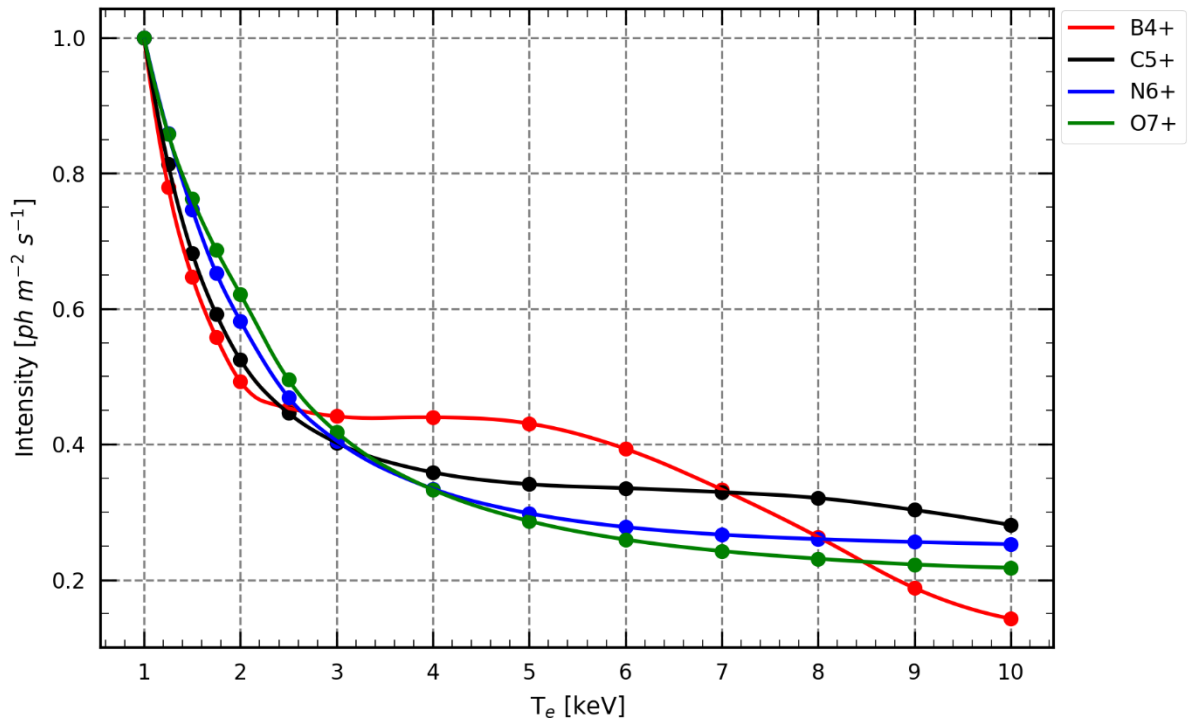
Figure 4.28. Spline fit of radiated photon intensities (normalized to 1) of selected ions as a function of electron temperature assuming the maximum electron density at $n_e = 10^{20}\ m^{-3}$ and 'peaked' impurity profile.

Figure 4.29 illustrates, that for the high density case, 'peaked' impurity profile and $T_e = 1$ keV, the significant part of radiated emissivity originates from the very center of a plasma. This is especially evident for O and N lines, but also the significant fraction of C line is emitted from the plasma axis. In general, the higher the temperature, the farther from the plasma center the maximum emission is. However, for O and N lines there is still a significant emission that is radiated from the core plasma region but only within electron temperature range below $T_e = 3 - 4$ keV.
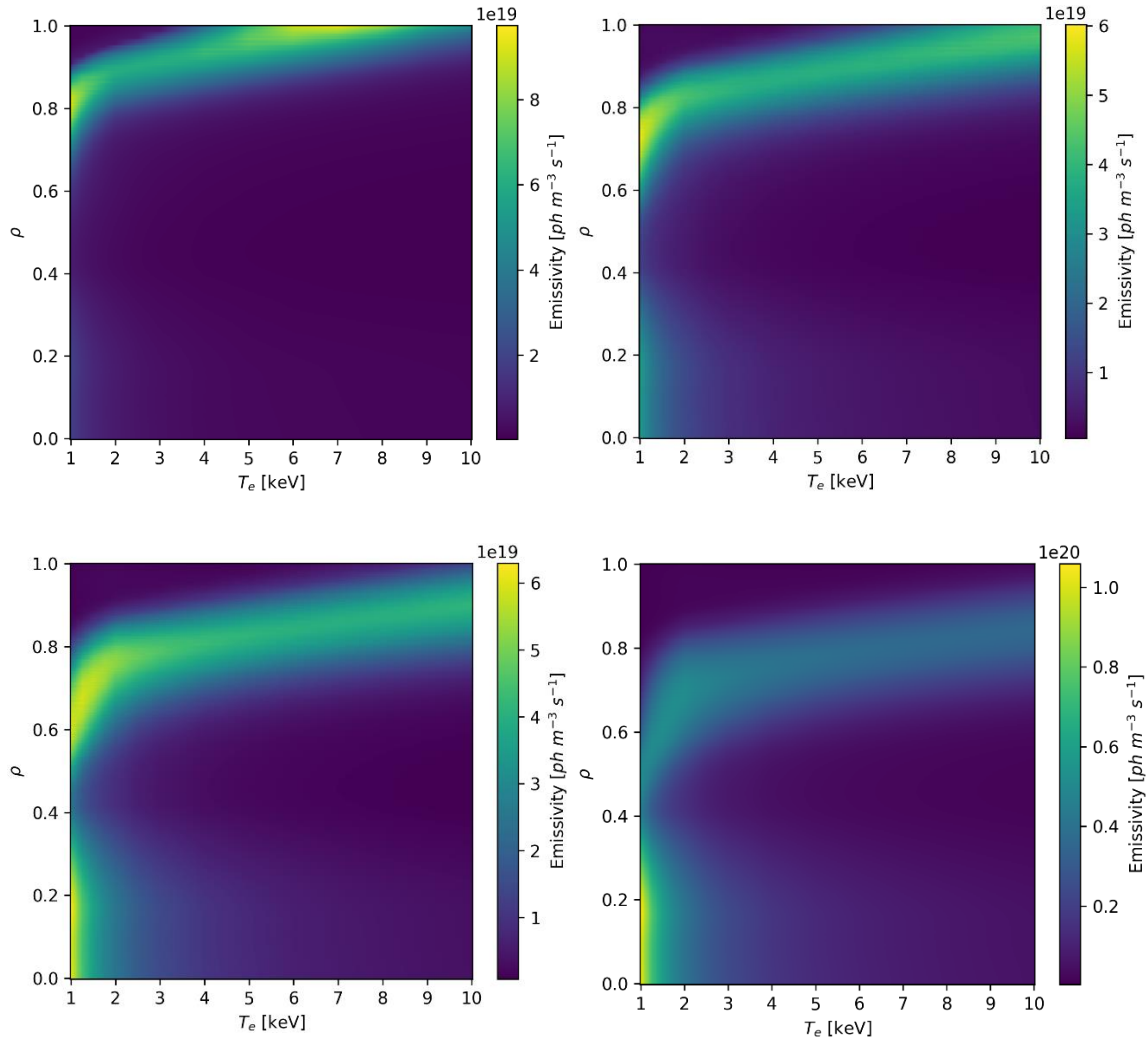
Figure 4.29. Colormap representing radial emissivity distributions of all considered ions (from top left B^{4+}, C^{5+}, N^{6+}, O^{7+}) as a function of electron temperature assuming the maximum electron density at $n_e = 10^{20}$ m^{-3} and 'peaked' impurity profile.

4.2.3 Comparison of photon intensity dependencies for 'peaked' and 'flat' impurity profiles

4.2.3.1 Dependence on the electron density

Previous analyzes presented the impact of impurity profiles' shapes ('peaked' and 'flat') on the radiated photon intensities and their dependences on the kinetic profiles in plasma. Figure 4.30 presents a comparison of the trend lines of the emitted intensities for both types of radial impurity distributions in plasma: 'flat' (solid lines) and 'peaked' (dashed lines) as a function of electron density assuming the maximum $T_e = 1$ keV. The line intensities of C and B are lower when comparing the 'peaked' and 'flat' impurity

profiles. For N line there is almost no difference in the line intensities over the considered density range. However, the O line intensities are approx. 50% higher for 'peaked' impurity profile.
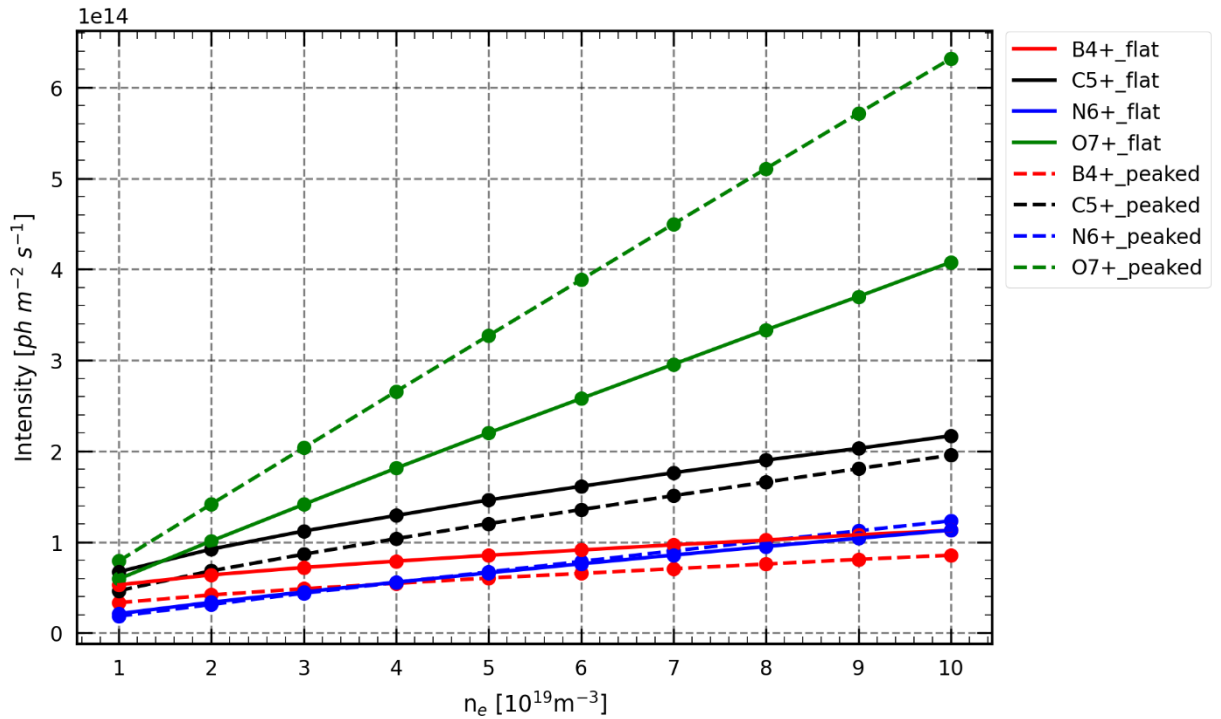
*Figure 4.30. Comparison of spline fits of radiated photon intensities of selected ions as a function of electron density for **'flat'** (presented in Figure 4.6) and **'peaked'** (presented in Figure 4.18) assuming the maximum electron temperature at* **T_e = 1 keV**.

The reason for this is the distribution of the radial emission of O Lyman-α line, which is especially clearly observable when comparing the emissivity distributions for both impurity profiles: 'flat' (Figure 4.31 – left) and 'peaked' (right). It can be observed, that the O radiation for 'peaked' profile originates mostly from the plasma center and the emissivity profiles are much broader (compared to the 'flat' case) emitting much stronger photon intensity. For N line the central emissivity radiation is significantly less intense while for B and C the radiation maximum is shifted towards the plasma edge.
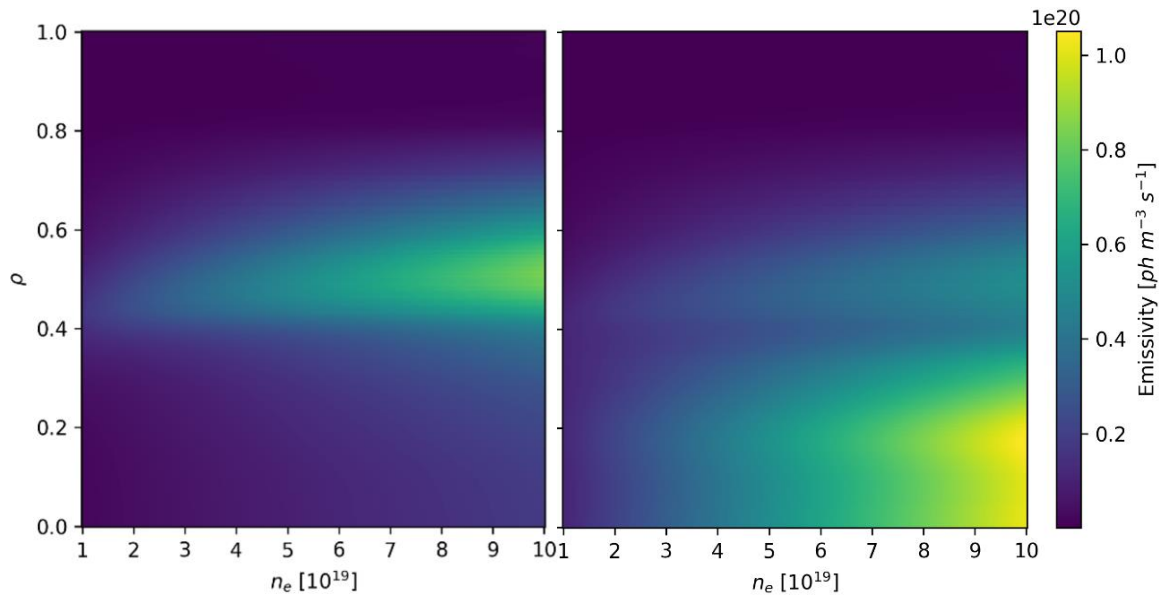
*Figure 4.31. Comparison of radial emissivity distributions of O^{7+} line as a function of electron density for **'flat'** (left) and **'peaked'** (right) impurity profiles assuming the maximum electron temperature at T_e = 1 keV.*

At high T_e = 10 keV, the 'flat' impurity distribution causes significantly more intense lines radiation (by approximately 50%) for all elements (including O) compared to the 'peaked' impurity profile - see Figure 4.32.
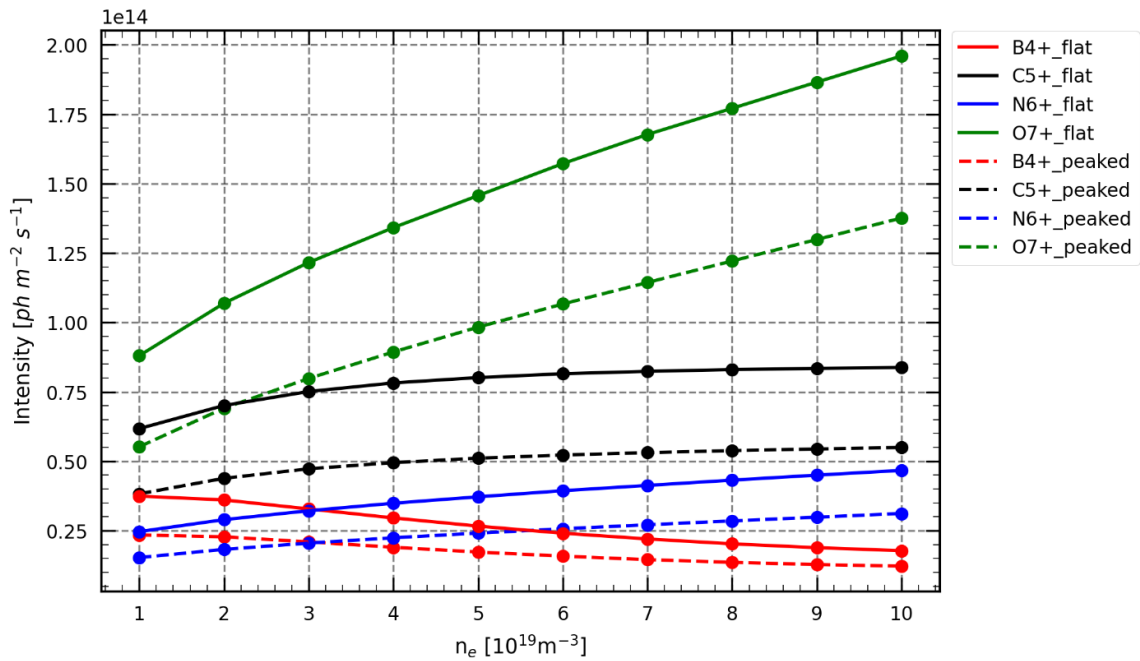
*Figure 4.32. Comparison of spline fits of radiated photon intensities of selected ions as a function of electron density for **'flat'** (presented in Figure 4.9) and **'peaked'** (presented in Figure 4.21) assuming the maximum electron temperature at $T_e = 10$ keV.*

4.2.3.2 Dependence on the electron temperature

Comparing radiated intensities as a function of T_e for profile with maximum $n_e = 10^{19}$ [m^{-3}] and both considered radial impurity distributions (Figure 4.33) it may be noticed, that the total emitted radiation depends strongly on the electron temperature levels, especially in 1 – 3 keV range. This is particularlyclear when comparing O line for the 'flat' impurity profile, which is approximately 25% less intense for 1 keV compared to the 'peaked' shape (also presented in Figure 4.30). Up to 1.25 keV the total radiated intensity for the 'peaked' impurity profile is higher than for the 'flat' one. Above 3 keV, both trends have almost identical shape. In the case of the other elements, the 'flat' impurity profiles (solid lines) lead to a significantly stronger radiation flux (by approx. 50%) compared to the 'peaked' profiles (dashed lines) over the total considered T_e range.
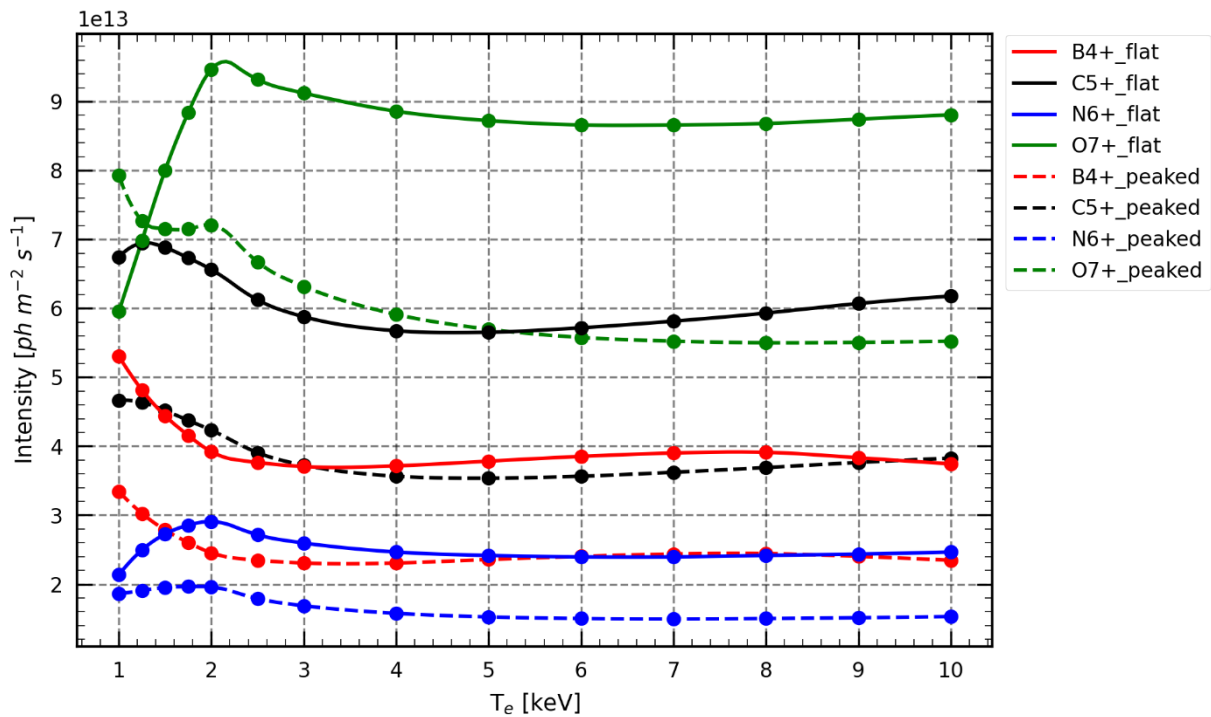
*Figure 4.33. Comparison of spline fits of radiated photon intensities of selected ions as a function of electron temperature for **'flat'** (presented in Figure 4.12) and **'peaked'** (presented in Figure 4.24) assuming the maximum electron density at $n_e = 10^{19} m^{-3}$.*

Similar behavior is observed when comparing both impurity profile shapes but assuming maximum $n_e = 10^{20} m^{-3}$ – see Figure 4.34. The same dependence for low electron temperature (1 – 2 keV) was noticed as in the case of low electron density. Above a certain electron temperature level – 3 keV for B, C and N-lines and 5 keV for O-line the trend line becomes flat for both impurity profiles' shapes. The intensities obtained with an assumption of 'flat' distribution are always higher than for 'peaked' impurity distribution for B, C and N lines, however for O line this is valid only for T_e higher than 2 keV.
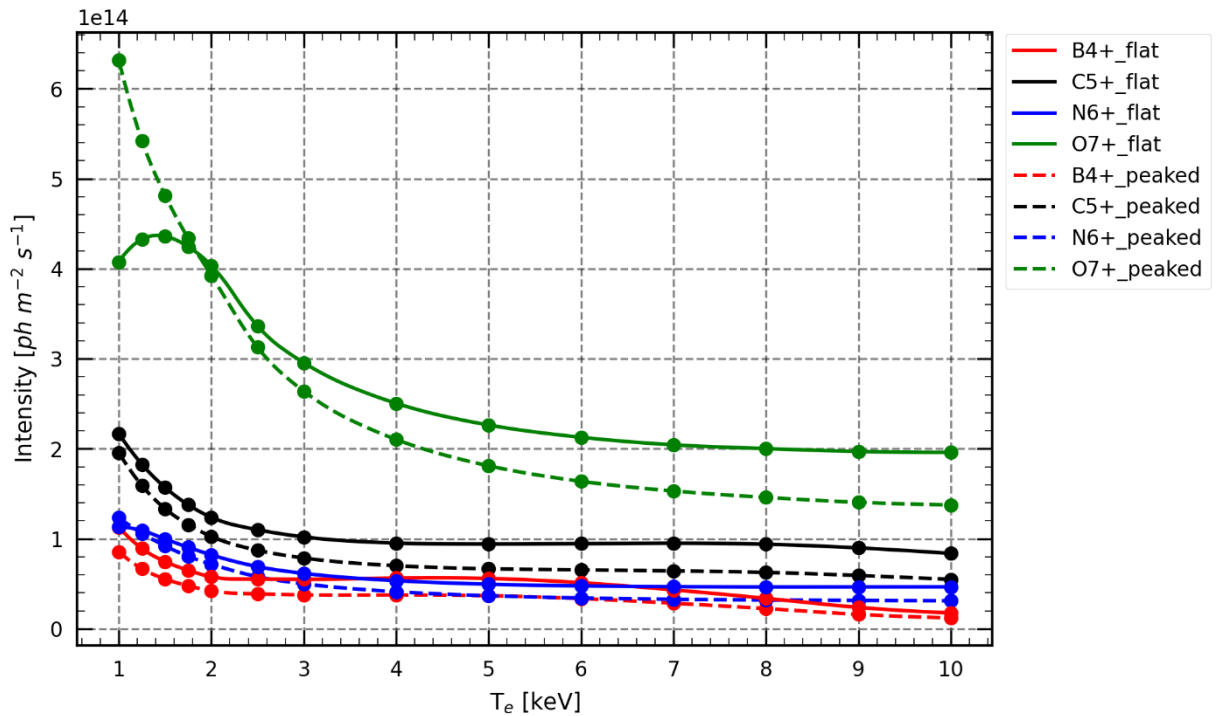
Figure 4.34. Comparison of spline fits of radiated photon intensities of selected ions as a function of electron temperature for **'flat'** *(presented in Figure 4.15) and* **'peaked'** *(presented in Figure 4.27) assuming the maximum electron density at* **$n_e = 10^{20}\,m^{-3}$.**

4.3 Case study of radiated photon intensities with respect to the C/O monitor system's efficiency – simulation approach [76]

The purpose of the final analysis was to check how strong photon intensities would reach the respective detectors if the system was in operation during the last operational phase OP1.2b. To do so, the reference discharge *20181009.016* was selected due to the observation of a clear C accumulation in the plasma center. This analysis was performed for two energy channels - C and O - since only these channels are planned to be commissioned during the OP2.0. Time evolutions of the main plasma parameters are presented in Figure 4.35.
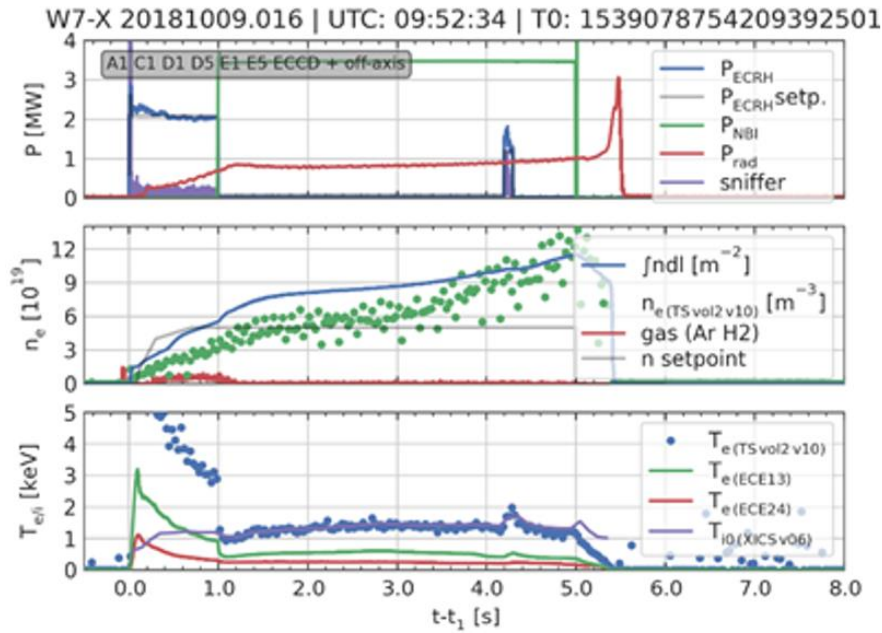
Figure 4.35. Time evolution of main plasma parameters: ECRH power (P_{ECRH}), radiated power (P_{rad}), line integrated electron density ($\int ndl$), central electron density provided by Thomson Scattering (TS) system ($n_{e(TSvol2v10)}$), central electron temperature provided by TS ($T_{e(TS\,vol2v10)}$), central electron temperature provided by ECE ($T_{e(ECE13)}$) (Electron Cyclotron Emission [77]), half radius electron temperature ($T_{e\,(ECE24)}$) and the central ion temperature from ECE system provided by XICS diagnostic system ($T_{i0(XICS)\,v06}$).

The radial distribution of C^{6+} line was measured using CXRS system, but without the simultaneous measurement of the O^{8+} line. Nevertheless, since the considered elements have similar atomic numbers, for the sake of analysis' simplification it was assumed that their radial distributions can be identical [75]. To get a better understanding of the system's response depending on the impurity profile shape, the average impurity density of a 'peaked' profile in the plasma were then converted into 'flat' distributions but assuming its identical content (as already described in the section 3.2.5).

The reason for such an approach was to investigate an impact of different radial impurity distributions (assuming their equal content in the plasma) on the emitted photon intensities under equivalent experimental conditions. Furthermore, one needs to remember that the system will provide a volume-integrated information about the change of impurity content from a large plasma volume. Because of that, it is important to check, how sensitive the system will be on a possible accumulation of

impurities in a specific plasma region and whether it will be able to detect this effect. The simulation procedure is similar to the examples presented in the previous chapter. The CXRS data were measured with time resolution of 100 ms, therefore the first step was to determine the kinetic profiles ($n_e(r)$, $T_e(r)$) of the considered discharge. Since the CXRS provides information about the fully ionized radial impurity distribution in the plasma and the procedure of emissivity calculation requires total impurity density information - it is necessary to perform calculations using pySTRAHL code. This is necessary to determine the experimental profile of a total impurity content in the plasma, and consequently to get an information about their fractional abundances. Hence, again, the set of plasma kinetic parameters together with diffusion (D) and convection velocity (V) profiles are required. Figure 4.36 presents an example of kinetic (left) as well as D and V profiles (right) corresponding to the exemplary time frame t = 4.7 s of the discharge used in the simulation.
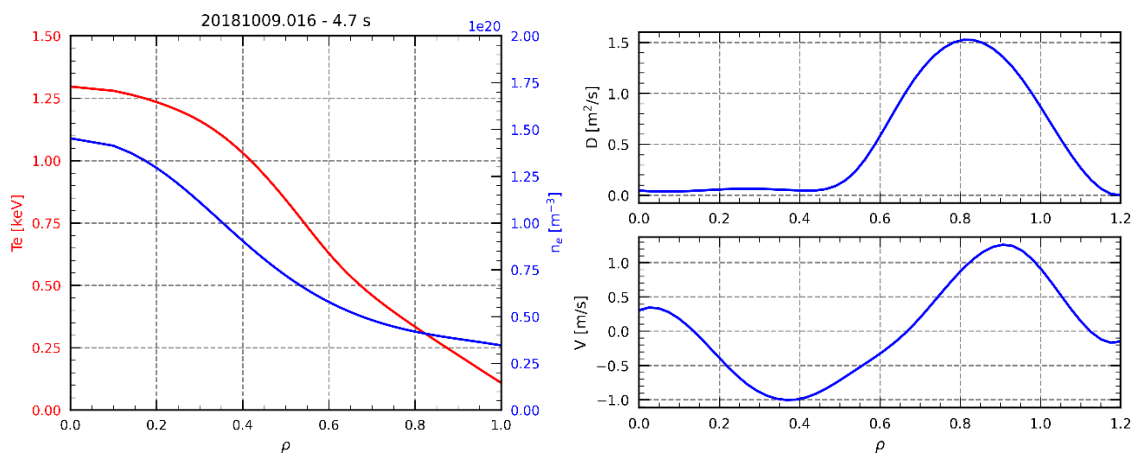
Figure 4.36. Plasma kinetic profiles for the discharge 20181009.016 at a time t = 4.7 s (left) and diffusion (right top) and convection velocity (right bottom) parameters used in the simulations with the pySTRAHL code.

Figure 4.37 illustrates the C^{6+} experimental data (t = 4.7 s) measured by CXRS system (blue line) as well as the fitted profile (purple line) calculated using pySTRAHL code.
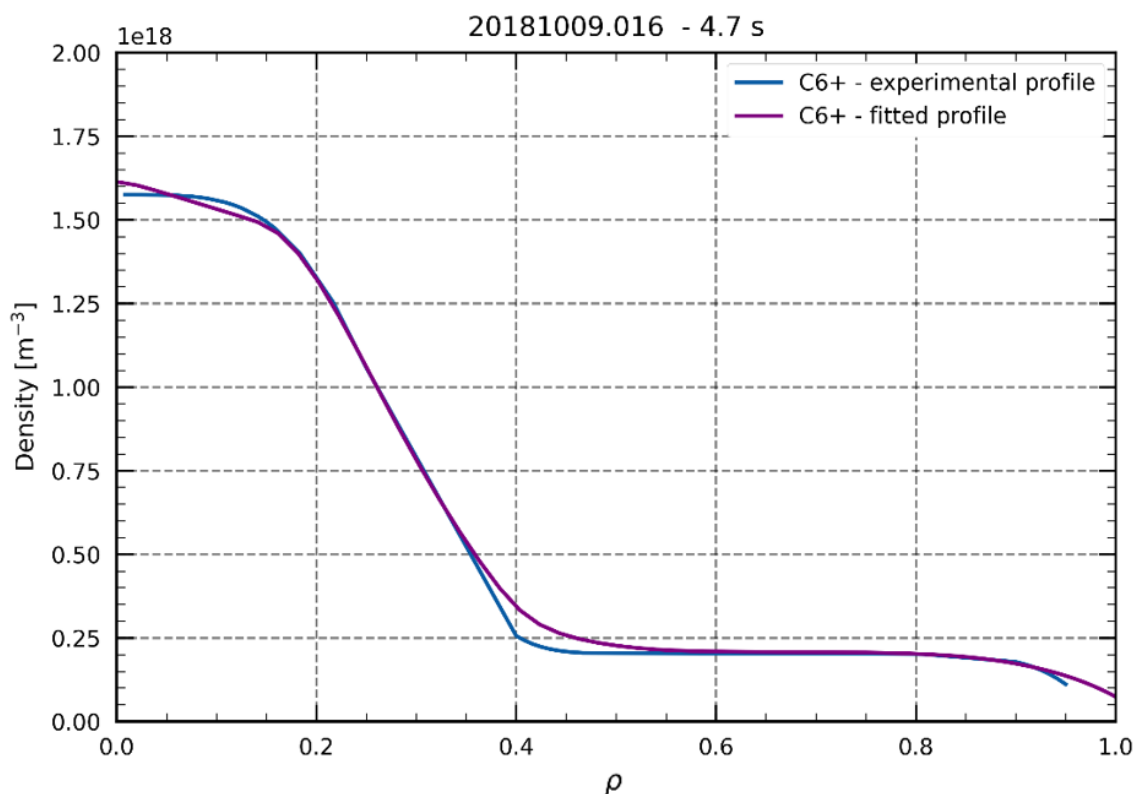
Figure 4.37. Radial impurity profile of C^{6+} registered by the CXRS system at t = 4.7 s (blue line). Purple line represents the fitted profile calculated using pySTRAHL code.

This set of information is then used by the C/O monitor code to calculate the emissivity of a given transition as a function of r_{eff} based on formula (33), followed by the radiated photon flux intensity calculation. The average value of each measured impurity density profile is then calculated from the formula (32), which serves as the basis for comparing the calculation results obtained for the 'peaked' and 'flat' radial impurity distributions. Figure 4.38 presents the time evolution of average density of both considered elements (C and O). The translucent grey area represents the uncertainty of calculated average density in a plasma, originating from non-perfect fitting of the simulated impurity profile (using pySTRAHL code) to the experimental data (provided by the CXRS system) as it was presented in Figure 4.37. This procedure was performed for each time frame separately. As the result, the uncertainty for the initial phase of the discharge was estimated to be ± 3%, reaching up to ± 11% at the end. At approx. 3.5 s the impurity content starts to raise due to accumulation in the central plasma.

Time evolution of average impurity density
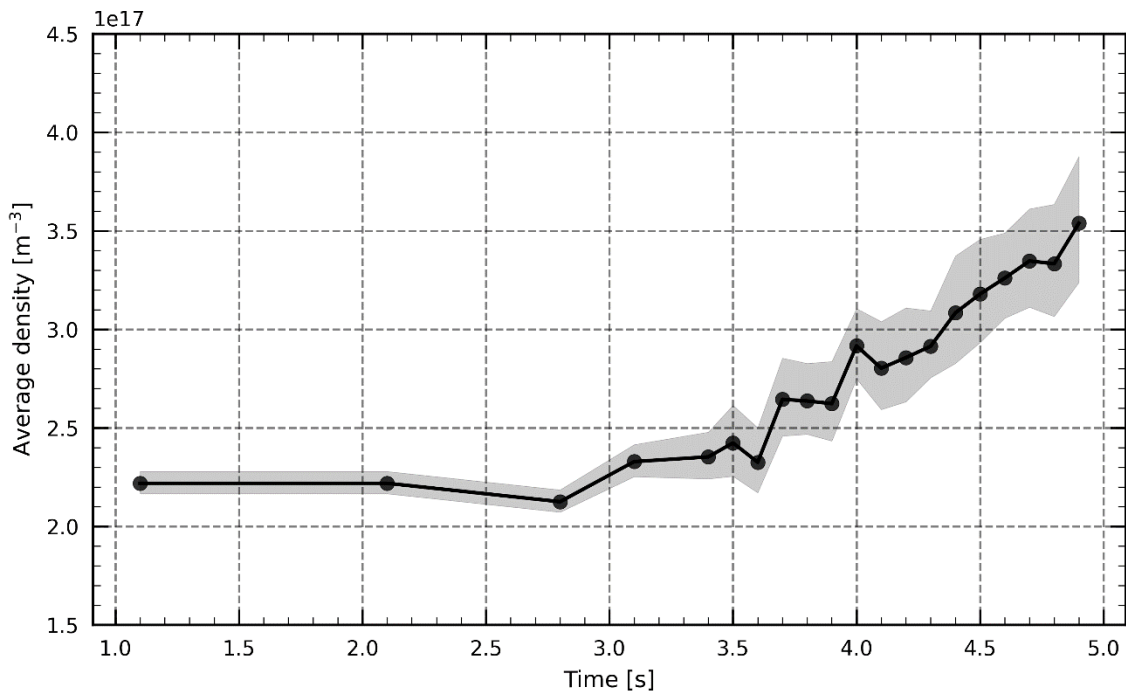
Figure 4.38. Time evolution of average impurity density in the plasma for both considered elements. The translucent grey area represents the uncertainty from fitting of the simulated impurity profile to the experimental data.

To compare 'peaked' and 'flat' impurity profiles impact on the obtained results, the calculated average densities served as a base level for 'flat' radial impurity distributions. Finally, the time evolution of C line intensity for both profile shapes were determined. Figure 4.39 presents the time evolution of C Lyman-α transition intensities measured by the C/O monitor assuming 'peaked' (blue) and 'flat' (red) radial impurity distributions. The translucent red and blue areas represent the uncertainties originating from fitting of the simulated impurity profiles corresponding to the given timeframes what was described in the previous paragraph.
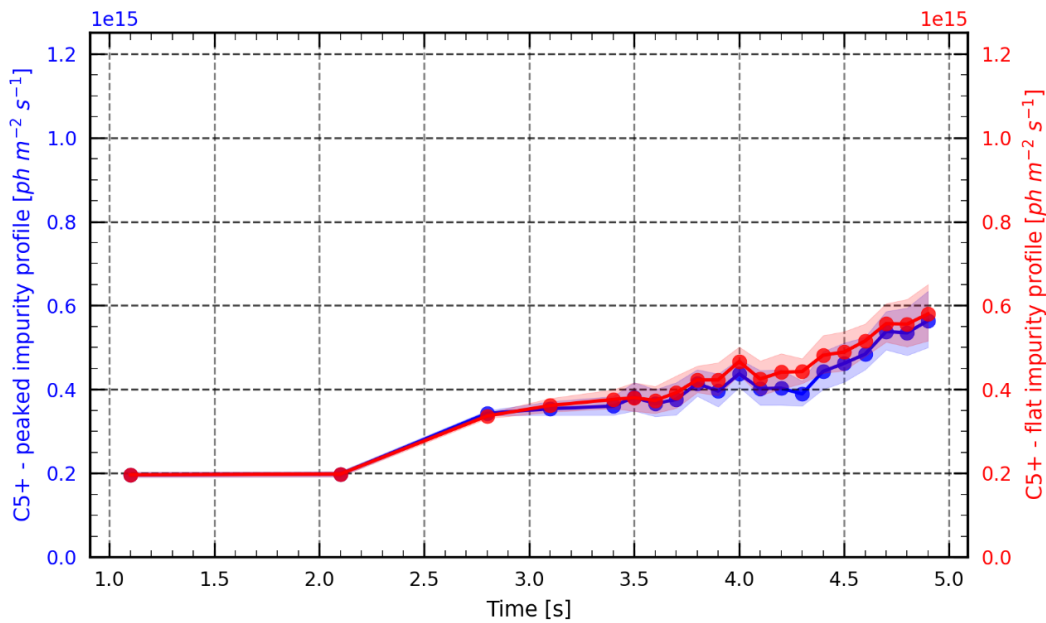
*Figure 4.39. Time evolution of calculated C^{5+} Lyman-α line intensities for **'peaked'** (blue) and **'flat'** (red) impurity profiles assuming experimental conditions from the discharge 20181009.016 .*

The total intensities for both impurity profiles are almost identical. Most of the emitted radiation for 'flat' impurity profile originates from the very edge of the plasma, whereas for the 'peaked' profile the radiation is emitted both from the edge and the plasma center – see Figure 4.40.
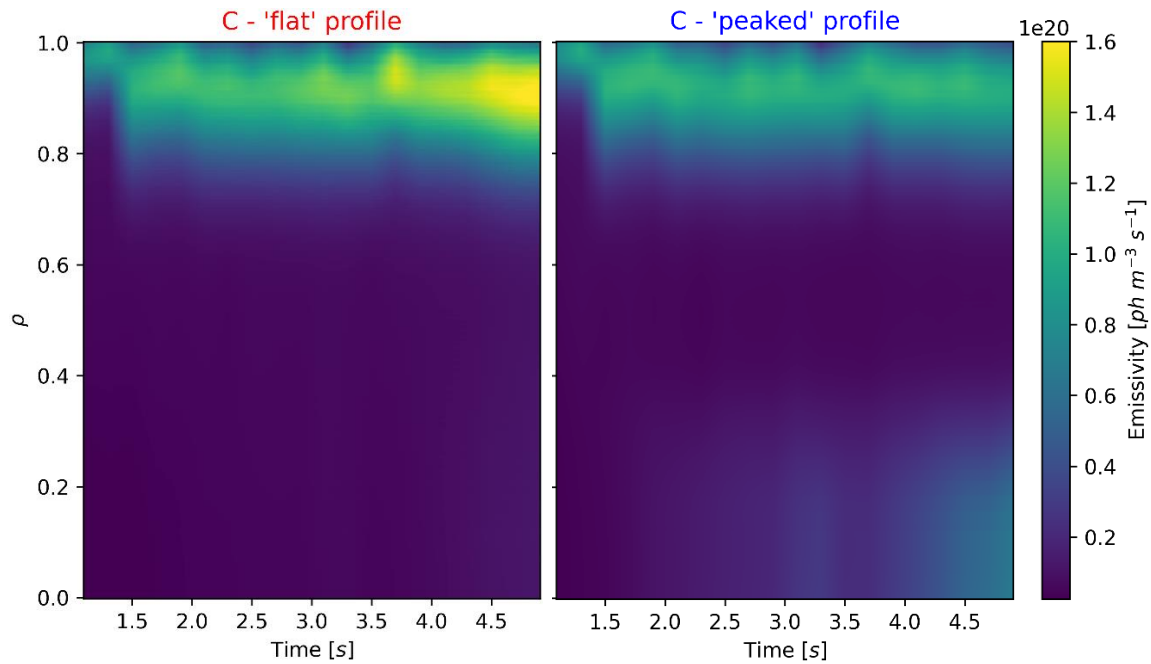
*Figure 4.40. Time evolutions of the radial emissivity distributions of the C^{5+} Lyman-α lines for a **'flat'** (left) and **'peaked'** (right – experimentally measured) impurity profiles assuming their equal average densities.*

The same procedure was applied to calculate the O Lyman-α transition. The average shapes/levels of impurities remained the same. The obtained dependencies are presented in Figure 4.41:
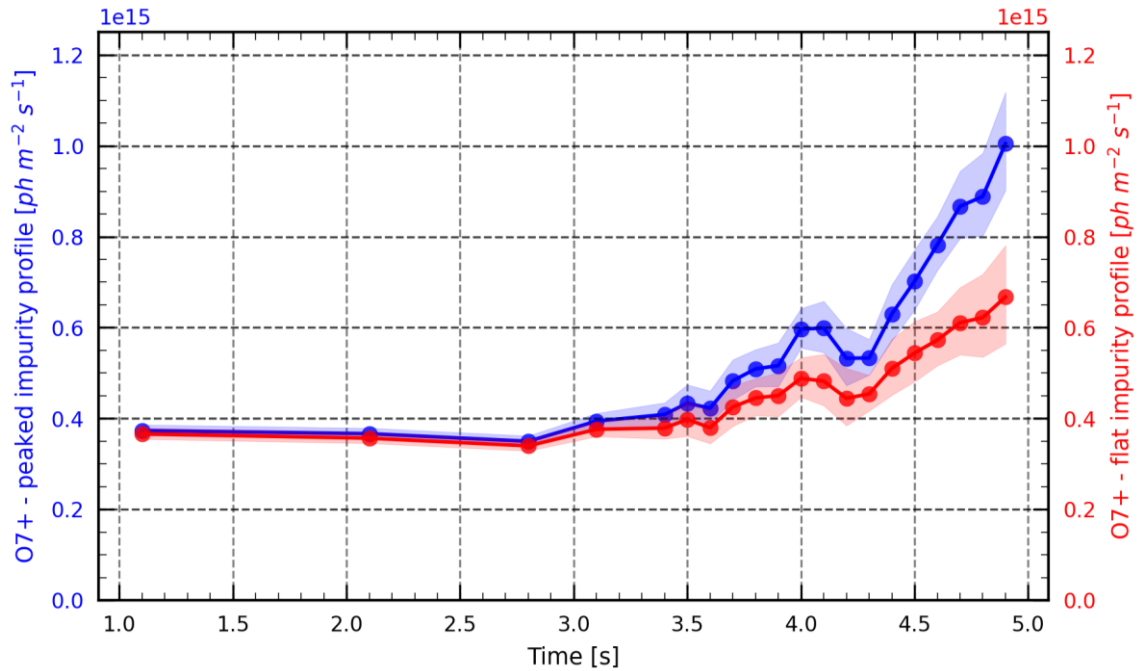
Figure 4.41. Time evolution of calculated O^{7+} Lyman-α line intensities for **'peaked'** (blue) and **'flat'** (red) impurity profiles assuming experimental conditions from the discharge 20181009.016 .

The total radiated fluxes are significantly more intense in the case of 'peaked' (blue line) compared to the 'flat' (red line) impurity profile. The radial emissivity distributions (presented in Figure 4.42) show, that for the 'flat' profile the highest emissivity is observed in the range ρ = 0.6 – 0.9. For the 'peaked' case the radiation is also emitted from the outer plasma region, however, a strong emissivity peak in the very center is observed. This central radiation becomes dominant since its intensity is almost two times higher than in the outer plasma region.
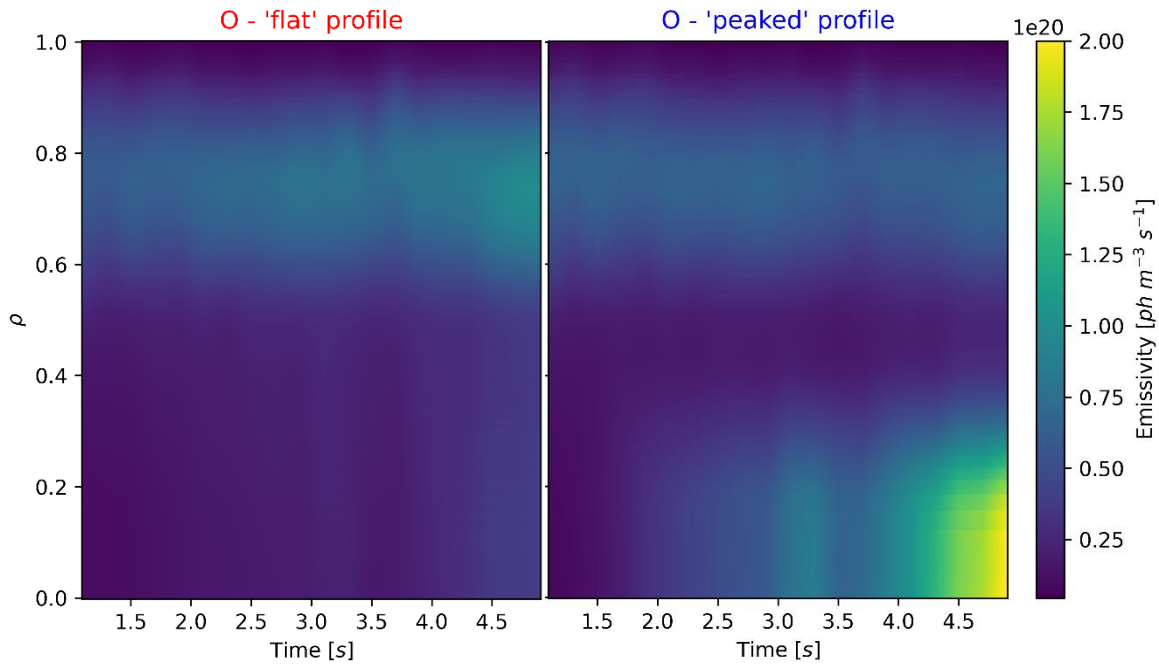
*Figure 4.42. Time evolutions of the radial emissivity distributions of the O^{7+} Lyman-α lines for a **'flat'** (left) and **'peaked'** (right) impurity profiles assuming their equal average densities.*

4.4   Simulations: conclusions

The described analyzes illustrate the C/O monitor system's efficiency in the investigation of impurities under various plasma conditions. The major factors taken under considerations were kinetic parameters (n_e and T_e) and the radial impurity profile distributions ('peaked' and 'flat'). Calculations were supported by the use of the pySTRAHL code, which was used to calculate the radial transport and the emission of impurities in the plasma bulk. It was a starting point to determine the input data (fractional abundances) used by the dedicated C/O monitor code to calculate the radial emissivity of respective transitions. Nevertheless, one needs to stress that the impurity transport itself was not investigated, but rather its impact on the radiated photon intensities in relation to the observed signals by the system.

Each of the calculated photon intensities consists of two dominant fractions: originating from excitation and recombination radiation processes. The calculations do not include charge exchange process of the considered lines. This is planned as a next step in the further code development, however, its impact is not expected to be significant [78].

From the obtained results one may notice, that the radiated photon intensities of the considered Lyman-α transitions are very sensitive to the electron temperature at its low levels (T_e < 500 eV). With the increase of atomic number, the maximum emission of elements tends to shift to plasma core, where the temperature is higher.

Since the complicated W7-X shape is normalized to a toroidal-cylindrical shape, the investigated unit plasma volume (1 cm^3), characterized by a set of characteristic parameters (e.g., n_e (R), T_e(R), n_z(R)), increases with a distance from the plasma axis. This impacts the total radiated photon intensity significantly and leads to a stronger contribution of the edge radiation fraction than the central region if 'flat' radial impurity distributions are assumed. For the higher electron temperatures, the respective radial emissivity is shifted towards the plasma boundary, to achieve the strongest emission in the plasma regions where the electron temperatures are the lowest (this is especially valid for B and C lines). For the higher-Z elements (O and N) low edge temperatures play less significant role, because their Lyman-α transitions are emitted in the vicinity of the plasma axis with a slightly higher temperature ranges (compared to B and C).

This effect can increase the emitted radiation even though the temperature increased, which is a result of the larger plasma volume from which the emission originates. For the higher electron temperatures this effect does not exceed approximately 5% of a signal strength. Similar rule is observed when considering increase of n_e, which leads to a photon intensity increase and as a consequence pushing the emissivity profile out towards the plasma edge. This, however, compared to the T_e increase is a less significant effect. Nonetheless, in some specific cases, especially in the case of B Lyman-α line, the emissivity profile is pushed outside the central plasma into the SOL region, leading to a drop of the calculated photon intensity. This is only numerical effect and has to be always taken into account when analyzing the data.

The above described effects result strictly from the change of kinetic parameters and the W7-X plasma geometry. Radial impurity distribution plays also significant role in the emissivity profile and consequently – the total photon intensity. In the context of performed analyses with the set of predefined temperature profiles, it was observed that the 'flat' radial impurity distribution implies the higher output photon intensity by

approximately 50% than in the case of 'peaked' impurity profile if the average impurity density is assumed equal. The exception was the O Lyman-α line intensities at low T_e range (below 1.5 keV), where its high central confinement implied higher photon intensities than for the 'flat' profile. This resulted from the very strong photon emission of O Lyman-α in the center of a plasma, that compared to the elements with lower atomic numbers (B, C and N) is emitted at higher T_e ranges.

Such a 'peaked' impurity profile occurs under specific plasma conditions, when the neoclassical impurity transport becomes dominant. The main factors are: high density, turbulence reduced ion-root confinement (hence negative radial electric field – E_r), strongly reduced diffusion coefficient (D) and pronounced negative convection velocity profiles (V) [74]. A strong factor associated with impurity accumulation may be also NBI heating and the use of strong pellet fueling during the experiment. While the estimation of D and V profiles are difficult to establish, information about the n_e and E_r is provided in real time. The time range in which the transition from the non-neoclassical to neoclassical regime takes place is approx. 200 ms [74]. Having information about these parameters one may notice, that if e.g., within the given time range the kinetic parameters remain constant, and the signal decrease by approx. 30% with a simultaneous negative E_r, the decrease of a signal could suggest the impurity accumulation in the core rather than the decrease of a total impurity content in the plasma. However, since at the W7-X no extensive studies were performed to clearly define, whether there is a strict rule between the abovementioned factors and occurrence of enhanced impurity confinement in the plasma, it is not sure if their presence can become a strict indicator of impurity accumulation. Therefore in order to simplify the future analysis and bring it to the level of a rather straightforward correlation, this topic needs to be thoroughly investigated.

On the other hand, the simultaneous presence of two overlapping scenarios i.e. increase of the signal being a consequence of a transition from the neoclassical to anomalous regime and decrease of impurity content in the plasma might be unnoticeable by the system because the radiated photon intensity could remain almost unchanged. This would be especially important during the steady state long pulse operation, when no significant volatility of kinetic parameters would be observed.

The increase of a signal provided by the C/O monitor system would mean, that there is an impurity influx not correlated with the plasma parameters and/or enhanced impurity confinement. In a short discharges with a dedicated heating schemes (i.e. stepped ECRH) and additional LBO/TESPEL [79], [80] injections, it will be a difficult to draw the correct conclusions without performing simulations, though. Nevertheless, when the cross calibration e.g., with the CXRS system will be performed, the system could provide precise information about impurity behavior and their concentration in the plasma based on the mapped T_e/n_e profiles (especially for the higher T_e ranges). Such analyses of experimental data, however, would require constant support of the C/O monitor code, and hence its strong optimization to perform on-the-fly calculations.

An alternative idea would be also application of the machine learning (ML) or Bayes theorem in order to predict, depending on the historical experimental dataset and the currently available information about plasma kinetic parameters, what the emissivity profile could be, and hence the output photon intensity. Thus, providing set of these information in a real time, could let the system to become an operational tool delivering reliable information about the light impurity composition in a plasma.

Although the presented procedure in most cases actualy reflects emissions of interesting Lyman-α transitions, it also have some drawbacks. These may occur when analyzing B line emission, especially in the high temperature ranges. The reason behind this are emissivity profiles being pushed out towards the plasma edge with increasing T_e (and less significantly with increasing n_e). Usually when the emissivity profile remains unchanged, this may lead to a photon intensity increase due to its emission from the larger plasma volume. However, since the highest probability of B Lyman-α line emission is most likely to occur at a very low T_e (in the order of 100 eV), this element becomes fully ionized under the central conditions while the main fraction of its emission is radiated from the very edge of a central region and even substantially from the outside of LCFS in the SOL. Thus, to perform reliable simulations, the normalized r_{eff} and the kinetic parameters outside LCFS are required.

A similar situation, but to much lesser extent is observed for the C^{5+} line emission, nevertheless, this effect is not as significant as in the B^{4+} case, since the higher electron temperatures are required to emit C Lyman-α line.

Summary and Outlook

The main goal of this work was to develop, design and construct the C/O monitor, a new XUV spectroscopic system for the Wendelstein 7-X and to prove that it will be a reliable tool for the measurement of the level of main low-Z impurities (B, C, N and O) based on line intensities of its hydrogen-like ions. The first subspectrometer section dedicated to the C and O investigations is already built and passed the laboratory tests. Its commisioning is planned before the next operational phase OP2.1 in the second half of 2022.

In order to understand the experimental output signals of the system in a very detailed manner, it was a key point to develop a dedicated numerical code to investigate impact of various plasma parameters such as T_e, n_e as well as impurity transport on the obtained signals. This was achieved by the implementation of the precise numerical representation of the system with respect to the W7-X geometry and simulation of the radiated photon fluxes. The whole work constitutes the author's approach for investigating the impact of kinetic parameters (T_e, n_e) and impurity profiles on the system's output signals.

Accordingly, as part of this dissertation I performed the following tasks:

1. I have participated in the design (using CATIA software) of the main components of the system such as vacuum chamber, table for rotational piezoelectrical drives, and support structure with the adjustment system tools to ensure the precise fine tuning of the spectrometer.

2. I have prepared the technical documentation necessary to manufacture the system.

3. I was taking part in the laboratory tests of the first sub-spectrometer section, during which I was adjusting the main optical components of the system.

4. I have developed an original code in Python which aim is to simulate the photon flux intensities reaching the detectors' surfaces. The code provides a way to simulate the system's response with respect to the e.g., change of the position of dispersive elements and apertures. It implements plasma kinetic parameters as well as radial impurity profile. To enhance its capabilities, it was

coupled with the pySTRAHL code – an external package dedicated for impurity transport calculations. Their combination ensures a way to investigate impact of radial impurity transport and to simulate the output signals (with a higher precision) with respect to the experimentally measured plasma parameters.

5. I have developed a procedure for investigation of impact of kinetic plasma parameters, impurity transport and geometry of the spectroscopic system on the photon fluxes emitted by the investigated ions.

6. I have performed a number of numerical simulations to study the impact of plasma kinetic parameters on the system's output signals. Moreover, the radial impurity distribution was investigated in order to check its impact on the total photon flux emitted towards the detectors' surfaces. The results were then compared and analysed in details. Next, I have created a colormaps illustrating the radial emissivity distributiuons of investigated lines with respect to the investigated factors, which are useful for explaining the observed phenomena.

7. I have determined the photon intensities of C and O lines that would reach the detectors (for the discharge *20181009.016*) if the system was in operation during the OP1.2. The investigations were performed assuming 'flat' and 'peaked' impurity profiles.

8. I have established the systems response with respect to the kinetic plasma parameters including also impact of impurity transport (for 'flat' and 'peaked' impurity profiles).

The aforementioned analysis showed that all energy channels of the C/O monitor system will be very sensitive to T_e (at least in some range). This is pivotal, especially at the plasma edge where T_e are the lowest, hence leading to a stronger emission of the considered spectral lines. Moreover, it was proved that the potential impurity accumulation occuring under specific plasma conditions (e.g., NBI heating and strong pellet fuelling) could lead to a decrease of a photon flux at detectors' surfaces (by approx. 50%.), even though the total amount of impurities remained constant. All of these peculiarities have been compiled into several major points that can initially indicate (with a decent precision) the impurity content in the plasma. Nevertheless,

these are the first assumptions based on simulation approach, hence they need to be experimentally tested and adjusted accordingly.

The real-time analysis could be, however, improved and extended in the future by the application of advanced numerical techniques such as e.g., machine learning (using the experimental datasets) and/or statistical Bayes theorem approach. These steps could speed up the process of providing a higher quality information about behavior of individual light impurities at an appropriate time resolution (e.g., once per 10 ms). Such results could provide a sufficient outlook on the light impurity content from the machine's operational perspective.

Finally, the results of the work presented in this dissertation proved that the C/O monitor system will be a proper tool able to provide important, real-time information about the light impurity composition in the W7-x plasma. It is also a promising device in the context of future operations of the W7-X and may become crucial from the operational point of view as well as safety.

Podziękowania

Pragnę złożyć serdeczne podziękowania mojej promotor Pani dr hab. Monice Kubkowskiej oraz mojemu promotorowi pomocniczemu Panu dr Ireneuszowi Książkowi za nieocenioną pomoc, poświęcony czas, opiekę merytoryczną oraz wiedzę, którą zawsze byli gotowi się dzielić.

Dziękuję również Dominikowi Stańczakowi, którego cenne wskazówki oraz wsparcie programistyczne pozwoliły mi sprawnie zrealizować zamierzone cele badawcze.

Ponadto dziękuję moim rodzicom, mojej narzeczonej Ani, a także siostrze z mężem oraz babci i dziadkowi, na wsparcie których zawsze mogłem liczyć.

Acknowledgements

Bibliography

[1] R. C. Wolf *et al.*, "Major results from the first plasma campaign of the Wendelstein 7-X stellarator," *Nuclear Fusion*, vol. 57, no. 10, 2017, doi: 10.1088/1741-4326/aa770d.

[2] B. Buttenschön *et al.*, "Spectroscopic impurity survey in the first operation phase ofWendelstein 7-X," 2016. Accessed: Apr. 11, 2019. [Online]. Available: http://ocs.ciemat.es/EPS2016PAP/pdf/P4.012.pdf

[3] M. Kubkowska *et al.*, "Plasma impurities observed by a pulse height analysis diagnostic during the divertor campaign of the Wendelstein 7-X stellarator," *Review of Scientific Instruments*, vol. 89, no. 10, 2018, doi: 10.1063/1.5038850.

[4] N. Krawczyk *et al.*, "Commissioning and first operation of the pulse-height analysis diagnostic on Wendelstein 7-X stellarator," *Fusion Engineering and Design*, vol. 123, no. 633053, pp. 1006–1010, 2017, doi: 10.1016/j.fusengdes.2017.02.069.

[5] A. Langenberg *et al.*, "Forward modeling of X-ray imaging crystal spectrometers within the Minerva Bayesian analysis framework," *Fusion Science and Technology*, vol. 69, no. 2, pp. 560–567, 2016, doi: 10.13182/FST15-181.

[6] A. Langenberg *et al.*, "Prospects of X-ray imaging spectrometers for impurity transport: Recent results from the stellarator Wendelstein 7-X (invited)," *Review of Scientific Instruments*, vol. 89, no. 10, p. 10G101, Oct. 2018, doi: 10.1063/1.5036536.

[7] C. Swee *et al.*, "Impurity transport studies at the HSX stellarator using active and passive CVI spectroscopy," *Plasma Physics and Controlled Fusion*, vol. 64, no. 1, 2022, doi: 10.1088/1361-6587/ac3965.

[8] IAEA, "IAEA Safety Standards: Storage of Spent Nuclear Fuel, SSG-15 (Rev. 1)," vol. 15, 2020, [Online]. Available: https://www.iaea.org/resources/safety-standards

[9]   Office of Nuclear Energy, "5 Fast Facts about Spent Nuclear Fuel | Department of Energy," 2020. https://www.energy.gov/ne/articles/5-fast-facts-about-spent-nuclear-fuel (accessed Mar. 30, 2022).

[10]   Office of Nuclear Energy, "3 Advanced Reactor Systems to Watch by 2030," *Office of Nuclear Energy*, 2021. https://www.energy.gov/ne/articles/3-advanced-reactor-systems-watch-2030 (accessed Mar. 30, 2022).

[11]   Ewa Pawelec, "Diagnostyka plazmy niskotemperaturowej metodami spektroskopii optycznej," 2014.

[12]   Griem H. R., "Principles of Plasma Spectroscopy," *Cambridge University Press*, 2005.

[13]   P. E. Boulos M. I., Fauchais P., *Thermal plasmas: Fundamentals and applications*, vol. 14, no. 2. Plenum Press, New York–London, 1994.

[14]   Hyperphysics.phy-astr.gsu.edu, "Nuclear Binding Energy," 2000. http://hyperphysics.phy-astr.gsu.edu/hbase/NucEne/nucbin.html (accessed Apr. 04, 2022).

[15]   J. P. Freidberg, *Plasma physics and fusion energy*, vol. 9780521851. 2007. doi: 10.1017/CBO9780511755705.

[16]   F. LeBlanc, *An introduction to stellar astrophysics*, vol. 48, no. 11. 2011. doi: 10.5860/choice.48-6256.

[17]   M. Kikuchi, K. Lackner, and M. Quang, "Fusion Physics," *Iaea*, pp. 24–26, 2012.

[18]   J. Wesson and D. J. Campbell, "Tokamaks - Wesson.pdf." 2011.

[19]   E. I. Moses, "The National Ignition Facility (NIF): A path to fusion energy," *Energy Conversion and Management*, vol. 49, no. 7, pp. 1795–1802, 2008, doi: 10.1016/j.enconman.2007.10.029.

[20]   J. Lindl, "Development of the indirect-drive approach to inertial confinement fusion and the target physics basis for ignition and gain," *Physics of Plasmas*, vol. 2, no. 11, pp. 3933–4024, 1995, doi: 10.1063/1.871025.

[21] R. K. Kirkwood *et al.*, "A review of laser-plasma interaction physics of indirect-drive fusion," *Plasma Physics and Controlled Fusion*, vol. 55, no. 10, 2013, doi: 10.1088/0741-3335/55/10/103001.

[22] U. of Pensylvannia, "Magnetic Bottle." https://www.sas.upenn.edu/~thomsone/html-physics/phys151/ (accessed May 10, 2022).

[23] J. Wesson, "The Science of JET," EFDA-JET, Culham Science Centre, Abingdon, 2000.

[24] "Poloidal and Toroidal Magnetic Fields." https://www.pngarea.com/pngm/180/8704367_motion-lines-png-poloidal-and-toroidal-magnetic-fields.png (accessed Jun. 01, 2022).

[25] W. Picot, "Magnetic Fusion Confinement with Tokamaks and Stellarators." https://www.iaea.org/bulletin/magnetic-fusion-confinement-with-tokamaks-and-stellarators (accessed Jun. 01, 2022).

[26] B. P. Van, A. L. Fraguas, and J. Geiger, "Suggestions for minor radius definitions in stellarators Definition of the minor radius of a (perfect) torus," no. 2, pp. 1–5, [Online]. Available: http://fusionwiki.ciemat.es/fusionwiki/images/2/21/Surf_vol.pdf

[27] U. Stroth, "A comparative study of transport in stellarators and tokamaks," *Plasma Physics and Controlled Fusion*, vol. 40, no. 1, pp. 9–74, 1998, doi: 10.1088/0741-3335/40/1/002.

[28] J. C. Schmitt, J. N. Talmadge, P. H. Probert, and D. T. Anderson, "Measurement of the Pfirsch-Schlüter and Bootstrap Currents in HSX," pp. 1–4.

[29] M. Endler *et al.*, "Wendelstein 7-X on the path to long-pulse high-performance operation," *Fusion Engineering and Design*, vol. 167, no. February, 2021, doi: 10.1016/j.fusengdes.2021.112381.

[30] Max Planck Institute for Plasma Physics, "Limiter." https://www.ipp.mpg.de/1766018/limiter (accessed Jun. 17, 2022).

[31] Max Planck Institute for Plasma Physics, "Divertor." https://www.ipp.mpg.de/1766198/divertor (accessed Jun. 17, 2022).

[32] T. Klinger *et al.*, "Overview of first Wendelstein 7-X high-performance operation," *Nuclear Fusion*, vol. 59, no. 11, 2019, doi: 10.1088/1741-4326/ab03a7.

[33] R. C. Wolf *et al.*, "Electron-cyclotron-resonance heating in Wendelstein 7-X: A versatile heating and current-drive method and a tool for in-depth physics studies," *Plasma Physics and Controlled Fusion*, vol. 61, no. 1, 2019, doi: 10.1088/1361-6587/aaeab2.

[34] P. Mc Neely et al., "Commissioning and initial operation of the W7-X neutral beam injection heating system," *14th International Symposium on Fusion Nuclear Technology [Fusion Eng. Des. (unpublished) (2019)]*.

[35] J. Ongena, Y. O. Kazakov, and B. Schweer, "The ICRH system for the stellarator Wendelstein 7-X," *47th EPS Conference on Plasma Physics, EPS 2021*, vol. 2021-June, no. September 2020, pp. 465–468, 2021.

[36] K. Miyamoto, *Plasma Physics for Controlled Fusion Second Edition*. 2015.

[37] D. Naujoks, *Plasma-Material Interaction in Controlled Fusion*. 2006. doi: 10.1007/3-540-32149-7.

[38] I. Raidpath, "A Dictionary of Astronomy," *A Dictionary of Astronomy*, 2012, doi: 10.1093/acref/9780199609055.001.0001.

[39] D. A. Frank-Kamieniecki, "Wykład z fizyki plazmy," *PWN*, 1968.

[40] H.-J. Kunze, *Introduction to Plasma Spectroscopy*, vol. 19. 1991.

[41] T. Putterich, "Investigations on Spectroscopic Diagnostic of High-Z Elements in Fusion Plasmas," Universitat Augsburg, 2005.

[42] Atomic Data and Analysis Structure, "OPEN-ADAS." https://open.adas.ac.uk/adf15 (accessed May 08, 2010).

[43] F. F. Chen, *Introduction to Plasma Physics and Controlled Fusion. Volume 1: Plasma Physics*. 1984.

[44] L. Vano, "Carbon content and transport investigations on Wendelstein 7-X with Charge Exchange Recombination Spectroscopy," [Unpublished doctoral dissertation], Technischen Universität Berlin, 2022.

[45] P. Helander *et al.*, "Stellarator and tokamak plasmas: A comparison," *Plasma Physics and Controlled Fusion*, vol. 54, no. 12, 2012, doi: 10.1088/0741-3335/54/12/124009.

[46] P. Helander, "Theory of plasma confinement in non-axisymmetric magnetic fields," *Reports on Progress in Physics*, vol. 77, no. 8, 2014, doi: 10.1088/0034-4885/77/8/087001.

[47] M. N. A. Beurskens *et al.*, "Ion temperature clamping in Wendelstein 7-X electron cyclotron heated plasmas," *Nuclear Fusion*, vol. 61, no. 11, 2021, doi: 10.1088/1741-4326/ac1653.

[48] R. Dux, "STRAHL User Manual," 2006.

[49] A. Greiche, W. Biel, O. Marchuk, and R. Burhenn, "Absolute intensity calibration of the Wendelstein 7-X high efficiency extreme ultraviolet overview spectrometer system," *Review of Scientific Instruments*, vol. 79, no. 9, 2008, doi: 10.1063/1.2977541.

[50] A. Czarnecka *et al.*, "Study of impurity behaviour for first magnetic configuration changes in W7-X plasmas by means of PHA spectra," *Fusion Engineering and Design*, vol. 136, 2018, doi: 10.1016/j.fusengdes.2018.04.119.

[51] C. Brandt *et al.*, "Installation of the soft X-ray multi-camera tomography system (XMCTS) in the Wendelstein 7-X stellarator," *Fusion Engineering and Design*, vol. 123, pp. 887–891, 2017, doi: 10.1016/j.fusengdes.2017.02.111.

[52] D. Zhang *et al.*, "Bolometer tomography on Wendelstein 7-X for study of radiation asymmetry," *Nuclear Fusion*, vol. 61, no. 11, 2021, doi: 10.1088/1741-4326/ac2778.

[53] M. Kubkowska, B. Buttenschön, and A. Langenberg, "W7-X plasma diagnostics for impurity transport studies," *Problems of Atomic Science and Technology*, vol. 118, no. 6, pp. 312–316, 2018.

[54] R. Neu *et al.*, "Monitor for the carbon and oxygen impurities in the ASDEX Upgrade tokamak," *Review of Scientific Instruments*, vol. 67, no. 5, pp. 1829–1833, May 1996, doi: 10.1063/1.1147522.

[55] D. D. le Pevelen, "Bragg ' s Law Small Molecule X-Ray Crystallography , Theory and Workflow X-Ray Fluorescence Spectrometers *," no. Warren 1990, 2010.

[56] T. Fornal *et al.*, "XUV diagnostic to monitor H-like emission from B, C, N, and O for the W7-X stellarator," *Review of Scientific Instruments*, vol. 90, no. 9, 2019, doi: 10.1063/1.5099448.

[57] I. Książek, "Private Communication," 2018.

[58] J. L. Schwob, A. W. Wouters, S. Suckewer, and M. Finkenthal, "High-resolution duo-multichannel soft x-ray spectrometer for tokamak plasma diagnostics," *Review of Scientific Instruments*, vol. 58, no. 9, pp. 1601–1615, 1987, doi: 10.1063/1.1139408.

[59] I. Książek, "JET Experimental Campaigns 2008 - Analysis comparisons between KS6 and KT4 line intensities," 2008.

[60] J. Miles, "Detection of Chiral Organic Compounds with Femtosecond Lasers," no. November, pp. 3–12, 2016.

[61] R. Burhenn, "Private Communication," 2021.

[62] D. Bolshukhin, R. Neu, D. Schlögl, and R. Dux, "Measurement of spurious impurity concentrations in ASDEX Upgrade by x-ray spectroscopy," *Review of Scientific Instruments*, vol. 72, no. 11, p. 4115, 2001, doi: 10.1063/1.1405792.

[63] R. Neu *et al.*, "Monitor for the carbon and oxygen impurities in the ASDEX Upgrade tokamak," *Review of Scientific Instruments*, vol. 67, no. 5, pp. 1829–1833, 1996, doi: 10.1063/1.1147522.

[64] M. Chernyshova *et al.*, "Gaseous electron multiplier-based soft x-ray plasma diagnostics development: Preliminary tests at ASDEX Upgrade," *Review of Scientific Instruments*, vol. 87, no. 11, pp. 1–5, 2016, doi: 10.1063/1.4960305.

[65] M. Chernyshova *et al.*, "Conceptual design and development of GEM based detecting system for tomographic tungsten focused transport monitoring,"

Journal of Instrumentation, vol. 10, no. 10, 2015, doi: 10.1088/1748-0221/10/10/P10022.

[66] S. Morita and M. Goto, "Space-resolved VUV spectroscopy using the 3 m normal incidence spectrometer with back-illuminated CCD detector in the LHD," *Review of Scientific Instruments*, vol. 74, no. 3 II, pp. 2036–2039, 2003, doi: 10.1063/1.1535252.

[67] Greateyes, "Greateyes CCD Camera Alex-s." https://www.greateyes.de/projects/greateyes/static/custom/file/Datasheets/greateyes_ALEX_s_Rev3.pdf (accessed May 07, 2022).

[68] Dask Development Team, "Dask: Library for dynamic task scheduling," *Https://Dask.Org*. 2016. [Online]. Available: http://dask.pydata.org

[69] "VMEC code." [Online]. Available: https://princetonuniversity.github.io/STELLOPT/

[70] C. Swee, "Private Communication," 2022.

[71] O. P. Ford *et al.*, "Charge exchange recombination spectroscopy at Wendelstein 7-X," *Review of Scientific Instruments*, vol. 91, no. 2, 2020, doi: 10.1063/1.5132936.

[72] T. Andreeva *et al.*, "Magnetic configuration scans during divertor operation of Wendelstein 7-X," 2022.

[73] J. Baldzuhn *et al.*, "Pellet fueling experiments in Wendelstein 7-X," 2019.

[74] A. Langenberg *et al.*, "Impurity transport in ion- A nd electron-root confinement scenarios at Wendelstein 7-X," *Nuclear Fusion*, vol. 61, no. 11, 2021, doi: 10.1088/1741-4326/ac24d4.

[75] T. Romba, "Private Communication," 2022.

[76] T. Fornal et. al, "Spectrocopic system 'C/O monitor for Wendelstein 7-X' as indicator of plasma wall interaction," *Nuclear Materials and Energy*, 2022, doi: Paper submitted.

[77] M. Hirsch *et al.*, "ECE Diagnostic for the initial Operation of Wendelstein 7-X," *EPJ Web of Conferences*, vol. 203, p. 03007, 2019, doi: 10.1051/epjconf/201920303007.

[78] O. Ford, "Private Communication," 2021.

[79] T. Wegner *et al.*, "Design, capabilities, and first results of the new laser blow-off system on Wendelstein 7-X," *Review of Scientific Instruments*, vol. 89, no. 7, 2018, doi: 10.1063/1.5037543.

[80] R. Bussiahn *et al.*, "Tracer-Encapsulated Solid Pellet (TESPEL) injection system for Wendelstein 7-X," *Review of Scientific Instruments*, vol. 89, no. 10, 2018, doi: 10.1063/1.5038844.